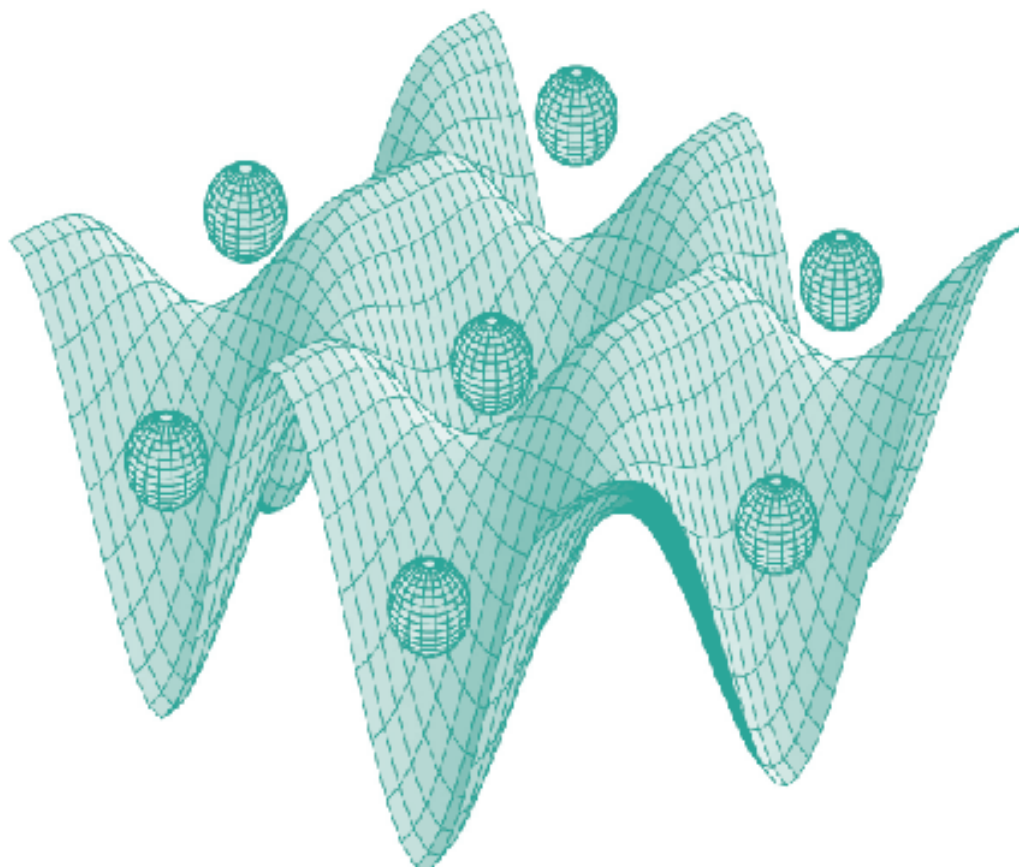




STUDIA UNIVERSITATIS  
BABEȘ-BOLYAI



# PHYSICA

---

1-2/2017

**STUDIA  
UNIVERSITATIS BABEŞ-BOLYAI  
PHYSICA**

**1-2/2017  
January-December**

---

**EDITORIAL OFFICE OF STUDIA UBB PHYSICA:**

1, M. Kogălniceanu St., Cluj-Napoca, ROMANIA, Phone: +40 264 405300

[http://www.studia.ubbcluj.ro/serii/physica/index\\_en.html](http://www.studia.ubbcluj.ro/serii/physica/index_en.html)

---

**EDITOR-IN-CHIEF:**

Professor Aurel POP, Ph.D., Babeş-Bolyai University, Cluj-Napoca, Romania

**EDITORIAL BOARD:**

Professor Simion AŞTILEAN, Ph.D., Babeş-Bolyai University, Cluj-Napoca, Romania

Professor Istvan BALLAI, Ph.D., The University of Sheffield, United Kingdom

Zoltan BALINT, Ph.D., Ludwig Boltzmann Institute Graz, Austria

Professor Titus BEU, Ph.D., Babeş-Bolyai University, Cluj-Napoca, Romania

Prof. Boldizsár JANKÓ, Ph.D., University of Notre Dame, USA

Professor Emil BURZO, Ph.D., Babeş-Bolyai University, Cluj-Napoca, Romania,  
member of Romanian Academy

Professor Vasile CHIŞ, Ph.D., Babeş-Bolyai University, Cluj-Napoca, Romania

Professor Olivier ISNARD, Ph.D., University J. Fourier & Institut Neel, Grenoble,  
France

Professor Ladislau NAGY, Ph.D., Babeş-Bolyai University, Cluj-Napoca, Romania

Professor Zoltan NEDA, Ph.D., Babeş-Bolyai University, Cluj-Napoca, Romania

Professor Jurgen POPP, Ph.D., Dr.h.c., Institute of Physical Chemistry, Friedrich-  
Schiller-University Jena, Germany

Professor György SZABÓ, Ph.D., Research Institute for Technical Physics and  
Materials Science, Hungarian Academy of Sciences, Budapest, Hungary

Professor Simion SIMON, Ph.D., Babeş-Bolyai University, Cluj-Napoca, Romania

Professor Romulus TETEAN, Ph.D., Babeş-Bolyai University, Cluj-Napoca, Romania

Professor Dietrich ZAHN, Ph.D., Dr.h.c., Technical University, Chemnitz, Germany

**EXECUTIVE EDITOR:**

Lecturer Claudiu LUNG, Ph.D., Babeş-Bolyai University, Cluj-Napoca, Romania

YEAR  
MONTH  
ISSUE

Volume 62 (LXII) 2017  
DECEMBER  
1-2

---

PUBLISHED ONLINE: 2017-12-30  
PUBLISHED PRINT: 2017-12-30  
ISSUE DOI:10.24193/subbphys.2017

---

**S T U D I A**  
**UNIVERSITATIS BABEȘ–BOLYAI**  
**PHYSICA**

1-2

---

**STUDIA UBB EDITORIAL OFFICE:** B.P. Hasdeu no. 51, 400371 Cluj-Napoca, Romania,  
Phone + 40 264 405352

---

**CUPRINS – CONTENT – SOMMAIRE – INHALT**

A.-M. HADA, M. POTARA, S. SUĂRĂȘAN, A. VULPOI, S. AȘTILEAN, *Chitosan-Coated Bimetallic Gold-Silver Nanoparticles: Synthesis, Characterization and Sers Activity* ..... 5

C. MOISESCU-GOIA, M. MUREȘAN-POP, V. SIMON, *XRD Checking of Crystalline Forms Resulted by Slow Evaporation of 5-Fluorouracil Solutions Obtained with Different Solvents* ..... 15

L.C. ȘUȘU, A.M. CRĂCIUN, S. AȘTILEAN, *Synthesis and Characterization of Polydopamine-Coated Gold Nanorods* ..... 23

M. TODICA, C. V. POP, <i>Simple Method for Digital Data Recording of Damped Oscillations of Mechanical Pendulum</i> .....	33
RÉKA-ANITA DOMOKOS, V. CHIŞ, <i>Conformational Space and Electronic Absorption Properties of the Two Isomers of Resveratrol</i> .....	43
M. TODICA, Z. KOVACS-KRAUSS, CARMEN NICULAESCU, <i>XRD Investigation of Thermal Degradation Effect on some Commercial Pet Samples</i> .....	63
LARISA MILENA ŢIMBOLMAŞ, V. CHIŞ, <i>Photophysical Properties of Perylene Molecule</i> .....	73
A. OKOS, OANA RAITA, A. POP, <i>Magnetic Properties of the Perovskite Oxide <math>PbV_{1-x}Fe_xO_3</math> Investigated by Electron Paramagnetic Resonance Spectroscopy</i> .....	87
I. COSMA, <i>Versatile Measuring Device for the Study of Magnetic Properties of Solids</i> .....	101

## CHITOSAN-COATED BIMETALLIC GOLD-SILVER NANOPARTICLES: SYNTHESIS, CHARACTERIZATION AND SERS ACTIVITY

A.-M. HADA<sup>1,2</sup>, M. POTARA<sup>2\*</sup>, S. SUARASAN<sup>2</sup>,  
A. VULPOI<sup>3</sup> and S. ASTILEAN<sup>1,2</sup>

**ABSTRACT.** In this study we report a fast and non-toxic approach for the synthesis of bimetallic gold-silver spherical nanoparticles coated with chitosan biopolymer. The obtained hybrid nanoparticles were characterized by UV-vis-NIR extinction spectroscopy, transmission electron microscopy (TEM) and zeta potential measurements. In view of future applicability in molecular sensing, we tested the feasibility of chitosan protected bimetallic nanoparticles to operate as surface-enhanced Raman scattering substrates.

**Keywords:** *chitosan; plasmonic nanoparticles; localized surface plasmon resonance; surface-enhanced Raman spectroscopy; transmission electronic microscopy; zeta potential*

---

<sup>1</sup> Department of Biomolecular Physics, Faculty of Physics, Babes-Bolyai University, M. Kogalniceanu Str. 1, 400084 Cluj-Napoca, Romania

<sup>2</sup> Nanobiophotonics and Laser Microspectroscopy Center, Interdisciplinary Research Institute in Bio-Nano-Sciences, Babes-Bolyai University, T. Laurian Str. 42, 400271 Cluj-Napoca, Romania

<sup>3</sup> Nanostructured Materials and Bio-Nano-Interfaces Center, Interdisciplinary Research Institute in Bio-Nano-Sciences, Babes-Bolyai University, T. Laurian 42, 400271, Cluj-Napoca, Romania

\* Corresponding author: monica.potara@phys.ubbcluj.ro

## INTRODUCTION

An important challenge of nanotechnology is the preparation of nanoparticles with desired properties and functions. In many cases the physical and chemical properties as well as the applications of nanoparticles are critically controlled by their dimension and shape [1]. This is also the case of noble-metal nanoparticles which exhibit extremely interesting optical response in interaction with light. When the incoming light couples with the oscillation frequency of the conduction electrons, a so-called localized surface plasmon resonance (LSPR) arises, which is manifested as an intense absorption band [2]. However, the precise spectral position of the plasmon resonance depends on several parameters, among which particle size and shape and their degree of assembling are the most important [3].

Due to their unique physical and chemical properties, noble-metal nanoparticles also called plasmonic nanoparticles are very attractive in a variety of biomedical applications such as: molecular sensing [4], molecular diagnosis [5], antibacterial action [6], drug delivery [7], bio-labeling [8], cancer therapy [9], etc. Besides the size and shape control, the usefulness of plasmonic nanoparticles in different applications strongly depends also on their structural and optical stability in the growth medium. For example, the plasmon-enhanced spectroscopies require stable and well-defined resonances and a shift of plasmon resonance can reduce the signal intensity by orders of magnitude.

The use of natural polymers to stabilize the plasmonic nanoparticles has received considerable attention recently [10], [11], especially for the safety point of view. Among them, chitosan shows very interesting biological, physical and chemical properties which make it possible to use chitosan-protected nanoparticles in biological applications [12]. Chitosan is a cationic polysaccharide obtained by partial deacetylation of chitin. It is an inexpensive polymer which possesses several favorable biological properties such as an excellent biocompatibility, low toxicity, biodegradability and adsorption ability [13].

The metal type is another parameter that influences the applicability of plasmonic nanoparticles. For example, gold nanoparticles exhibit higher chemical stability in comparison with the silver ones. However, silver is a more efficient plasmonic material than gold and can be excited with more energetic light due to a significantly reduced damping for interband transitions which make it an ideal candidate for sensing applications based on plasmon-enhanced spectroscopies [14]. In this context, bimetallic gold-silver nanoparticles could be a good option for sensing application.

In this work we report a facile, rapid, and inexpensive route to synthesize bimetallic gold-silver spherical nanoparticles. Due to its interesting biological, chemical and physical properties we selected chitosan biopolymer for the stabilization of the particles. The produced chitosan-coated bimetallic gold-silver nanoparticles were characterized by UV-vis-NIR extinction spectroscopy, transmission electron microscopy (TEM) and zeta potential measurements. The surface-enhanced Raman scattering efficiency of the fabricated nanoparticles was assessed with para-aminothiophenol (pATP) as a probe molecule.

## EXPERIMENTAL DETAILS

### Chemicals

Chitosan flakes (medium molecular weight),  $\text{HAuCl}_4$ , and paraaminothiophenol (pATP) were purchased from Aldrich and used without further purification. Glacial acetic acid (99.8%), silver nitrate ( $\text{AgNO}_3$ ) and ascorbic acid were obtained from Merck. Glacial acetic acid was diluted to a 1% aqueous solution before use. All reagents employed were of analytical grade and the solutions were prepared using ultrapure water with a resistivity of at least 18 M $\Omega$  cm. The glassware used was cleaned with aqua regia solution ( $\text{HCl}:\text{NO}_3$  3:1) and then rinsed carefully with ultrapure water. A solution of 2 mg/mL chitosan was prepared by dissolving the polymer in 1% acetic acid solution. The mixture was kept for a day until the solution became clear.



### **Preparation of chitosan-coated bimetallic gold-silver nanoparticles**

Chitosan-coated bimetallic gold-silver nanoparticles (Au-AgNPs) were synthesized using a two-step approach. In the first step, spherical gold nanoparticles (AuNPs) were prepared by mixing a volume of  $10^{-3}$  M HAuCl<sub>4</sub> with 18 ml chitosan solution and keeping this mixture at 50 °C under magnetic stirring until the solution turns red. In the second step, ascorbic acid, AgNO<sub>3</sub> and 5 ml of as-prepared spherical gold nanoparticles were combined and kept at room temperature for 30 minutes under continuous magnetic stirring. For SERS measurements, 990  $\mu$ L of Au-AgNPs were incubated at room temperature for several hours with 10  $\mu$ L solution of pATP, followed by centrifugation and re-suspension in ultrapure water.

### **Equipment and characterization methods**

A 2 mm quartz cuvette was used to collect the LSPR spectra, using a Jasco V-670 UV-VIS-NIR spectrometer with 1 nm spectral resolution.

The transmission electron microscopy (TEM) images were collected using a high resolution electronic microscope FEI Tecnai F20.

The Raman spectra were recorded on a confocal Raman microscope (CRM alpha 300R from WITec GmbH, Germany) in backscattering geometry, employing 532 nm laser line as the excitation source directed through a 20x objective lens with a numerical aperture (NA) of 0.4.

The zeta potential of the AuNPs and Au-AgNPs was determined using a Malvern Zetasizer Nano ZS-900. The analysis was performed at a temperature of 25°C, with a He-Ne laser (5mW).

The theoretical extinction spectra were calculated using the method Finite Difference Time Domain (FDTD) provided by the software FDTD Lumerical Solutions [15]. The FDTD method solves electromagnetics problems, Maxwell's differential equations to be more specific. We calculated the extinction spectrum for a 16 nm gold sphere enveloped in a silver layer of

2.2 nm and surrounded by water ( $n=1.33$ ). In order to perform the simulation, we used a 0.2 nm mesh and an electromagnetic source with a domain between 300 nm and 700 nm.

## RESULTS AND DISCUSSION

AuNPs are obtained using the reducing agent chitosan, which is also a stabilizer agent, to reduce the Au ions and form the nanoparticles as crystalline networks of Au atoms. The UV-Vis spectrum of the AuNPs (Fig. 1) shows a narrow band with a single peak at 524 nm which is typical for monodispersed spherical AuNPs. The lack of band in the near-infrared (NIR) region indicates that the AuNPs do not aggregate.

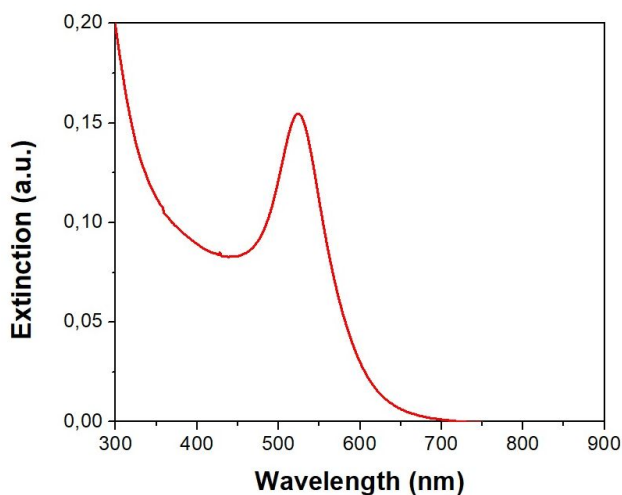


**Fig. 1.** The extinction spectrum of chitosan-coated AuNPs

In the interest of obtaining more information about the size and the shape of the AuNPs some TEM images were taken, a representative TEM image of the synthesized AuNPs being presented in Fig. 2. As can be seen

from the TEM analysis, the NPs are spherical with the mean particle diameter of 16 nm (see histogram in Fig. 2(a) inset). The results were obtained by analyzing several TEM images.

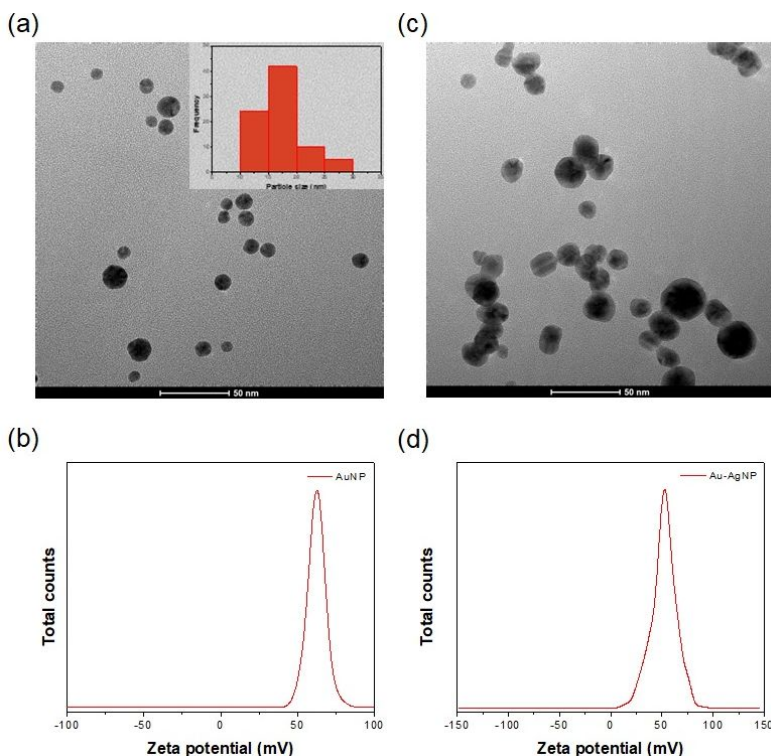
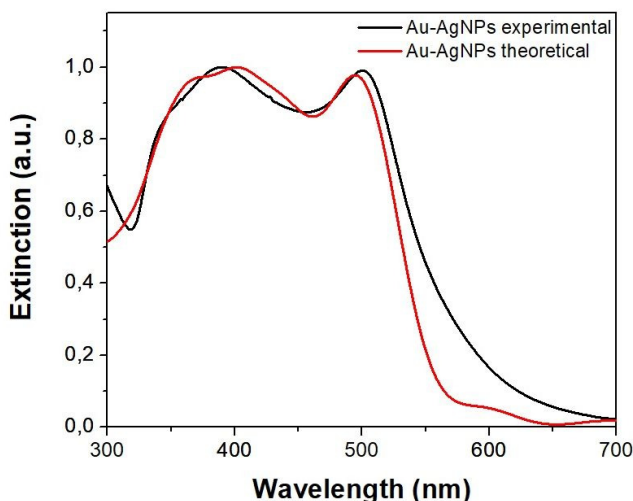


**Fig. 2.** (a) A representative TEM image of the chitosan-coated AuNPs, (b) the zeta potential of chitosan-coated AuNPs (c) A representative TEM image of chitosan-coated Au-AgNPs, (d) the zeta potential of chitosan-coated Au-AgNPs

Zeta potential measurements were further performed to evaluate the electrostatic repulsion between polymer-coated AuNPs. The value of the zeta potential gives us information about the stability of the colloidal solutions. Nanoparticles with a value of the zeta potential higher than  $\pm 30$  mV are considered stable. The zeta-potential analysis from Fig. 2(b) reveals that the particles are positively charged (+62.4 mV) due to the polymeric coating.

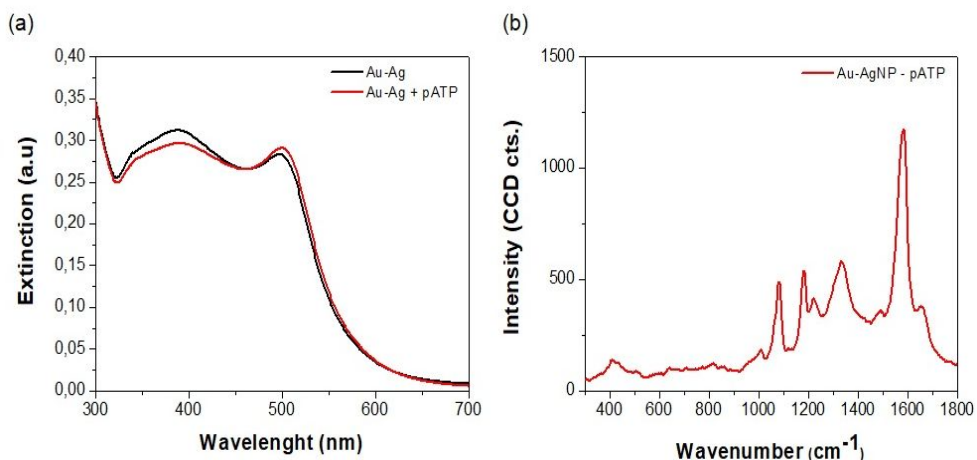
Au-AgNPs were obtained by gradual reducing silver ions with ascorbic acid into a solution of chitosan-coated AuNPs. Reduction of silver ions leads to the formation of bimetallic gold-silver nanoparticles. Fig. 2(c) illustrates a representative TEM picture of obtained Au-AgNPs which clearly reveals the formation of individual particles mainly of spherical shape. The strong positive surface charge of Au-AgNPs in Fig. 2(d) (+ 42.6 mV) indicates the presence of polymeric coating around Au-AgNPs and the good stability of colloidal suspension.

Fig. 3 (black line) shows the extinction spectrum of Au-AgNPs which features two LSPR bands resulting from the hybridization of individual surface plasmon resonance localized on gold nanosphere coated by silver layer and surface plasmon resonance localized on silver nanolayer. To understand the plasmonic response of Au-AgNPs a numerical simulation of hybridization was carried out using FDTD software (Lumerical). For simulation we considered a gold sphere of 16 nm diameter covered by a silver layer of 2.2 thickness surrounded by water ( $n = 1.333$ ). The simulated spectrum in Fig. 3 (red line) clearly exhibits two distinct bands indicating once more the bimetallic structure of the fabricated nanoparticles.



**Fig. 3.** The experimental and theoretical extinction spectra of chitosan-coated Au-AgNPs

Next, we investigate the SERS activity of Au-AgNPs using pATP as a probe molecule. Fig. 4(a) illustrates the extinction spectra of Au-AgNPs before (black spectrum) and after incubation with pATP (red spectrum). We noticed that the shape of extinction spectrum was preserved and no sign of aggregation is observed. This suggests that chitosan provide good stability to Au-AgNPs keeping nanoparticles far from approaching and preventing their aggregation. However, a 3 nm red shift of the plasmonic band at 500 nm was observed in the presence of pATP molecules. This result indicates that chitosan preserves the stability of nanoparticles, while allows the exchange with surrounding medium, keeping the ability of Au-AgNPs to sense the modifications of refractive index values. This is why we assume that pATP molecules can diffuse through the internal nanoporosities of chitosan and immobilize on the particles surface, leading to an increase of the refractive index of the medium surrounding the particles.



**Fig. 4.** (a) The extinction spectra of Au-AgNPs before (black spectrum) and after (red spectrum) the addition of pATP (b) SERS spectrum of pATP on colloidal suspension by laser excitation wavelength 532 nm

In Fig. 4(b) we recorded the SERS spectrum of pATP molecules in solution at a final concentration of  $10 \times 10^{-6}$  M. The illustrated spectrum clearly identifies the characteristic bands of pATP when is adsorbed onto the surface of Au-AgNPs. In particular, the most intense bands at  $1080 \text{ cm}^{-1}$ ,  $1582 \text{ cm}^{-1}$ , and  $1184 \text{ cm}^{-1}$  are assigned to  $a_1$  vibrational modes of p-ATP, namely, C-S stretching vibration, C-C stretching mode, and C-H bending mode [16]. Considering the final concentration of pATP in colloidal solution relatively low and no sign of aggregation observed after the addition of pATP, the signal detected from adsorbed molecules clearly demonstrates a good SERS activity of as prepared Au-AgNPs.

## CONCLUSIONS

In conclusion, stable chitosan-coated bimetallic Au-AgNPs dispersed in aqueous solution were prepared through a rapid, environmentally friendly procedure. The presence of chitosan onto the surface of Au-AgNPs was evidenced by zeta potential measurements. The bimetallic structure of the fabricated nanoparticles was confirmed by comparing the experimental and theoretical extinction spectrum of Au-AgNPs. The morphology of Au-AgNPs was investigated by TEM analysis, which revealed the formation of individual nanoparticles, mainly of spherical shape. The obtained Au-AgNPs were found to be excellent SERS substrates.

## ACKNOWLEDGEMENTS

This work was supported by CNCS-UEFISCDI, project number PN-II-RU-TE-2014-4-1988.

## REFERENCES

1. E. Boisselier, D. Astruc, *Chem. Soc. Rev.*, 38, 6 (2009).
2. M.A. Garcia, *J. Phys. Appl. Phys.*, 44, 28 (2011).
3. M. Tréguer-Delapierre, J. Majimel, S. Mornet, E. Duguet, S. Ravaine, *Gold Bull.*, 41, 2 (2008).
4. J. Du, B. Zhu, X. Chen, *Small*, 9, 24 (2013).
5. Y.-C. Yeh, B. Creran, V.M. Rotello, *Nanoscale*, 4, 6 (2012).
6. B. Le Ouay, F. Stellacci, *NanoToday*, 10, 3 (2015).
7. B. Kang, M.M. Afifi, L.A. Austin, M.A. El-Sayed, *ACS Nano*, 7, 8 (2013).
8. T.L. Paxon, R.S. Duthie, C. Renko, A.A. Burns, M.L. Lesaichere, F.J. Mondello, *Proc. SPIE 8034* (2011).
9. S. Jain, D.G. Hirst, J.M. O'Sullivan, *Br. J. Radiol.*, 85, 1010 (2012).
10. M.P. Neupane S.J. Leel. S. Park M.H. Lee, T.S. Bae, Y. Kuboki, M. Uo, F. Watari, *J. Nanoparticle Res.*, 13, 2 (2010).
11. E.-K. Lim W. Sajomsang, Y. Choi, E. Jang, H. Lee, B. Kang, E. Kim, S. Haam, J.S. Suh, S.J. Chung, Y.M. Huh, *Nanoscale Res. Lett.*, 8, 1 (2013)
12. M.S. P. Boyles, T. Kristl, A. Andosch, M. Zimmermann, N. Tran, E. Casals, M. Himly, V. Puntès, C.G. Huber, U. Lütz-Meindl, A. Duschl, *J. Nanobiotechnology*, 13, 84 (2015).
13. R.C.F. Cheung, T.B. Ng, J.H. Wong, and W.Y. Chan, *Mar. Drugs*, 13, 8 (2015).
14. Y.H. Lee, H. Chen, Q.-H. Xu, J. Wang, *J. Phys. Chem. C*, 115, 16 (2011).
15. [http://docs.lumerical.com/en/fdtd/knowledge\\_base.html](http://docs.lumerical.com/en/fdtd/knowledge_base.html). [Online] Lumerical Solutions, Inc.
16. X. Zou, S. Dong, *J. Phys. Chem. B*, 110, 43 (2006).

## XRD CHECKING OF CRYSTALLINE FORMS RESULTED BY SLOW EVAPORATION OF 5-FLUOROURACIL SOLUTIONS OBTAINED WITH DIFFERENT SOLVENTS

C. MOISESCU-GOIA<sup>1,2</sup>, M. MURESAN-POP<sup>3</sup>,  
V. SIMON<sup>1,3\*</sup>

**ABSTRACT.** The present study aimed to obtain new crystalline forms of 5-fluorouracil (5-FU) chemotherapy drug after 5-FU solvation in different solvents, considering the crystallization by slow evaporation. The expectation was to obtain 5-FU polymorphs. 5-FU was tested in aqueous solutions of 14 solvents. After slow evaporation of solutions (11) or suspensions (3), the obtained crystalline forms were examined by checking their X-ray diffraction patterns. Only for acetonitrile solution resulted a polymorph of 5-FU.

**Key words:** 5-fluorouracil; solubility; X-ray diffraction; polymorphs.

---

<sup>1</sup> Faculty of Physics & Interdisciplinary Research Institute on Bio-Nano-Sciences, Babes-Bolyai University, 400084 Cluj-Napoca, Romania

<sup>2</sup> Nuclear Medicine Department, Ion Chiricuta Institute of Oncology, 400015 Cluj-Napoca, Romania

<sup>3</sup> Interdisciplinary Research Institute on Bio-Nano-Sciences, Babes-Bolyai University, 400084 Cluj-Napoca, Romania

\* Corresponding author: [viosimon@phys.ubbcluj.ro](mailto:viosimon@phys.ubbcluj.ro)



## INTRODUCTION

Polymorphism has important consequences in the development of drugs. The existence of multiple crystal forms with differences in the solid-state properties can translate into significant effects on the bioavailability of the active drug substance [1].

The 5-fluorouracil is an efficient agent largely used in the clinical practice for treatment of solid tumors. It is an antimetabolite drug of pyrimidine class with antiviral and anticancer activities [2] and is one of the most effective chemotherapeutic agents administered in colorectal cancer treatment [3-5]. This chemotherapeutic agent has N–H donors and C=O acceptors (Fig. 1) and exhibits the diversity of hydrogen bonding motifs from a crystal engineering viewpoint [6].

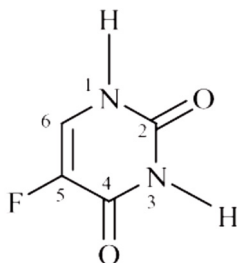


**Fig. 1.** Chemical structure of 5-fluorouracil

Nevertheless, 5-fluorouracil is sparingly soluble in water and slightly soluble in alcohol, and therefore the testing of its solubility in different solvents, as well as the identification of 5-fluorouracil polymorphs could be of biomedical interest. Such results are important also in the approach to obtain co-crystals or salts with proper cofomers for achieving new pharmaceutical solid forms which may be may influenced by a particular solvent system [7].

In this study we carried out a preliminar investigation on solubility and polymorphism of 5-fluorouracil compound by initial solvent screening for 14 solvents.

## EXPERIMENTAL

The test on the solubility and the identification of 5-fluorouracil (noted 5-FU) polymorphs was accomplished by solving 5-FU in different solvents, followed by crystallization at room temperature by slow solvent evaporation, and X-ray diffraction analysis of the resulted crystalline phases. The X-ray diffraction (XRD) patterns were recorded with a Shimadzu XRD-6000 diffractometer with graphite monochromator. The measurements were performed at room temperature, in  $2\theta$  range between 3–35°, with Cu  $K_{\alpha 1}$  radiation ( $\lambda = 1.5406 \text{ \AA}$ , operating conditions 40 kV and 30 mA).

An amount of about 20 mg 5-FU provided by Alfa Aesar was added to 1000  $\mu\text{l}$  of 14 solvents and the mixtures were heated at 40°C. The 1000  $\mu\text{l}$  of each solvent was progressively supplied in 5 steps of 200  $\mu\text{l}$  each one. Under these conditions the 5-FU dissolution was obtained only in water. Consequently, to the other solvents were added amounts of 200-500  $\mu\text{l}$  water (Table 1).

**Table 1.** Solubility test data

Crt.nr.	Solvent	5-FU (mg)	Added water ( $\mu\text{l}$ )	Observation
1	water	20.8	200	solution
2	ethanol	19.9	400	solution
3	dioxane	19.8	400	solution
4	acetonitrile	20.4	200	solution
5	2,2,2 trifluoroethanol	19.7	500	solution
6	n-heptane	19.6	400	suspension
7	ethylacetate	20.0	400	solution
8	toluen	19.5	400	suspension
9	3dimethyl-2butanone	20.7	400	suspension
10	dichloromethane	20.2	500	suspension
11	tetrahydrofuran	20.6	500	solution
12	etoxyethanol	19.8	500	solution
13	methanol	20.3	500	solution
14	2-butanone	20.1	500	solution

## RESULTS AND DISCUSSION

With respect to the solubility test, excepting the solvents based on n-heptane, toluen, 3 dimethyl-2butanone and dichloromethane which led to suspensions, in the case of all other solvents we could obtain 5-FU solutions after water addition to about 20 mg 5-FU and 1000  $\mu$ l solvent (Table 1).

The X-ray diffractograms recorded from the powdered samples obtained after slow evaporation show that the only sample which clearly delivers a different diffractogram from that of 5-FU is obtained for the sample resulted from the 5-FU solution with acetonitrile (Fig. 2), while all other samples deliver XRD patterns with the characteristic lines of 5-FU (Figs. 3 and 4).

The main characteristic signals in the diffraction line of 5-fluorouracil occur as a very intense peak at  $2\theta = 28.7^\circ$  and a much weaker one at  $2\theta = 16.3^\circ$ . Due to the very high intensity of the peak recorded at  $2\theta = 28.7^\circ$ , this was truncated in all XRD patterns.

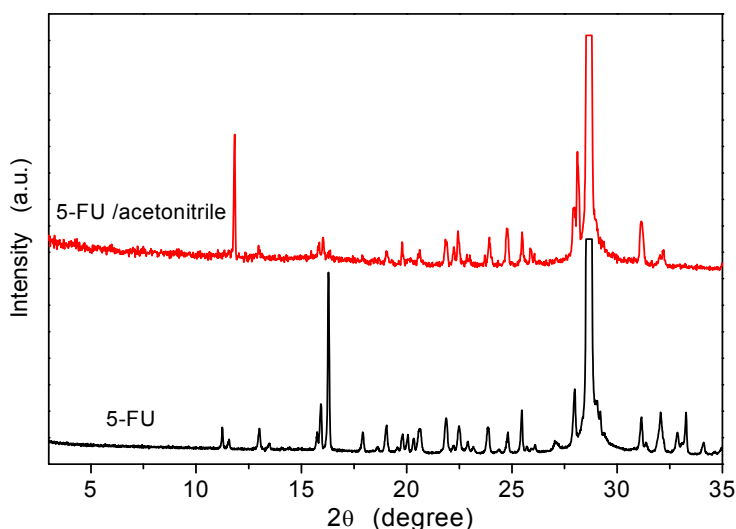


**Fig. 2.** XRD patterns of 5-FU and crystalline form resulted after evaporation of 5-FU solved in water solution with acetonitrile.

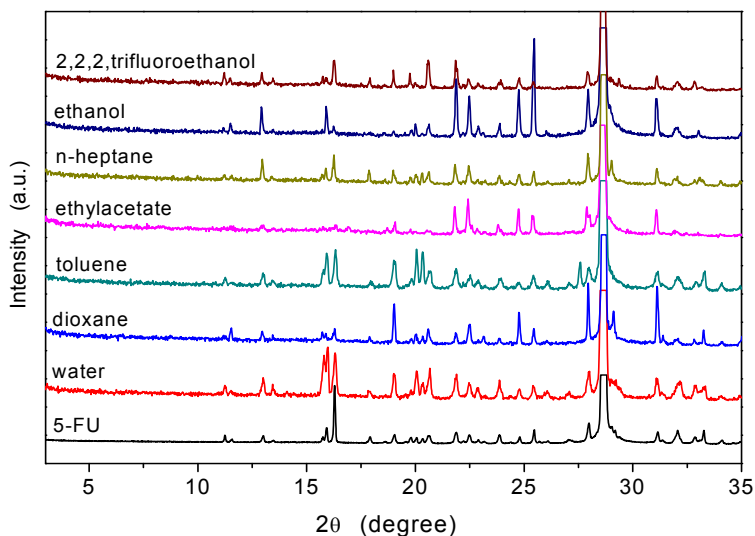


**Fig. 3.** XRD patterns of crystalline forms resulted after evaporation of 5-FU solved in water and in water solutions with dioxane, toluene, ethylacetate, n-heptane, ethanol and 2,2,2-trifluoroethanol.

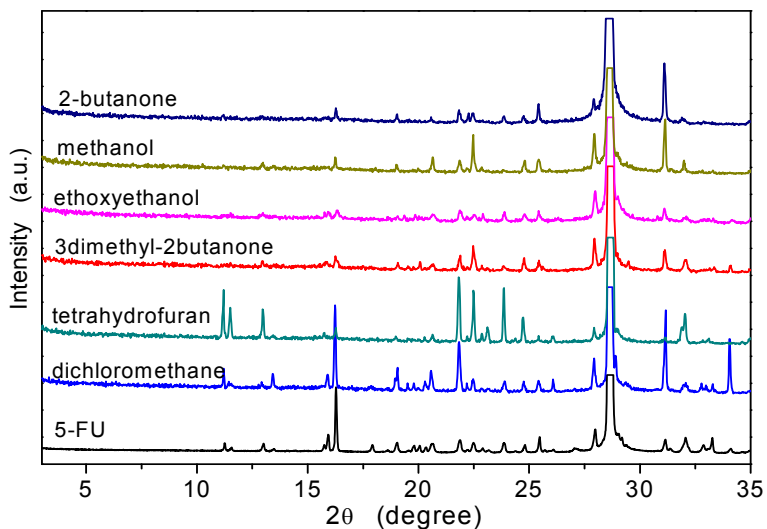


**Fig. 4.** XRD patterns of crystalline forms resulted after evaporation of 5-FU solved in water solutions with dichloromethane, tetrahydrofuran, 3-dimethyl-2butanone, ethoxyethanol, methanol and 2-butanone.

By checking the XRD patterns of the samples resulted by slow evaporation of 5-FU aqueous solutions with different solvents, it is first remarked a very pronounced enhancement of the diffraction line at  $2\theta = 28.7^\circ$  and the mentening of 5-FU signature (Figs. 3 and 4), excepting the crystalline form resulted from the solution with acetonitrile (Fig. 2). At the same time, one notices differences related to relative intensities of the diffraction peaks and this result can be primary assigned to occurance of 5-FU hydrated forms, because in hydrated forms the lattice constants are modified [8]. For the crystalline form obtained from acetonitrile aqueous solution the XRD pattern indicated the formation of a 5-FU polymorph, with crystaline structure different from that of 5-FU before solvation.

## CONCLUSIONS

The solubility of 5-fluorouracil (5-FU) chemotherapeutic agent was tested in 14 solvents: water, dioxane, toluene, ethylacetate, n-heptane, ethanol, 2,2,2-trifluoroethanol, dicloromethane, acetonitrile, tetrahydrofuran, 3-dimethyl-2butanone, ethoxyethanol, methanol and 2-butanone. By heating at  $40^\circ\text{C}$ , an amount of about 20 mg FU can be solved in 1.2 ml water or in aqueous solutions obtained by addition of 0.2-0.5 ml water to 1 ml solvent, excepting n-heptane, toluen, 3 dimethyl-2butanone and dichloromethane, in which, under these solubility test conditions appeared suspensions.

The structure of the samples resulted by slow evaporation of 5-FU solutions and suspensions was examined by checking their XRD patterns. Only for the crystalline form obtained from acetonitrile aqueous solution the XRD pattern indicates the formation of a 5-FU polymorph, while in all other cases the crystalline forms may are structurally similar to 5-FU before solvation and could be assigned to hydrated forms of 5-FU.

The 5-FU polymorph obtained by slow evaporation of acetonitrile aqueous solution could pay attention for further investigations related to new solid forms of 5-FU active drug substance.

## REFERENCES

1. M. Davidovich, J.Z. Gougoutas, R.P. Scaringe, I. Vitez, S. Yin, Detection of polymorphism by powder X-ray diffraction: Interference by preferred orientation, *Am. Pharm. Rev.*, 2004, 7, 10-16.
2. V. Sharma, N. Chitranshi, A.K. Agarwal, Significance and biological importance of pyrimidine in the microbial world, *Int. J. Med. Chem.*, 2014 (2014), Article ID 202784.
3. J.L. Grem, 5-Fluorouracil: Forty-plus and still ticking. A review of its preclinical and clinical development, *Invest. New Drugs*, 2000, 18, 299–313.
4. N. Zhang, Y. Yin, S.J. Xu, W.S. Chen, 5-Fluorouracil: Mechanisms of resistance and reversal strategies, *Molecules*, 2008, 13, 1551–1569.
5. D.B. Longley, D.P. Harkin, P.G. Johnston, 5-fluorouracil: Mechanisms of action and clinical strategies, *Nat. Rev. Cancer*, 2003, 3 330–338.
6. S. Li, J.-M. Chen, T.-Bu. Lu, Synthon polymorphs of 1 : 1 co-crystal of 5-fluorouracil and 4-hydroxybenzoic acid: their relative stability and solvent polarity dependence of grinding outcomes, *CrystEngComm*, 2014, 16, 6450-6458
7. A. Ainouz, J.-R. Authelin, P. Billot, H. Lieberman, Modeling and prediction of cocrystal phase diagrams, *International Journal of Pharmaceutics*, 2009, 374, 82-89.
8. G. Engelhardt, J. Felsche, P. Sieger, The Hydrosodalite System  $\text{Na}_{6+x}[\text{SiAlO}_4]_6(\text{OH})_x \cdot n\text{H}_2\text{O}$ : Formation, phase composition, and de- and rehydration studied by  $^1\text{H}$ ,  $^{23}\text{Na}$ , and  $^{29}\text{Si}$  MAS-NMR spectroscopy in tandem with thermal analysis, X-ray diffraction, and IR spectroscopy, *J. Am. Chem. Soc.*, 1992, 114, 1173-1182.



## SYNTHESIS AND CHARACTERIZATION OF POLYDOPAMINE-COATED GOLD NANORODS

L.C. ȘUȘU<sup>1</sup>, A.M. CRĂCIUN<sup>2</sup> and S. AȘTILEAN<sup>1,2\*</sup>

**ABSTRACT.** Biologically inspired polydopamine (Pd) has served as a universal coating of nanoparticles for various applications in nanobiotechnology research fields. In this study, we report the encapsulation of gold nanorods in Pd through the self-polymerization of dopamine molecules under alkaline conditions. The obtained core/shell nanoparticles were optically and morphologically characterized using UV-vis absorption spectroscopy, transmission electronic microscopy, dynamic light scattering and Zeta Potential measurements.

**Keywords:** *gold nanorods; polydopamine coating; surface plasmon resonance; transmission electronic microscopy; dynamic light scattering; Zeta Potential*

---

<sup>1</sup> Babeș-Bolyai University, Faculty of Physics, Biomolecular Physics Department, 1 M. Kogălniceanu str., 400084 Cluj-Napoca, Romania

<sup>2</sup> Babes-Bolyai University, Interdisciplinary Research Institute in Bio-Nano-Sciences, Nanobiophotonics and Laser Microscopy Center, 42 T. Laurian str., 400271, Cluj-Napoca, Romania

\* Corresponding author: [simion.astilean@phys.ubbcluj.ro](mailto:simion.astilean@phys.ubbcluj.ro)



## INTRODUCTION

In the last decade, nanoscience and biotechnology have shown great potential in developing nanoinstruments for use in biological applications such as biosensing, bioimaging and drug delivery. There has been a great appeal in gold nanoparticles (GNPs) over the last years because of their unique shape and size-dependent optical properties originating from their surface plasmon resonances (SPR), arising from the collective oscillations of free electrons at the nanoparticle surface upon interaction with light. The increasing interest in rod-shaped GNPs, also known as gold nanorods (GNRs), is due to the split of the SPR band into two modes: one longitudinal mode (LSPR), parallel to the long axis of the rod, and one transversal mode, perpendicular to the first. As a result of this split, GNRs can absorb light from the visible to the near-IR region of the electromagnetic spectrum by altering their aspect ratio. The biological tissues are transparent in the near-IR region, enabling the use of GNRs in a wide variety of applications such as biological imaging, drug delivery, therapy of cancerous cells, etc. [1].

A new challenge nowadays in bionanotechnology is the fabrication of nanoscale plasmonic devices with high stability, low cytotoxicity and good biocompatibility to be used in practical applications as in-vivo or in-vitro assays. Because of its ease to use and fascinating properties, polydopamine (Pd) has attracted considerable interest in this matter [2]. Dopamine, a well-known neurotransmitter, can undergo self-polymerization onto many solid surfaces at alkaline pH conditions forming robust adherent Pd films [3,4]. The surface of Pd contains amino and catechol groups, allowing for further conjugation with bio-molecules [5]. More interestingly, Pd coating has been reported to be very biocompatible and stable for in vitro and biomedical applications [6]. Recently, Pd-coated NP have shown great attraction in biological applications, like bioimaging, biosensing, and photothermal therapy, due to their ease of formation, good stability and special molecular absorption [7]. For example, Ju and co-workers designed a dual-mode nanocomplex for magnetic resonance and Raman imaging based on Pd-capped hollow GNPs

conjugated with bio-molecules [8]. On the other hand, Pd-coated GNRs were demonstrated to be efficient in targeted photothermal therapy of breast and oral cancer cells [9]. More recently, Wang *et al.* synthesized Pd-capped GNRs loaded with methylene blue and doxorubicin, for multifunctional drug delivery and multimodal light-mediated therapy [10].

In this paper, we successfully enveloped GNRs in a Pd shell by using dopamine as precursor and adjusting the pH of GNRs's solution to an appropriate alkaline value to ensure polymerization. The coating of GNRs in Pd was experimentally confirmed by UV-vis absorption spectroscopy, transmission electron microscopy (TEM), dynamic light scattering (DLS) and Zeta Potential measurements.

## EXPERIMENTAL DETAILS

### Chemicals

Tetrachloroauric acid ( $\text{HAuCl}_4 \cdot 4\text{H}_2\text{O}$ , 99.99%), cetyltrimethylammonium bromide (CTAB), ascorbic acid and dopamine hydrochloride ( $(\text{HO})_2\text{C}_6\text{H}_3\text{CH}_2\text{CH}_2\text{NH}_2 \cdot \text{HCl}$ , 98%) were purchased from Sigma-Aldrich. Sodium borohydride ( $\text{NaBH}_4$ , 99%), silver nitrate ( $\text{AgNO}_3$ ) and sodium nitrate ( $\text{NaOH}$ ) were obtained from Merck. All chemicals were used without further purification. Ultrapure water (resistivity  $\sim 18.2 \text{ M}\Omega$ ) was used as the solvent throughout the experiments.

### Synthesis of CTAB - stabilized GNRs

A seed-mediated approach was used in this study for the synthesis of GNRs with different aspect ratios. First, gold seeds were prepared by mixing 1.25 ml of 0.2 M CTAB with 1.25 ml of 5mM  $\text{HAuCl}_4$ . Next, 0.9ml of freshly prepared ice cold 1 mM  $\text{NaBH}_4$  solution was added all at once, resulting in a brownish-yellow seed solution [11].

In order to obtain the growth solution, a total of 10ml of 0.2 M CTAB was first gently mixed with 10ml of 1mM HAuCl<sub>4</sub> and various amounts of 4mM AgNO<sub>3</sub>, adjusted in order to tune the aspect ratio of GNRs. Ascorbic acid was then added to the solution as a mild reductant agent (78.8 mM, 0.15 ml) changing the color of the growth solution from dark yellow to colorless, followed by the addition of 0.024 ml of the seed solution. The color of the solution changed in the first 20-30 min until final stabilization.

The obtained probes were centrifuged at 14000 rpm for 10 min to remove the excess CTAB surfactant and the obtained GNRs were resuspended in ultrapure water for further use [12].

### **Preparation of Pd-coated GNRs**

The pH of 1 ml CTAB-stabilized GNRs was altered from 5 to 8.5 through the addition of 100 mM NaOH solution. Next, we added into the solution 0.516 mM dopamine hydrochloride buffered to pH 8 using NaOH. The sample was allowed to react for 30 min and the GNRs suspension was sonicated for 15 min.

### **Experimental measurements**

The extinction spectra were recorded on a Jasco V-670 UV-Vis-NIR spectrophotometer with 1 nm spectral resolution. The morphology of the obtained GNRs was examined using a FEI Tecnai F20 field emission, high resolution TEM (TEM/HRTEM) operating at an accelerating voltage of 200 kV and equipped with Eagle 4k CCD camera. Dynamic light scattering (DLS) and Zeta Potential measurements were performed using a Zetasizer Nano ZS 90 from Malvern Instruments.

## RESULTS AND DISCUSSION

Fig. 1 displays the normalized extinction spectra of CTAB – stabilized GNRs with varying aspect ratio obtained in aqueous solution by varying the concentration of silver ions in the growing solution. As shown in the plot, all recorded spectra exhibit two localized surface plasmonic resonances (LSPR) corresponding to the light-induced electron oscillations perpendicular and parallel to the nanorod length direction.

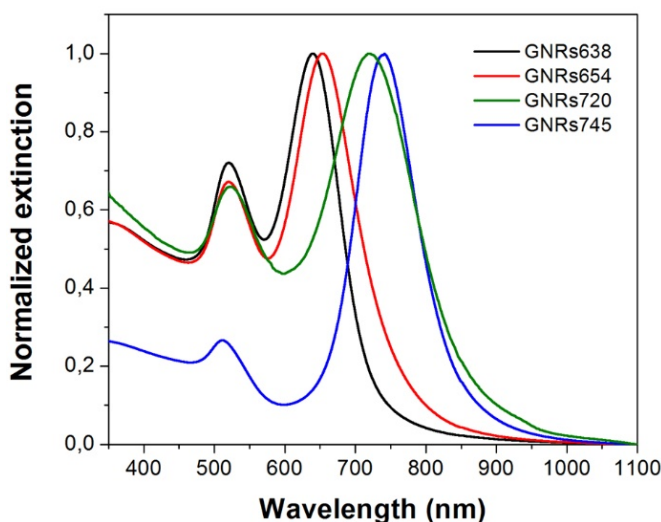


**Fig. 1.** Normalized extinction spectra of CTAB-stabilized GNRs with different aspect ratio.

The transversal band is located at around 520 nm for all the probes whereas the longitudinal band is tuned from 638 nm to 745 nm, confirming the successful synthesis of GNRs of increasing aspect ratio.

In view of future applicability in biomedical applications, we have selected for encapsulation in Pd the GNRs displaying longitudinal LSPR band in the biological window, at 745 nm (GNRs745). Fig. 2(a) shows the normalized extinction spectra of GNRs745 before and after coating with Pd

(Pd-GNRs745) together with the spectrum of Pd-coated GNRs recorded after long-time storage (*i.e.* 3 months). As shown, the longitudinal LSPR band undergoes a red shift from 745 nm to 757 nm after the formation of Pd at the surface of GNRs while the position of the transversal band remains almost unchanged. This red shift can be assigned to the increase of refractive index around the GNRs after Pd deposition. After long-time storage, the longitudinal LSPR band displays a slight blue shift, however the spectral shape of the spectrum remains unaltered indicating that the synthesized Pd-coated GNRs745 have good stability in time.

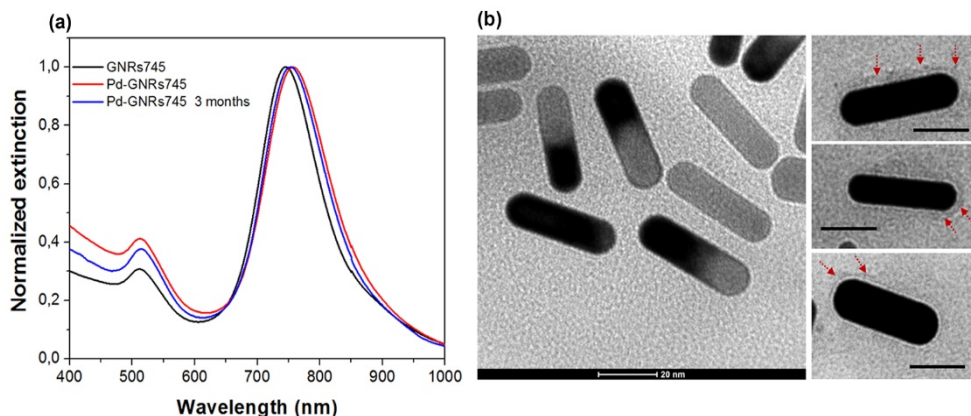


**Fig. 2.** (a) Normalized extinction spectra of GNRs745 before and after Pd coating and its evolution in time; (b) TEM images illustrating CTAB-stabilized GNRs745 (left) and Pd-coated GNRs745 (right). All scale bars have the same length (20 nm).

Further, we performed TEM measurements in order to evaluate the morphology of our samples. Fig. 2(b) (left), displaying a typical TEM image of CTAB-stabilized GNRs745, confirms the formation of GNRs monodisperse in size and shape with average length  $\times$  width of  $40 \times 12$  nm and an aspect ratio of 3.3. Moreover, TEM images presented in Figure 2(b) (right), confirm the

deposition of a 2-3 nm thick Pd shell (marked with red arrows) at the surface of GNRs. Future work is in progress in order to optimize the encapsulation procedure and obtain a more uniform Pd shell around the GNRs.

Subsequently, DLS and Zeta Potential measurements were performed in conjunction with absorption spectroscopy and TEM in order to validate the presence of Pd coating. Fig. 3(a) reveals an increase of the hydrodynamic diameter, after Pd coating, indicating the presence of an extra layer at the surface of the nanorods, thus confirming the results obtained from TEM. Zeta Potential measurements (Fig. 3(b)) were performed to analyze the change in surface charge at the surface of GNRs. As displayed, the charge value dropped from +48.7 mV to +31 mV after Pd deposition, which can be attributed to the catechol and -OH groups from the surface of the Pd shell [13]. Moreover, the slightly small change observed after 3 months of storage in the hydrodynamic diameter and Zeta Potential indicate once more the good stability of Pd – GNRs745 in time.

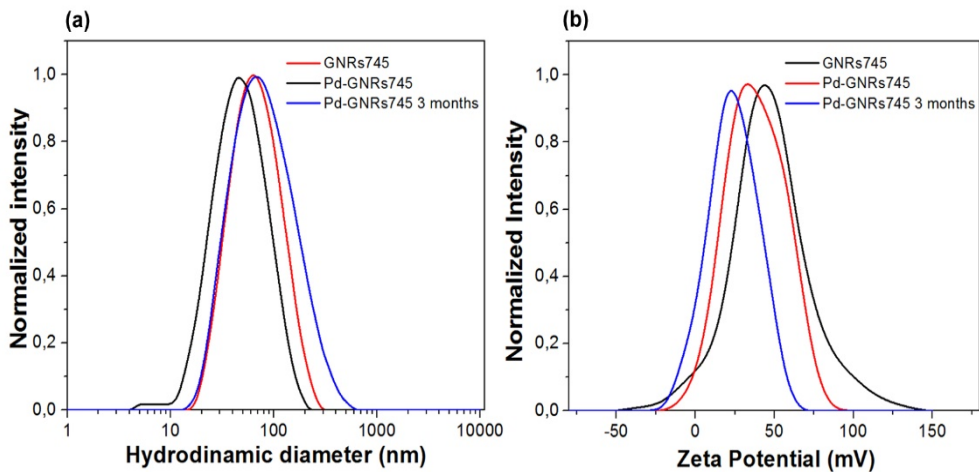


**Fig. 3.** Hydrodynamic diameter (a) and Zeta Potential (b) of GNRs745 before and after Pd deposition and their evolution in time.

## CONCLUSIONS

In conclusion, we have successfully synthesized stable core/shell nanoparticles by coating GNRs with Pd shell. The first evidence of successful coating with Pd is the 12 nm red shift of the longitudinal LSPR peak occurring as a consequence of dielectric constant modification after polymerization of dopamine. The nanocomposites were morphologically characterized using TEM, which further revealed the presence of a 2-3 nm Pd layer around GNRs. Finally, DLS and Zeta Potential measurements confirmed the presence of the Pd layer at the surface of the nanorods and their good stability in time, even 3 months after the coating procedure. Further improvement of the encapsulation process and adjustment of Pd shell thickness can lead to valuable platforms for various biomedical applications.

## ACKNOWLEDGMENTS

This work was supported by CNCS - UEFISCDI, Romania, under the project number PN-III-P4-ID-PCE-2016-0837.

## REFERENCES

1. Z.Y. Ma, H.X. Xia, Y.P. Liu, B. Liu, W. Chen, Y.D. Zhao, *Chin Sci Bull*, 58, 2530 (2013).
2. X. Liu, J. Cao, H. Li, J. Li, Q. Jin, K. Ren, J. Ji, *ACS Nano*, 7, 9384 (2013).
3. H. Lee, S.M. Dellatore, W.M. Miller, P.B. Messersmith, *Science*, 318, 426 (2007).
4. Y. Liu, K. Ai, L. Lu, *Chem. Rev.*, 114, 5057 (2014).
5. W. Tao, X. Zeng, J. Wu, X. Zhu, X. Yu, X. Zhang, J. Zhang, G. Liu, L. Mei, *Theranostics*, 6, 470 (2016).

6. S. Hong, K.Y. Kim, H.J. Wook, S.Y. Park, K.D. Lee, D.Y. Lee, H. Lee, *Nanomedicine*, 6, 793 (2011).
7. M.E. Lyngge, P. Schattling, B. Stadler, *Nanomedicine*, 10, 2725 (2015).
8. K.-Y. Ju, S. Lee, J. Pyo, J. Choo, J.-K. Lee, *Small*, 11, 84 (2015).
9. K. CL Black, J. Yi, J. G. Rivera, D.C. Zelasko-Leon, P.B. Messersmith, *Nanomedicine*, 8, 17 (2013).
10. S. Wang, X. Zhao, S. Wang, J. Qian, S. He, *ACS Appl. Mater. Interfaces*, 8, 24368 (2016).
11. B. Nikoobakht, M.A. El-Sayed, *Chem. Mater.*, 15, 1957 (2003).
12. V. Sharma, K. Parka, M. Srinivasarao, *PNAS*, 106, 4981 (2009).
13. D.R. Dreyer, D.J. Miller, B.D. Freeman, D.R. Paul, C.W. Bielawski, *Langmuir*, 28, 6428 (2012).





# SIMPLE METHOD FOR DIGITAL DATA RECORDING OF DAMPED OSCILLATIONS OF MECHANICAL PENDULUM

M. TODICA<sup>1\*</sup> and C. V. POP<sup>1</sup>

**ABSTRACT.** A simple method for digital data acquisition of low frequency damped oscillations of mechanical pendulum is proposed. The method use very simple equipment available in every didactic laboratory. It is intended for didactic purpose, but the method can be used for scientific investigations also.

**Keywords:** *digital data recording, low frequency oscillations, mechanical pendulum*

## INTRODUCTION

The digital acquisition of data is today a very common stage of every scientific experiment, being performed with equipments implemented in every modern system for experimental investigation. This situation facilitates a rapid and reliable acquisition of data without special skills requested to the

---

<sup>1</sup> Babes-Bolyai University, Faculty of Physics, M. Kogalniceanu No 1, 400084 Cluj-Napoca, Romania

\* Corresponding author: [mihai.todica@phys.ubbcluj.ro](mailto:mihai.todica@phys.ubbcluj.ro)

user, [1-4]. However the simplicity of the use is paid some time by the incomplete understanding of the physics and mathematics implemented into the sophisticate procedure of data acquisition. This knowledge lacking leads to the impossibility to adjust or to improve the parameters of the acquisition. Creating an opportunity to operate inside the protocol of data recording represents the aim of this work. We propose a simple method for digital data acquisition of the damped oscillations of the mechanical pendulum using only an ordinary computer mouse, a common computer and the software Processing, available free on the internet. The method is intended for application in the didactic experiments, being accessible to a large category of population. Despite the simplicity the collected data are very accurate and can be used also for scientific investigations.

## EXPERIMENTAL

The main piece of the experimental set-up is a home-made mechanical pendulum attached to a common CD which rotates in front of an optical mouse (Fig. 1). The pendulum is made from a thin and light rod of aluminium or steel of length  $l=33\text{ cm}$  and neglecting mass and a small heavy body of mass  $m=0.73\text{ g}$ . The length and the mass of pendulum can be set according to the necessities of the experimentations. The other end of the rod is attached to the CD, which can rotate around a fixed axle passing through its mass center. It is suitable to use a bearing in order to reduce at minimum the friction and to ensure a stable plan of rotation. We used for this purpose an old computer hard disc drive, (HDD). Only the mechanical bearing is used, the other parts, like the lecture head and the positioning system of the head, are eliminated. This system ensures a very precise plan of oscillations and very small friction. In front of the CD, on the vertical plane of the pendulum, we placed an optical mouse, at  $0.5\text{-}1\text{ mm}$  distance from the CD, avoiding any

friction with the CD. The distance between the axle of the CD and the optical sensor of the mouse is  $b=5\text{ cm}$ . When the pendulum oscillates, the CD move in front of the mouse that is equivalent with a motion of the mouse along a segment of circle. The position of the mouse is transformed by its processor on  $X$  and  $Y$  coordinates transmitted to the computer. We process these coordinates in order to display and calculate the parameters of the oscillation.

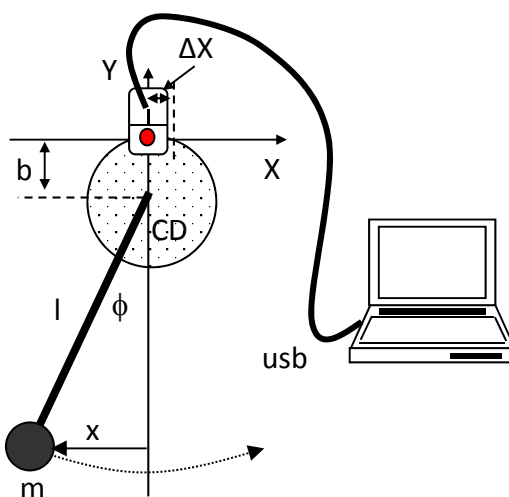


**Fig. 1.** Schematic representation of the experimental setup.

## RESULTS AND DISCUSSION

Digital data acquisition from a moving object supposes the use of adequate motion sensor. Usually mechanical or optical encoders dedicated to each application are used. The accuracy of measurements depends on the resolution of the sensor. The accuracy is defined by the rate of digital sampling

per unit of length. More the resolution is high more the sensors are complex and expensive. A simple solution is the use of an optical mouse. Usually such device has a resolution of hundreds of dpi/mm, enough to ensure tens of readings for displacements of the order of few millimeters. Such characteristics are adequate to our situation. Small oscillations of the pendulum, of angles less than 4 degrees, determine a displacement of the CD in front of the optical sensor of the mouse  $\Delta X = b \cdot \sin\phi \cong b \cdot \phi$  of the order of few millimeters. This displacement is equivalent with a displacement of the optical mouse of the order of tens of digital points along the OX axis. In the ordinary computer the data read by the mouse are transferred directly to the processor, being not accessible for external use. However we can read and display on the PC the coordinates of the mouse using Processing software. To do this we must download the this software from official site and install it on the computer, [5]. Then we upload the following code:

```
//The code

import processing.serial.*;
int start;
int count;
int prevX=200;
int X=100;
void setup() {
  size(600, 400);
  background(255);
  smooth();
}

void draw() {
  int X =mouseX;
  if(X>prevX) {
    start = millis();
    count++;
  }
}
```

```

    stroke(0);
    ellipse(X,count,5,5);
    prevX=X;
  }
  if(X<prevX) {
    start = millis();
    count++;
    stroke(0);
    ellipse(X,count,5,5);
    println(X,"",count,"");
    prevX=X;
  }
}

//End of the code.

```

The code starts automatically if the pendulum is moving. It is enough to displace the oscillating body from its equilibrium position and leave it to oscillate freely. Processing read the coordinate  $X$  of the mouse and starts automatically the time counter. The instruction for reading the  $X$  coordinate is:

```
int X =mouseX;
```

The current position of the mouse is compared with the previous value.

```

if(X>prevX) {
  start = millis();
  count++;
}

```

If the new value is greater than the previous, the counter is started. The variable *count* measures the time of data sampling. In our code the sampling is performed to each millisecond. The counter is started also if the current coordinate is smaller than the previous.

```

if(X<prevX) {
  start = millis();
  count++;
}

```

If one of these conditions are fulfilled, the computer receive the instruction to draw a small circle with radius 5 points, centered at (count, X).

```
stroke(0);  
ellipse(X,count,5,5);
```

The amplitude of oscillations, designed by the variable *X*, and the time, designed by the variable *count*, are graphically represented in the working windows of Processing. In the same time the data are written in two columns of the Processing working windows, (Fig. 2).

```
println(X,"",count,"");
```

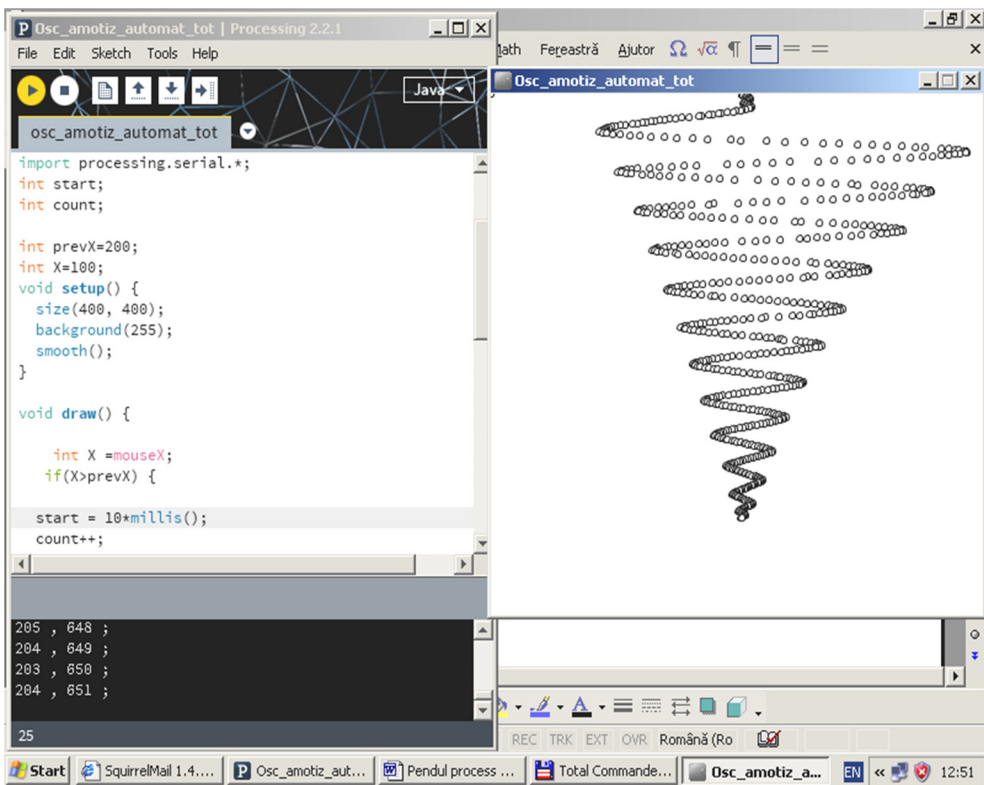


**Fig. 2.** Print screen of damped oscillations recorded with Processing. The data are automatically printed on the window workspace of Processing.

When the pendulum stops to oscillate, the acquisition of data is stopped. We can copy the data and analyze them with specific software like Origin or Kaleidagraph. Some theoretical considerations are necessarily in order to process the experimental data.

It is well known that the oscillations of the simple pendulum are determined by the tangential component of the gravity force acting on the body mass of the pendulum  $G_t = -m \cdot g \cdot \sin \phi$ . For small angles of deviation  $\sin \phi \cong \phi$ , and the displacements of the oscillating body from its equilibrium position is described by the equation  $x = l \cdot \sin \phi \cong l \cdot \phi$ . Applying these approximations we can write  $G_t \cong -m \cdot g \cdot \phi = -\frac{m \cdot g \cdot x}{l}$ .  $l$  represents the length of the pendulum and  $\phi$  the angle of deviation from the equilibrium position. In these conditions the force governing the oscillations is an elastic force of the form  $\overset{P}{F} = -k \cdot \overset{P}{x}$ , where the elastic constant  $k$  is given by the relation  $k = \frac{m \cdot g}{l}$ . We can apply all the equation of the elastic oscillator to describe the motion of the pendulum. If the oscillation of the pendulum is subject of friction with the coefficient  $\mu$ , then the motion of the system is described by the equation:

$$m \frac{d^2 x}{dt^2} = -kx - \mu \frac{dx}{dt} \quad (1)$$

The solution of this equation is a damped oscillation:

$$x = A \cdot \exp(-\alpha t) \cdot \sin(\omega t) \quad (2)$$

$A$  represents the amplitude,  $\alpha$  the attenuation coefficient and  $\omega$  the pulsation of the damped oscillation. The relation existing between the parameters  $\alpha$ ,  $\omega$ ,  $m$  and  $k$  are described by the equations:

$$\alpha = \frac{\mu}{2m}, \quad \omega^2 = \frac{k}{m} - \frac{\mu^2}{4m^2} = \frac{g}{l} - \frac{\mu^2}{4m^2} \quad (3)$$



The period of the damped oscillation  $T = \frac{2\pi}{\omega}$  is greater than the period of the ideal oscillations

$$T_0 = \frac{2\pi}{\omega_0}, \quad \text{where } \omega_0^2 = \frac{k}{m} = \frac{g}{l}, \quad [6].$$

We are interested to measure and calculate the parameters of the real oscillations and compare them with those of the ideal pendulum. Experimentally we can measure the period and the amplitude of the damped oscillations, but we cannot directly measure the attenuation or the friction coefficients. These parameters can be obtained only by calculation. The amplitude of oscillations is affected by the attenuation coefficient  $\alpha$  following an exponential law, [7]. Measuring the amplitudes  $A(T_i)$  of damped oscillations at different instants  $T_i$ , we can calculate the attenuation coefficient  $\alpha$  from the representation:

$$A(T_i) = A_0 \exp(-\alpha T_i) \quad (4)$$

We can also calculate this coefficient from the logarithmic decrement of the oscillations,  $\Lambda = \frac{A_2}{A_1}$ . To do this we must measure the amplitudes  $A_1$  and  $A_2$  of two successive oscillations separated by a time interval equal with a period.  $\Lambda$  represents the rate of loss of mechanical energy  $W$  during a period, [8]. Taking into account the attenuation of the amplitude, we can find a direct relation between  $\alpha$  and  $\Lambda$ .

$$\frac{W_2}{W_1} = \exp(-2\alpha T) = \Lambda^2 \quad \alpha = -\frac{\ln \Lambda}{T} \quad (5)$$

Knowing  $\alpha$ ,  $m$ , and  $T$  we can calculate the friction coefficient  $\mu$ .

The experimental oscillations are presented in figure 3. From these data we measured the period  $T$  of the damped oscillations and we read the amplitudes  $A(T_i)$  of the oscillations. We found the value  $T = 1.23$  s. This value

is smaller than the period of ideal oscillations  $T_0=1.15$  s calculated with the relation  $T_0 = 2\pi\sqrt{\frac{l}{g}}$ . Using the equation (4) we calculated the attenuation coefficient  $\alpha$ . We found the value  $\alpha = 0.27$  s<sup>-1</sup>. The value of  $\alpha$  was also calculated from the logarithmic decrement of the oscillations using equation (5). We took two successively values of amplitudes  $A_1 = 123$  a.u and  $A_2 = 94$  a.u. We obtained the value  $\alpha = 0.268$  s<sup>-1</sup>. The values determined by both methods are in good agreement. Using this value of  $\alpha$ , the measured values of  $T$  and  $m$ , we calculated the friction coefficient  $\mu$  with the equation  $\mu = 2m \cdot \alpha$ . We found the value  $\mu = 0.039$ . We calculated also the elastic constant  $k$  with the equation (3). We found the value  $k = 2.167$  N/m. To verify our result, we used the values  $\alpha, \mu, m$  and  $T$  to fit the experimental data with the equation (2). The result of the fit is shown in figure 3. We can see a good agreement between the experimental data and the simulation.

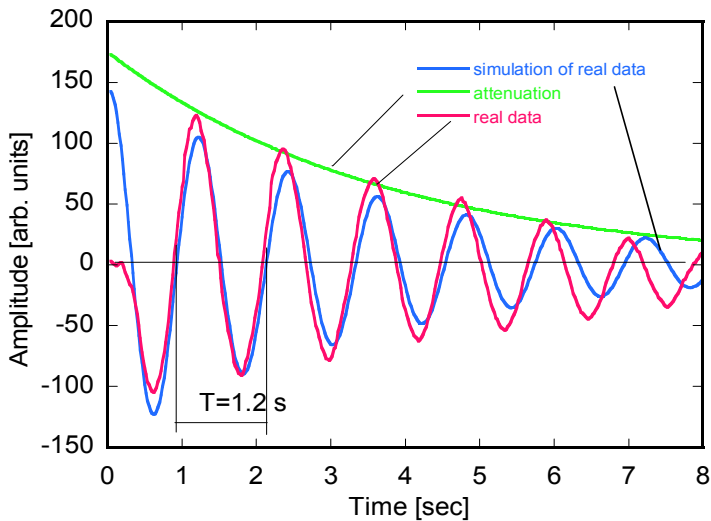


**Fig. 3.** Representation of real data, simulation of data with the calculated parameters and the theoretical attenuation

## CONCLUSION

A simple method for digital data recording of oscillations of mechanical pendulum was presented. The method allows quantitative calculation of the parameters of the oscillations. The method is based on the use of very simple equipment, which can be "home made", and free software available on the internet. The method can be used for scientific experiments but also for didactic purpose, allowing the user to better understanding the principles of digital data acquisition.

## REFERENCES

1. S.D. Anghel, *Bazele Electronicii analogice și digitale*, Presa Universitară Clujeană, Cluj-Napoca, 2007, ISBN: 978-973-610-554-8.
2. I. Burda, *Microprocesoare și microcontrolere*, Presa Universitară Clujeană, Cluj-Napoca, 2002, ISBN 973-610-046-4.
3. D. Rădoi, G.D. Popescu, *Introducere în știința sistemelor de calcul*, Editura Universității "Petru Maior", Târgu-Mureș, 1999, ISBN 973-98726-7-0.
4. A. Nicula, M. Todica, G. Buzas, S. Astilean, I. Berindean, *Studia UBB Physica*, XXXIII, 2, (1988), 15-19.
5. <https://processing.org/download/>
6. R.M. Eisberg, L.S. Lerner, *Physics Foundations and Applications*, McGraw-Hill, London, 1982, ISBN 0-07-066268-1.
7. B.M. Yavorsky and A.A. Pinsky, *Fundamental of Physics*, Mir Publishers, Moscow, 1987.
8. M. Todica, C.V. Pop, *Fizică generală aplicată*, Presa Universitară Clujeană, Cluj-Napoca, 2007, ISBN (10)973-610-498-2; ISBN (13) 978-973-610-498-5.

## CONFORMATIONAL SPACE AND ELECTRONIC ABSORPTION PROPERTIES OF THE TWO ISOMERS OF RESVERATROL

RÉKA-ANITA DOMOKOS<sup>1</sup>, V. CHIŞ<sup>1\*</sup>

**ABSTRACT.** The present study analyses the *trans* and *cis* conformations of resveratrol, aiming to get clear experimental and computational evidences that can be used to differentiate between the two isomers. Three conformers for each isomer have been considered and their characteristic geometrical parameters, relative free energies, Boltzmann populations and electronic transitions have been calculated at B3LYP/6-31+G(2d,2p) level of theory in gas phase, as well as in water, ethanol and DMSO. The experimental UV-Vis spectra of the two isomers have been explained by using the time dependent density functional theory (TD-DFT) formalism.

**Keywords:** *trans-resveratrol*; *cis-resveratrol*; *conformational analysis*; *UV-VIS*

---

<sup>1</sup> Babeş-Bolyai University, Faculty of Physics, 1 Kogălniceanu, RO-400084 Cluj-Napoca, Romania

\* Corresponding author: [vasile.chis@phys.ubbcluj.ro](mailto:vasile.chis@phys.ubbcluj.ro)

## INTRODUCTION

Resveratrol (3, 5, 4'- trihydroxystilbene - RESV) has been proven to be a strong antioxidant and anti-inflammatory compound, showing also beneficial effects for treating diseases like heart failure, breast and prostate cancers, stroke, brain damage, etc. [1-4]. RESV is found in red grapes and wine [5] and it is widely believed to be responsible for the "French Paradox" which describe the low incidence of heart disease and obesity among the French in contrast to their relatively high-fat diet [6]. The structure of RESV consists of two phenols linked by a double bond which facilitates two isomeric forms, called *trans*- (E) - and *cis*- (Z) resveratrol (Fig. 1). The biological activity of RESV seems to be primarily due to its *trans*-isomer, while the *cis* isomer is obtained by UV-irradiation of the *trans*-RESV [7].

In spite of its structural simplicity and of a wealth of spectroscopically data reported in the literature about RESV, its structural isomers, particularly the *cis* form, have not been yet fully characterized.

The solid state structure of *trans*-resveratrol was studied by X-Ray technique [8] being shown that these molecules in solid phase are interconnected by an extensive hydrogen bond network. On the other hand, to the best of our knowledge, no information related to structural parameters of the *cis* isomer has been reported so far.

The spectroscopic response of various isomers of a compound can be significantly different. This is particularly important for UV-VIS spectra, but also for other spectroscopic techniques. That's why we analyzed in this study the two isomeric forms of resveratrol, aiming to get clear experimental and computational evidences that can be used to differentiate between the two conformers. In order to obtain new information about the structure and the electronic properties of both isomers, this study has been conducted using the UV-VIS spectroscopy coupled to methods of computational spectroscopy based on DFT and TD-DFT formalisms. Molecular structures of the isomers and their energetic stability was investigated in gas phase, as well as in liquid phase (ethanol, water and DMSO).

## EXPERIMENTAL AND COMPUTATIONAL DETAILS

The two isomeric forms (*trans* (E-) and *cis* (Z-)) of RESV compound were purchased from Cayman Chemical and used as received. *Trans*-resveratrol was supplied in powder form with a purity  $\geq 98\%$  and *cis*-resveratrol as a solution in ethanol with a purity  $\geq 98\%$ .

Optical absorbance spectra of the two isomers were recorded at room temperature using a Jasco V-630 UV-Vis double beam spectrophotometer with a slit width of 2 nm. The spectra of both isomers have been recorded in ethanol at different concentration.

Geometry optimizations and single point calculations were performed with the Gaussian 09, revision E.01 software package [9] by using DFT approaches. The hybrid B3LYP exchange-correlation functional [10-12] was used in conjunction with Pople's split valence 6-31+G(2d,2p) basis set [13-14]. Absorption spectra for both isomer of RESV were calculated using the time-dependent DFT (TD-DFT) methodology [15], implemented in the Gaussian09 package. The simulated UV-vis spectrum of RESV in the 180–500 nm range has been obtained by summation of the contributions from transitions to the first 30 singlet excited electronic states. The UV spectral line-shapes were convoluted with Gaussian functions with the full width at half maximum of 0.33 eV. The nature of the excited states has been analyzed using the Natural Transition Orbitals (NTO) formalism [16].

Solvent effects on the vertical excitation energies were also considered by using the implicit Polarizable Continuum Model (PCM) of solvation [17].

## RESULTS AND DISCUSSIONS

Our first interest was to investigate the stability of the possible conformers of RESV in both isomeric forms. The starting geometries of *trans*-RESV used for geometry optimizations were derived from the X-ray

diffraction data reported by Caruso *et al.* [8]. For *cis*-RESV the starting geometries were obtained by a dihedral distortion of the *trans* isomer around the C7-C8 olefin bond (see atom numbering scheme in Fig. 1).

Depending on the mutual orientation of the OH bonds in RESV, three different conformers have been analyzed for each isomer and they are shown in Fig. 1. A good agreement is observed between the solid state structure of *trans*-RESV and that of its *c2* conformer in gas-phase. Thus, the shortest calculated bond for the *c2-trans*-RESV (1.348 Å) is the olefin C7=C8 bond, as it was also observed in solid state, where the corresponding bond length is 1.333 Å [8]. It remains the shortest bond for all conformers of the two isomers, with values in the 1.349-1.350 Å interval. The calculated aromatic CC bond lengths are between 1.387 – 1.409 Å (1.37 – 1.40 Å – experimental) and the calculated longest bonds correspond to the olefin-phenyl bonds, 1.466 Å for the C1-C7 bond and 1.463 Å for the C8-C9 bond (experimental values are 1.468 Å and 1.460 Å, respectively [8]). All the C-O bonds are predicted longer by calculations and this fact can be explained by the extended network of hydrogen bonds in which the OH groups are involved in solid state.

The calculations reproduce also very well the non-planarity of this isomer. Thus, the calculated dihedrals that give the non-coplanarity of the olefin moiety with the two phenyl rings are 5.97° and 4.97° for di-*m*-OH and *p*-OH rings, respectively. The calculated dihedral angle between the planes defined by the two rings is 11.06 Å, slightly larger than the experimental value (5.30 Å [8]). Solid state structure of *trans*-RESV shows that the two hydroxyl groups in the di-*m*-OH phenyl are almost coplanar with the ring, while in case of *p*-OH phenyl ring the OH bond is out of plane by 51.09° [8]. However, since the intermolecular hydrogen bond interactions were not considered in this study, for the isolated *trans*-RESV molecule, the three OH bonds are predicted coplanar with the phenyl rings, for all the conformers of *trans*-RESV, both in gas-phase and in solution.

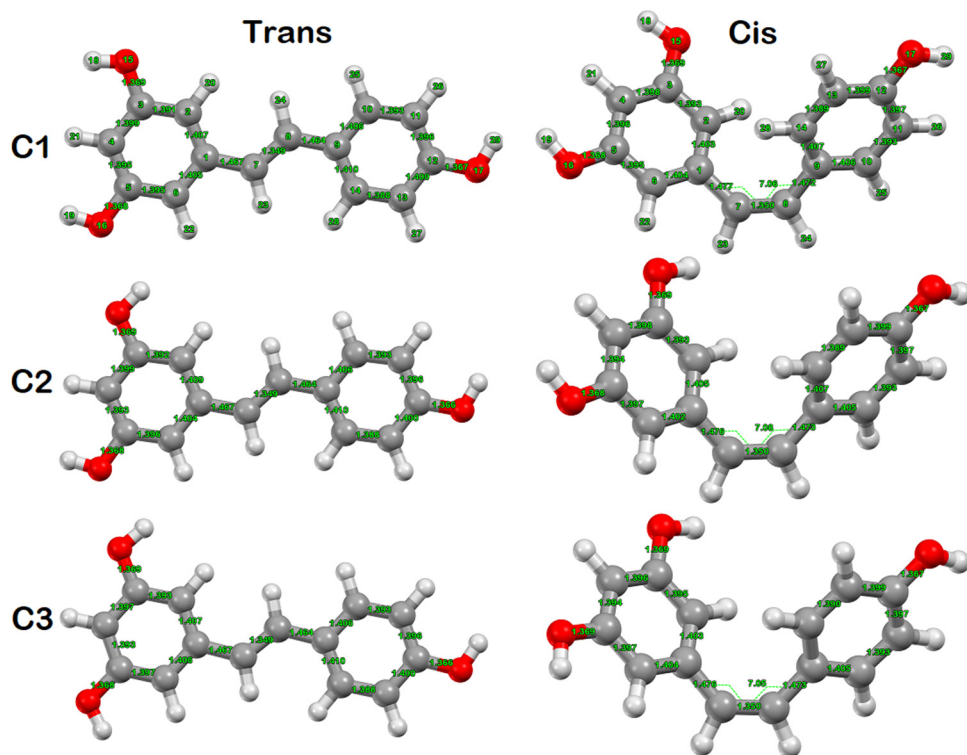


**Fig. 1.** PCM-B3LYP/6-31+G(2d,2p) optimized geometries of *trans*- (left) and *cis*- (right) resveratrol in ethanol

The calculated geometrical parameters for all the three conformers of the *trans*- and *cis*-RESV in ethanol are shown in Fig. 1. Computational data show that for the conformers of both isomers, the bond lengths as well as the valence and dihedral angles suffer minor changes between the gas and solution phases.

Comparing the geometrical parameters of the two isomers, as expected, the most pronounced differences were observed for the C1-C7 and C9-C10 bonds which become slightly longer for the *cis* isomer. It is worth noting that the C7=C8 double bond remains practically unchanged between the isomers and does not change also as a result of transition between the gas and liquid states.



Moreover, the most important changes of the valence angles (however, less than  $5^\circ$ ) are predicted by calculations for the C2-C3-O15 and C1-C7-C5 angles. The first one decreases by  $5^\circ$ , while the latter increases by about  $4^\circ$  when going from the *trans*- to the *cis* isomer.

Obviously, the largest changes between the isomers are observed for the dihedral angles defining the orientation of the two phenyl rings relative to olefin moiety. Thus, the C1-C7-C8-C9 dihedral angle changes from  $180^\circ$  for the *trans* isomer to  $7^\circ$  in case of *cis* conformation. In ethanol, the deviation from the Ph-olefin coplanarity, characteristic for the *trans* isomer, is predicted to be of  $37.8^\circ$  for the di-*m*-OH phenyl and  $27.1^\circ$  for the *p*-OH phenyl, in case of the *cis* isomer. Similar distortions were predicted in gas phase.

### 2D and 1D potential energy surfaces (PESs) of Resveratrol

The relaxed 2D PES of resveratrol in gas-phase (Fig. 2) has been calculated at B3LYP/STO-3G level of theory, by varying the C6-C1-C7-C8 and C7-C8-C9-C10 dihedrals (marked with a star in the left upper corner of Fig.2) in steps of  $10^\circ$ , within the  $0 \div 180^\circ$  interval.

Two stationary points have been identified on the 2D PES; the global minimum ( $GM_{2D}$ ) is four-fold degenerate due to the symmetry of the molecule and it corresponds to the *trans* isomer. The same is true for the saddle point ( $SP_{2D}$ ) which adopts a structure with the two phenyl rings making a dihedral angle of  $80.1^\circ$ . The global maximum ( $MAX_{2D}$ ) has a stair-like structure, with the planes of the phenyl rings being parallel and the plane containing the olefin bond perpendicular to the phenyl rings.

The energetic difference between the  $GM_{2D}$  and  $SP_{2D}$  is 5.65 kcal/mol, and the  $MAX_{2D}$  structure is 6.28 kcal/mol above the  $SP_{2D}$ .

However, none of the points of the 2D PES corresponds to the *cis* isomeric form. Such a structure can only be obtained by performing a rotational scan around the C=C bond. The relaxed 1D PES in ethanol has been obtained by varying the H23-C7-C8-H24 dihedral with a step of  $10^\circ$ , within the  $-180^\circ \div 180^\circ$  interval (see Fig. 3).

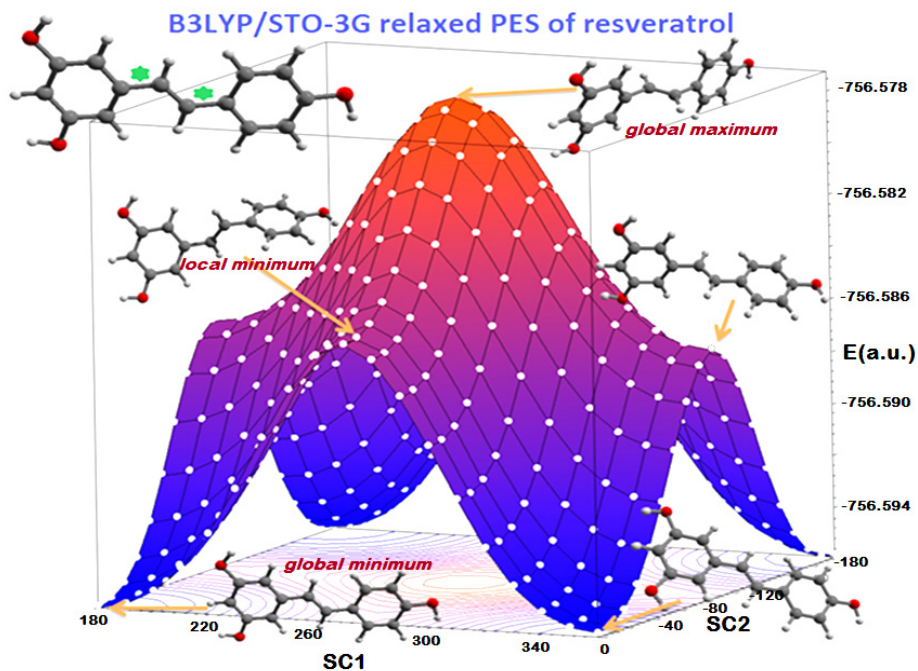


**Fig. 2.** Relaxed 2D PES of *trans*-RESV (c2 conformer) calculated at B3LYP/STO-3G level of theory, in gas-phase

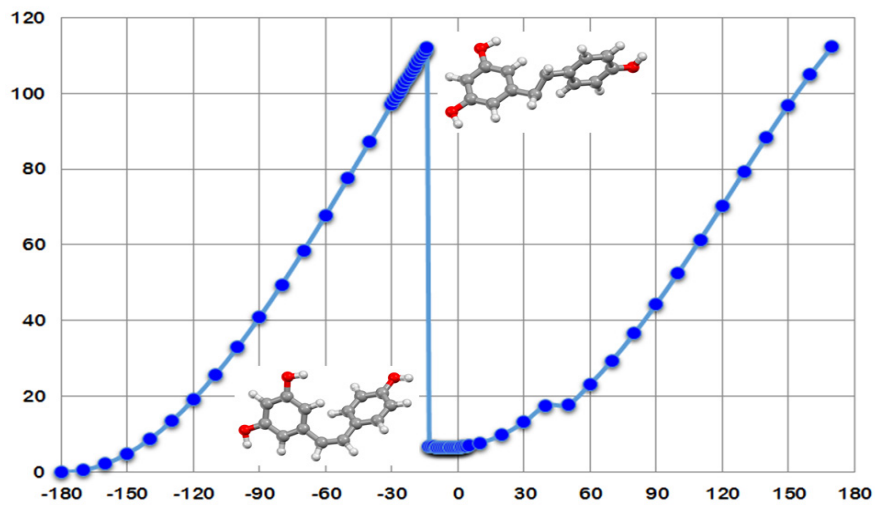


**Fig. 3.** Relaxed 1D PES of *trans*-RESV (c3 conformer) calculated at PCM-B3LYP/STO-3G level of theory, in ethanol

The step was reduced to  $1^\circ$  for the  $-30^\circ \div 0^\circ$  interval, where the transition from *trans* to *cis* occurs. We used the c3 conformer of the RESV because it is the lowest energy conformer in liquid phase for both isomers (see Table 1). Again, two stationary points have been obtained on the 1D PES, the global minimum ( $GM_{1D}$ ) corresponding to the *trans*-RESV and another, local minimum ( $LM_{1D}$ ), for the value of  $-5^\circ$  of the H23-C7-C8-H24 scanning dihedral angle, which corresponds to the *cis* isomer. The maximum energy structure on the 1D PES in ethanol ( $MAX_{1D}$ ) is 106.67 kcal/mol higher in energy than the *trans* isomer and 99.77 kcal/mol than the *cis*-RESV. The angles between the phenyl rings of the *cis* isomer and  $MAX_{1D}$  structures are  $48.64^\circ$  and  $84.07^\circ$ , respectively. Even though the *cis* and *trans* isomers are separated only by 6.9 kcal/mol, the energetic barrier between the two isomers is 106.67 kcal/mol which corresponds to a wavelength of 268 nm. This value is in excellent agreement with the results of Figueiras et al. [7] who used a wavelength of 260 nm for inducing the *trans-cis* photo-isomerization of resveratrol.

As shown in Table 1, our calculations predict a small change of the relative energies of the conformers when going from gas phase to liquid phase. The three studied conformer of both isomers are very close in energy in gas phase, as well as in liquid phase (ethanol, water and DMSO). The conformer c2 of both isomeric forms are the most stable in gas phase, but, contrary to the *trans* isomer, in case of the *cis* isomer, the c3 conformer is very close in energy to c2. On the other hand, in solutions, the c3 conformers are most stable, but c2 conformers also have comparable Boltzmann populations, particularly for the *trans* isomer.

The calculated UV-Vis spectra for the three conformers of *trans* (or *cis*) isomer (not shown) are very similar. Thus, for instance, in case of *trans*-RESV in ethanol, the calculated  $\lambda_{max}$  varies between 342.89 nm for c1 and 343.97 nm for c3, that is, in the limit of experimental errors. For the *cis* conformers,  $\lambda_{max}$  was calculated between 327.55 nm for c2 and 328.25 nm for c3.

**Table 1.** Relative Gibbs energies ( $\Delta G$ , kcal mol<sup>-1</sup>) and Boltzmann populations (%) of the three conformers of *trans*- and *cis*-RESV optimized in gas phase, ethanol, water and DMSO solutions, at room temperature

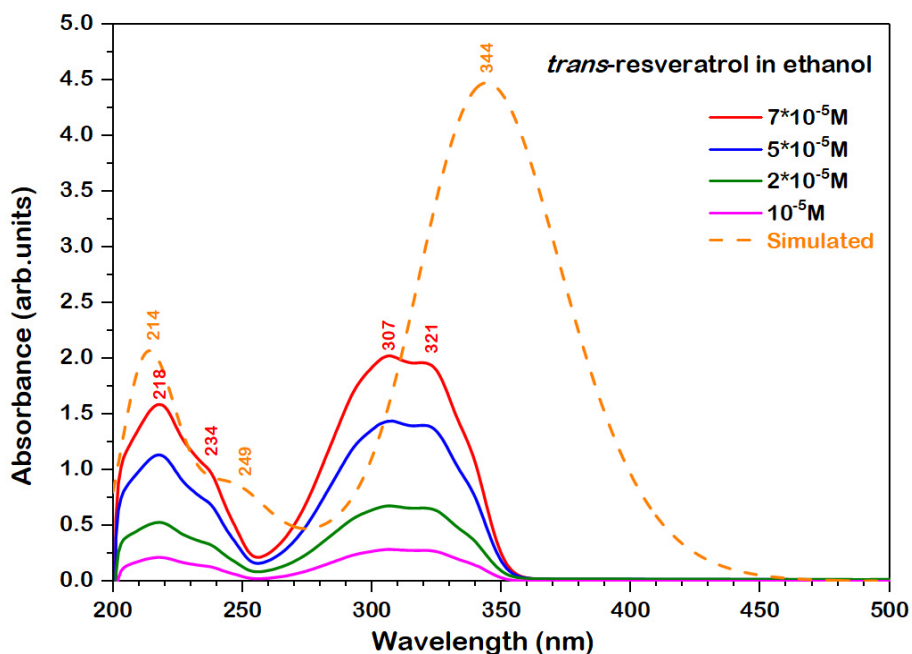
	gas-phase		ethanol		water		DMSO	
	$\Delta G$	Population	$\Delta G$	Population	$\Delta G$	Population	$\Delta G$	Population
<b><i>trans</i>-RESV</b>								
c1	0.648	17.95%	0.239	25.42%	0.285	24.27%	0.270	24.61%
c2	0.000	53.59%	0.024	36.52%	0.043	36.48%	0.036	36.54%
c3	0.375	28.46%	0.000	38.06%	0.000	39.25%	0.000	38.85%
<b><i>cis</i>-RESV</b>								
c1	0.894	10.26%	0.380	21.94%	0.352	22.88%	0.362	22.56%
c2	0.000	46.38%	0.080	36.40%	0.089	35.67%	0.087	35.88%
c3	0.040	43.36%	0.000	41.66%	0.000	41.45%	0.000	41.57%

For this reason we calculated the electronic absorption of both isomeric forms of resveratrol molecules considering the most stable conformation and those with the highest relative populations in ethanol.

The UV-Vis spectra of *trans*-resveratrol in ethanol (Fig. 4) were recorded at four concentrations, ranging from  $7 \cdot 10^{-5}$  M to  $10^{-5}$  M. As can be seen in Figure 4, the UV-Vis spectrum of *trans*-resveratrol consists of four peaks (218, 234, 307 and 321 nm) and their position does not change by varying the concentration.

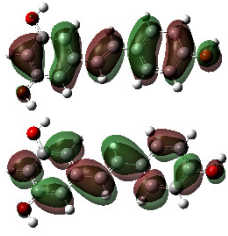
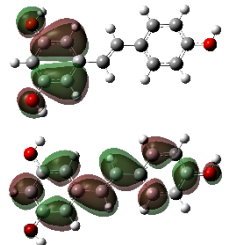
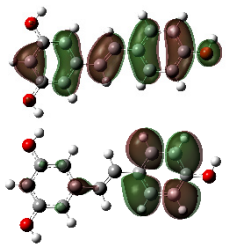
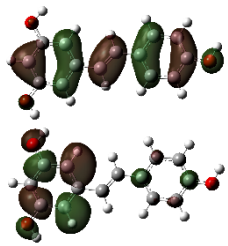
The calculated transition energy values and the transition types of *trans*-resveratrol are summarized in Table 2. The first excited state of the *trans*-resveratrol isomer results from the HOMO  $\rightarrow$  LUMO transition (99%). The calculated value for the electron transition with the smallest energy corresponds to  $\lambda_{\max}=344$  nm, which is higher than the experimentally determined value by cca. 30 nm. Such differences are frequently reported in the literature [18] and they are due to the approximations used in these calculations. On the other hand, the peak at 218 nm is in excellent agreement

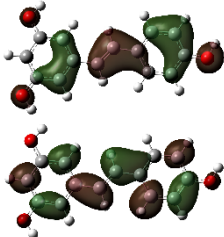
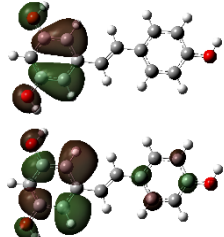
with the experimental value and corresponds to a HOMO-4  $\rightarrow$  LUMO transition. The other experimentally determined peaks are displaced from those theoretically predicted by less than 15 nm. Thus, the experimental bands at 321, 307 and 234 nm correspond to the calculated value of 314 nm, 287 and 232 nm, respectively. The theoretical absorption spectrum of the *trans*-resveratrol molecule (Figure 4, dashed line) reproduces satisfactory all the features of the experimental spectra, both the bands positions and their relative intensities.



**Fig. 4.** Experimental UV-VIS spectrum of the *trans*-resveratrol in ethanol at different concentration and the simulated UV-VIS spectrum of its c3 conformer in ethanol at PCM-TD-B3LYP/6-31+G(2d,2p) level of theory

**Table 2.** PCM-B3LYP/6-31+G(2d,2p) calculated electronic transitions for the c3 conformer of *trans*-resveratrol in ethanol

Excited state	$\lambda$ (nm)	f	Transitions	Contributions * (%)	NTOs** Coefficient/Shape
1	343.97	1.0709	H->L	98.99	0.999 
2	312.36	0.0391	H-1->L	92.90	0.933 
3	286.60	0.0782	H->L+1	82.62	0.840 
6	248.27	0.1278	H->L+3	71.01	0.751 

Excited state	$\lambda$ (nm)	f	Transitions	Contributions * (%)	NTOs** Coefficient/Shape
16	217.40	0.1342	H-4->L	42.45	0.480 
19	210.66	0.3182	H-1->L+3	75.90	0.784 

\*Only the largest contribution is included

\*\*HOTO - left and LUTO – right (isovalue 0.02 a.u.); The NTO coefficients represent the extent to which the excitation can be written as a single configuration [19].

As shown in the last column of Table 2, the first excited state appears as a result of a  $\pi \rightarrow \pi^*$  transition, while the transitions to the excited states 2, 3 and 6 correspond to intra-molecular charge transfers, in each case, the HOTOs and LUTOs being localized on different parts of the molecule. The last two calculated transitions are mainly due to a redistribution of electronic charge within the molecule.

Analogously was studied the *cis*-resveratrol isomer, its absorption spectrum being shown in Figure 5. Four absorption bands can be identified in the experimental spectrum at 204-208 nm, 211 nm, 232 nm and 285-286 nm. Compared to the *trans* isomer, the experimental  $\lambda_{\max}$  for *cis*-RESV is blue-

shifted by 30 nm and less intense than the bands observed in the 204-232 nm. The two isomers show distinct UV-Vis spectra, differing both in the positions of the bands, but also in their relative intensities.

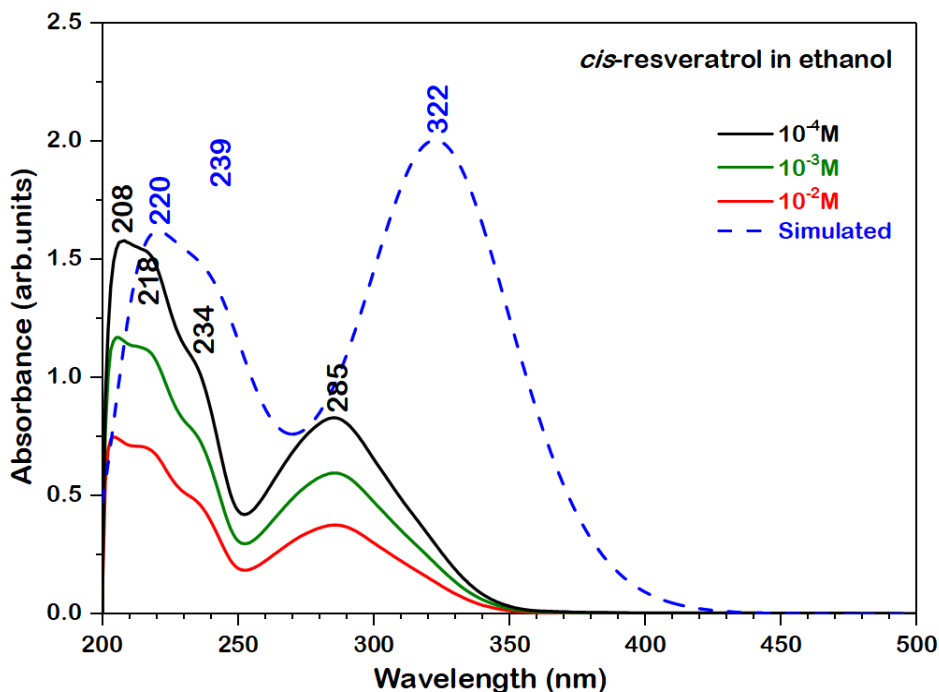


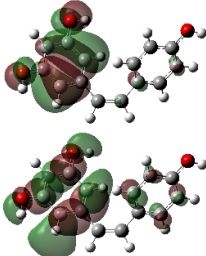
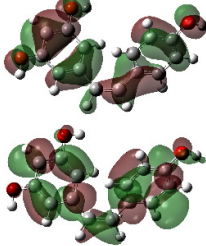
**Fig. 5.** Experimental UV-VIS spectrum of the *cis*-resveratrol in ethanol at different concentration and the simulated UV-Vis spectrum of its c3 conformer in ethanol at PCM-TD-B3LYP/6-31+G(2d,2p) level of theory

The assignments of the electronic transitions of *cis*-RESV are given in Table 3. The lowest excited state for *cis*-RESV appears as a result of HOMO  $\rightarrow$  LUMO transition (97.08% contribution), similar to the case of *trans* isomer. Again, a discrepancy of 37 nm was noted between the experimental and calculated  $\lambda_{\max}$  band.



**Table 3.** PCM-B3LYP/6-31+G(2d,2p) calculated electronic transitions for the c3 conformer of *cis*-resveratrol in ethanol

Excited state	$\lambda$ (nm)	f	Transitions	Contributions* (%)	NTOs** Coefficient/Shape
1	328.25	0.4145	H->L	97.08	0.996 
2	302.25	0.0914	H-1->L	89.48	0.913 
3	279.34	0.1054	H->L+1	80.12	0.819 
6	245.20	0.1196	H->L+4	28.28	0.503 

Excited state	$\lambda$ (nm)	f	Transitions	Contributions* (%)	NTOs** Coefficient/Shape
19	210.96	0.1230	H-1->L+4	39.28	0.489 
25	201.17	0.1910	H-2->L+3	47.16	0.719 

\*Only the largest contribution is included

\*\*HOTO - left and LUTO – right (isovalue 0.02 a.u.). The NTO coefficients represent the extent to which the excitation can be written as a single configuration [19].

The first absorption band experimentally determined at 204-208 nm was not reproduced by calculations. On the other hand, a very good agreement was obtained between the experimental and theoretical excitation energies (especially at 216 nm and 234 nm), the differences being within the limit of the experimental errors. The 216 nm and 234 nm experimental absorption bands are in excellent agreement with those determined theoretically (211 nm and 245 nm, respectively). The first corresponds to the HOMO-1  $\rightarrow$  LUMO+4 transition and the second results from the HOMO  $\rightarrow$  LUMO+4 transition.

Like in the case of *trans* isomer, the lowest excited state of *cis*-RESV is due to the HOMO-LUMO transition of  $\pi$ - $\pi^*$  type. However, as seen in Tables 2 and 3, while the LUMO of the *trans*-RESV is bonding with respect to the C=C double bond, it becomes anti-bonding for the *cis* isomer. This character leads to an increase of its energy for *cis* and, consequently to a higher energy HOMO-LUMO gap and lower  $\lambda_{\max}$ .

The next three transitions with appreciable oscillator strength are due to an intra-molecular charge transfer in the molecule. Also, the last two calculated transitions are again due to a redistribution of electronic charge within the molecule.

## CONCLUSIONS

Here we analyzed the stability of the two isomers of resveratrol, as well as the relative energies of their possible conformers, determined by the relative orientation of the OH groups, in gas-phase as well as in ethanol, water and DMSO solutions at the B3LYP/6-31+G(2d,2p) level of theory.

Three conformers have been identified for each isomer, within a 0 ÷ 0.65 kcal/mol and 0 ÷ 0.29 kcal/mol energy window, in gas-phase and liquid phase, respectively for the *trans* isomer, while for the *cis* partner the corresponding Gibbs free energy intervals were 0 ÷ 0.89 kcal/mol in gas-phase and 0 ÷ 0.38 kcal/mol in solutions. The geometrical parameters of the conformers of each isomer are slightly affected when passing from the gas- to liquid phases.

Conformer 2 is the most stable for both isomeric forms in gas-phase, while the conformer c3 become the most stabilized in water, ethanol and DMSO. However, either in gas-phase or in solutions, the other two conformers are also appreciably populated at room temperature. On the other hand, the conformers of the the *cis* isomer are more than 6 kcal·mol<sup>-1</sup> higher in energy than those of the *trans*- partner.

Two stationary points have been obtained on the 1D PES of RESV in ethanol, corresponding to the *trans* and *cis* isomers, separated by 6.9 kcal/mol. Nevertheless, the energetic barrier between the two isomers is 106.67 kcal/mol, a value which corresponds to a wavelength of 268 nm.

The two isomers show distinct UV-Vis spectra differing in the positions of the  $\lambda_{\max}$ , which is red-shifted for *trans* by 30 nm, but also in its relative intensity with respect to the other absorption peaks. Experimental absorption spectra have been accurately reproduced by TD-DFT calculations and using the NTO it was proved that the lowest excited states are due to  $\pi$ - $\pi^*$  transitions. However, the LUMO orbital changed from bonding to antibonding with respect to the C=C double bond when passing from *trans* to *cis* isomer, causing a lower  $\lambda_{\max}$  for the *cis* isomer.

## ACKNOWLEDGEMENTS

The research undertaken for this article was conducted using the Babeş-Bolyai University Research infrastructure financed by the Romanian Government through the project MADECIP (POSCEE COD SMIS CSNR 48801/1862).

R.A. DOMOKOS highly acknowledges financial support from the Babeş-Bolyai University through a Performance Scholarship during the academic year 2015–2016, contract number 35218/11.11.2015.

## REFERENCES

1. J. Gusman, H. Malonne, and G. Atassi, "A reappraisal of the potential chemopreventive and chemotherapeutic properties of resveratrol," *Carcinogenesis*, 22 (2001) 1111–1117.
2. S. Quideau, D. Deffieux, and L. Pouységu, "Resveratrol Still Has Something To Say about Aging!," *Angew. Chem. Int. Ed.*, vol. 51, no. 28, pp. 6824–6826, Jul. 2012.

3. R.Á. Rodríguez, I.R. Lahoz, O.N. Faza, M.M. Cid, and C.S. Lopez, "Theoretical and experimental exploration of the photochemistry of resveratrol: beyond the simple double bond isomerization," *Org. Biomol. Chem.*, vol. 10, no. 46, pp. 9175–9182, Nov. 2012.
4. M. Diaz, H. Degens, L. Vanhees, C. Austin, and M. Azzawi, "The effects of resveratrol on aging vessels," *Exp. Gerontol.*, vol. 85, no. Supplement C, pp. 41–47, Dec. 2016.
5. J. Park and Y.C. Boo, "Isolation of Resveratrol from *Vitis Viniferae* Caulis and Its Potent Inhibition of Human Tyrosinase," *Evidence-Based Complementary and Alternative Medicine*, 2013. [Online]. Available: <https://www.hindawi.com/journals/ecam/2013/645257/>. [Accessed: 13-Dec-2017].
6. S. Renaud and M. de Lorgeril, "Wine, alcohol, platelets, and the French paradox for coronary heart disease," *Orig. Publ.*, Vol. 1, Issue 8808, vol. 339, no. 8808, pp. 1523–1526, Jun. 1992.
7. T.S. Figueiras, M.T. Neves-Petersen, and S.B. Petersen, "Activation energy of light induced isomerization of resveratrol," *J. Fluoresc.*, vol. 21, no. 5, pp. 1897–1906, Sep. 2011.
8. F. Caruso, J. Tanski, A. Villegas-Estrada, and M. Rossi, "Structural Basis for Antioxidant Activity of trans-Resveratrol: Ab Initio Calculations and Crystal and Molecular Structure," *J. Agric. Food Chem.*, vol. 52, no. 24, pp. 7279–7285, Dec. 2004.
9. Gaussian 09, Revision E.01, M.J. Frisch, G. W. Trucks, H. B. Schlegel, G. E. Scuseria, M. A. Robb, J. R. Cheeseman, G. Scalmani, V. Barone, G.A. Petersson, H. Nakatsuji, X. Li, M. Caricato, A. Marenich, J. Bloino, B.G. Janesko, R. Gomperts, B. Mennucci, H.P. Hratchian, J.V. Ortiz, A.F. Izmaylov, J.L. Sonnenberg, D. Williams-Young, F. Ding, F. Lipparini, F. Egidi, J. Goings, B. Peng, A. Petrone, T. Henderson, D. Ranasinghe, V.G. Zakrzewski, J. Gao, N. Rega, G. Zheng, W. Liang, M. Hada, M. Ehara, K. Toyota, R. Fukuda, J. Hasegawa, M. Ishida, T. Nakajima, Y. Honda, O. Kitao, H. Nakai, T. Vreven, K. Throssell, J.A. Montgomery, Jr., J.E. Peralta, F. Ogliaro, M. Bearpark, J.J. Heyd, E. Brothers, K.N. Kudin, V.N. Staroverov, T. Keith, R. Kobayashi, J. Normand, K. Raghavachari, A. Rendell, J.C. Burant, S.S. Iyengar, J. Tomasi, M. Cossi, J.M. Millam, M. Klene, C. Adamo, R. Cammi, J.W. Ochterski, R.L. Martin, K. Morokuma, O. Farkas, J.B. Foresman, and D. J. Fox, Gaussian, Inc., Wallingford CT, 2016.

10. A.D. Becke, "Density-functional thermochemistry. III. The role of exact exchange," *J. Chem. Phys.*, vol. 98, no. 7, pp. 5648–5652, Apr. 1993.
11. C. Lee, W. Yang, and R.G. Parr, "Development of the Colle-Salvetti correlation-energy formula into a functional of the electron density," *Phys. Rev. B*, vol. 37, no. 2, pp. 785–789, Jan. 1988.
12. S.H. Vosko, L. Wilk, and M. Nusair, "Accurate spin-dependent electron liquid correlation energies for local spin density calculations: a critical analysis," *Can. J. Phys.*, vol. 58, no. 8, pp. 1200–1211, Aug. 1980.
13. W.J. Hehre, R. Ditchfield, and J.A. Pople, "Self-Consistent Molecular Orbital Methods. XII. Further Extensions of Gaussian-Type Basis Sets for Use in Molecular Orbital Studies of Organic Molecules," *J. Chem. Phys.*, vol. 56, no. 5, pp. 2257–2261, Mar. 1972.
14. M.J. Frisch, J.A. Pople, and J. S. Binkley, "Self-consistent molecular orbital methods 25. Supplementary functions for Gaussian basis sets," *J. Chem. Phys.*, vol. 80, no. 7, pp. 3265–3269, Apr. 1984.
15. M.E. Casida, C. Jamorski, K.C. Casida, and D.R. Salahub, "Molecular excitation energies to high-lying bound states from time-dependent density-functional response theory: Characterization and correction of the time-dependent local density approximation ionization threshold," *J. Chem. Phys.*, vol. 108, no. 11, pp. 4439–4449, Mar. 1998.
16. R.L. Martin, "Natural transition orbitals," *J. Chem. Phys.*, vol. 118, no. 11, pp. 4775–4777, Feb. 2003.
17. J. Tomasi, B. Mennucci, and R. Cammi, "Quantum Mechanical Continuum Solvation Models," *Chem. Rev.*, vol. 105, no. 8, pp. 2999–3094, Aug. 2005.
18. A.J. Cohen, P. Mori-Sánchez, and W. Yang, "Challenges for Density Functional Theory," *Chem. Rev.*, vol. 112, no. 1, pp. 289–320, Jan. 2012.
19. A.E. Clark, "Time-Dependent Density Functional Theory Studies of the Photoswitching of the Two-Photon Absorption Spectra in Stilbene, Metacyclopentadiene, and Diarylethene Chromophores," *J. Phys. Chem. A*, vol. 110, no. 10, pp. 3790–3796, Mar. 2006.



## XRD INVESTIGATION OF THERMAL DEGRADATION EFFECT ON SOME COMMERCIAL PET SAMPLES

M. TODICA<sup>1\*</sup>, Z. KOVACS-KRAUSS<sup>1</sup> and CARMEN NICULAESCU<sup>1</sup>

**ABSTRACT.** The structural changes of some commercial PET samples, submitted to different thermal treatments, were investigated by XRD method. Rapid cooling of melted samples, leads to partial destruction of the initial local ordered structure. A tendency of polymeric chain to conglomerate into new small crystalline structures is observed. At slow cooling this tendency is accentuated, but the initial ordered structure is almost entirely destroyed.

**Keywords:** PET, thermal degradation, XRD method

### INTRODUCTION

Solid polyethylene terephthalate, (PET), in its solid form, is one of the most popular polymers used for various packaging, often for food products and alimentary liquids as water or soft drinks. It is cheap, easy to produce, and as a container, acceptably maintains the quality of the aliments or liquid within over long periods of time.

---

<sup>1</sup> "Babes-Bolyai" University, Faculty of Physics, M. Kogalniceanu No 1, 400084 Cluj-Napoca, Romania

\* Corresponding author: mihai.todica@phys.ubbcluj.ro



Due to the continuous accumulation of PET wastes, with small rate of recycling, this polymer is one of the most pollutant material produced by the humanity, for what reason the investigation of its potential reuse or recycling is being conducted constantly. At the most basic level, PET bottles are often recycled by grinding and milling into lower grade packing material, or fibers. Dissolving these materials with specific solvents and then repolymerization is possible, but the procedure is not frequently used because it is expensive and takes more effort than simply creating more new material. One of the simplest method of destroying or recycling these materials is the thermal degradation, but this process could produces other secondary pollutant products, or can induces irreversible modification of the structure the polymer, avoiding its use for new applications, [1,2]. It is a reason for which the study of the thermal effects on the molecular structure of these materials is important. XRD is a suitable technique for investigation such local ordering modification and can offer information concerning the reuse of these materials, [3].

## **EXPERIMENTAL**

We used for ours investigation small square pieces, with the dimensions 20x20 mm and the thickness about 0.3 mm, taken off from commercial PET water bottles. The samples were heated progressively on aluminum plate, up to 300°C, until an even melt was obtained. Once the samples were completely melted, there were maintained at this temperature 1-2 minutes for homogenization. We did not leave samples on for much longer, to prevent decomposition of PET chains. After that the samples were cooled. The crystallization of PET is greatly affected by cooling rate, and we wished to investigate this effect as well. To facilitate this, we employed two simple cooling methods. The first was to take off the plate with the melt from the heating system and leave it in open air, at room temperature, to cool progressively by passively convection. This process takes approximately 3 minutes. For further discussions we refer this as the slow cooling process.

The second cooling procedure, referred as fast cooling, was achieved by immersing rapidly the melted sample in cold water. This cooling process is estimated to take about 2-5 seconds. Using this procedure, all samples remain transparent and flexible, mostly in amorphous phase, without crystallization.

The X-ray diffraction was performed with Bruker X-ray diffractometer, with  $\text{Cu K}\alpha$   $\lambda=1.54 \text{ \AA}$ , at 45 KV and 40 mA. The  $2\theta$  range of  $10\text{--}40^\circ$  was recorded, within  $0.1^\circ$  resolution.

## RESULTS AND DISCUSSION

Generally the polymers are known as amorphous materials due to the disordered arrangement of the chains, [4, 5]. However, some times, parts of different neighboring chains, or different parts of the same chain, can adopt a parallel local arrangement, giving a local ordered character to the sample. This situation is called crystalline phase.

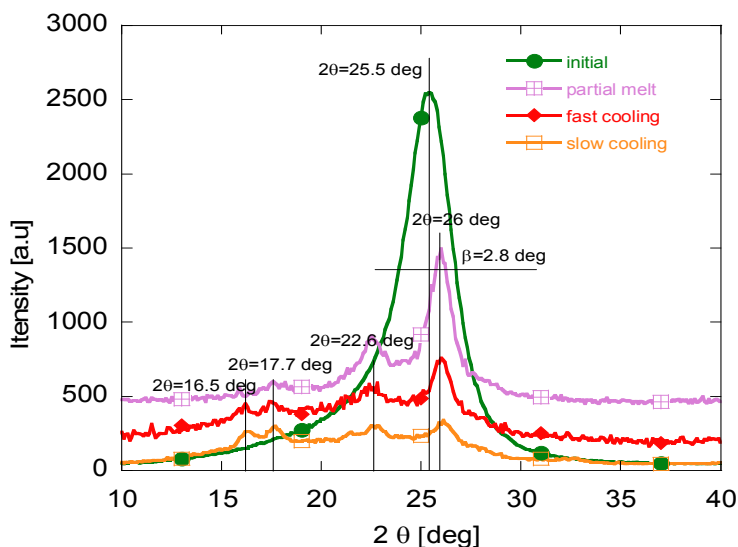


**Fig. 1.** The XRD data recorded for PET in initial state, partially melted, melted and fast cooled, melted and slow cooled.

The crystallization is determined by the particularities of polymerization process or by the action of different external factors, as the heating-cooling process. In function of the amount of crystalline phase, we speak about crystalline, semi-crystalline or amorphous polymers. The distance between the parallel portions of the polymeric chains, in the crystalline phase, is of the same order of magnitude as the inter-planar distance of solid crystals, and behaves in the same manner as a solid crystal, when they are investigated by XRD method. It is the reason for which XRD can be successfully used for structural polymeric investigation. From the diffraction theory we can calculate the inter-planar distance with the Bragg equation:

$$d = \frac{k \cdot \lambda}{2 \sin \theta} \quad (1)$$

where  $k$  is the diffraction order and  $2\theta$  is the diffraction angle. The area  $S$  under the diffraction peak is proportional with the concentration of the ordered domains in the sample, [6-9].

In native state, the PET is a semi-crystalline polymer, containing both the amorphous and crystalline phase, [10]. This affirmation is confirmed by the XRD pattern of the PET sample before any heating process. The spectrum contains a high peak centered at the diffraction angle  $2\theta = 25.5^\circ$ , with a great area. That corresponds to a large fraction of the polymeric chains, in parallel arrangement, with the inter-planar distance  $d=3.48\text{\AA}$ . However the peak is not narrow, (like in the case of the solid crystals), it is large, with the half line width  $\beta = 2.8^\circ$ , between  $2\theta = 23.9^\circ$  and  $26.7^\circ$ , (Fig. 1). That shows a dispersion of the inter-planar distances between  $d_1=3.33\text{\AA}$  and  $d_2=3.74\text{\AA}$ . That shows that the sample contains many ordered domains with parallel arrangement of the chains, with inter-planar distances ranging between  $d_1$  and  $d_2$ . Outside these crystalline domains, the polymeric chains are in the amorphous phase. A simplified sketch of such structure is presented in figure 2. The amorphous phase leads to the broadening of the spectrum.

The crystallinity of a PET is greatly dependent on the thermal treatment, especially the heating-cooling rate, [2, 11]. The heating process increases the dynamics of the polymeric chains, which have the tendency to disengage from the ordered arrangement and become freely.

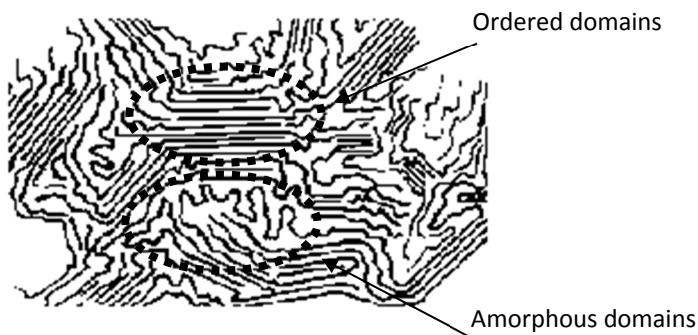


**Fig. 2.** Schematic representation of the semicrystalline polymer.

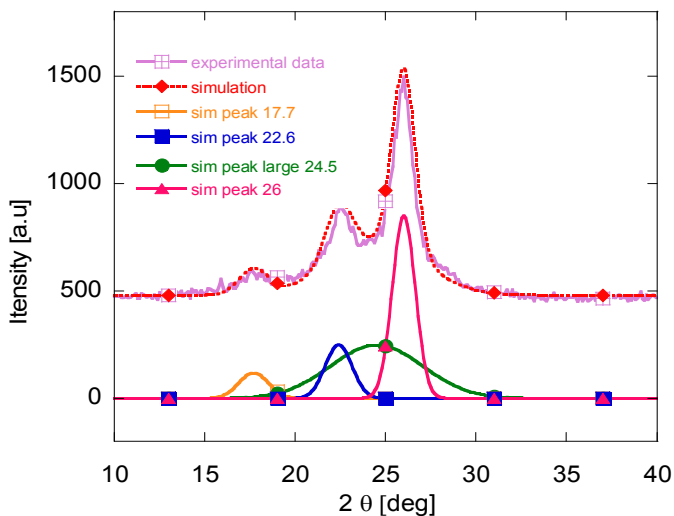


**Fig. 3.** Simulation of the experimental XRD data for PET partially melted.

As result, the fraction occupied by the crystalline phase into the whole sample decreases. Moreover it is possible that new nucleation centers appear in the sample, giving rise to new ordered domains, generally with different inter-planar distances and different sizes. Consequently the XRD spectrum changes. We can see this effect for partially melted samples, (Fig. 1). The XRD spectrum of these samples contains three peaks, at  $2\theta = 26^\circ$ ,  $22.6^\circ$  and  $17.7^\circ$ . The first peak at  $26^\circ$  is the correspondent one of the high peak at  $2\theta = 25.5^\circ$  of the unheated PET, but its amplitude is reduced and it shifts towards higher angles. That means that the initial ordered phase of the polymer, responsible for the peak  $2\theta = 25.5^\circ$ , occupies smaller fraction into the partially melted samples, and becomes more compact, with smaller inter-planar distance,  $d=3.42 \text{ \AA}$ . The new peaks at  $2\theta = 22.6^\circ$  and  $17.7^\circ$  indicate the apparition of new crystalline domains, with greater inter-planar distance. Theirs small amplitude shows only small fraction occupied into the sample. The fractions occupied by each ordered structure are proportional with area of the peak. To calculate these parameters we simulated the spectrum using Gaussian function for each peak.

$$f(\theta) = A \exp \left[ -\frac{(\theta - \theta_0)^2}{\beta} \right] \quad (2)$$

There  $\theta_0$  is the diffraction angle of the maximum of the peak and  $\beta$  is the half line width. The result of simulation, for the partially melted sample, is shown in figure 3. The parameters of the simulation are listed in Table 1. In this table S denotes the area under each peak,  $S_{\text{tot}}=3635 \text{ a.u.}$  is the area of the entire spectrum,  $d$  is the inter-planar distance corresponding to the maximum of the peaks and  $S/S_{\text{tot}}$  represents the fraction of the crystalline phase corresponding to each peak into the entire sample. The simulation shows also the existence of a broad peak, centered at  $2\theta = 24.5^\circ$ , superimposed over the main three peaks. This peak corresponds to the completely disordered phase which appears into the polymer after the melting.

In the un-melted sample this peak is difficult to be seen because it is hidden by the high peak at  $2\theta = 25.5^\circ$ . However it exists and enlarges the whole spectrum.

**Table 1.**

$2\theta_0$ [deg]	$\beta$ [deg]	S [a.u.]	S/S <sub>tot</sub> [%]	d [Å]
17.7	1.3	240	6.61	5.01
22.6	1.1	464	12.76	3.96
26	0.8	1347	37.06	3.42
24.5	1.3	1584	43.57	3.62

As the sample become to melt, the initial crystalline phase diminishes in the detriment of the amorphous phase, but additionally new small crystalline domains, designed by the peak at  $2\theta = 22.6^\circ$  and  $17.7^\circ$ , appear. When the samples are completely melted and then cooled, the situation is different. The degree of crystallinity is noticeable in the sample depending on whether it's opaque or transparent [2]. At fast cooling rate we can see a drastic decrease of the intensities of the peaks at  $2\theta = 22.6^\circ$  and  $26^\circ$ , small increase of the peak at  $2\theta = 17.7^\circ$ , and the apparition of a new peak at  $2\theta = 16.5^\circ$  (Fig. 1). That means massive destruction of the initial crystalline phase and the apparition of new centers of crystallization with higher inter-planar distance. At slow cooling rate, the decrease of the intensities of the peaks at  $2\theta = 22.6^\circ$  and  $26^\circ$  is more pronounced than in the case of fast cooling, but the peaks at  $2\theta = 17.7^\circ$  and  $16.5^\circ$  appears more clearly into the spectrum. That means intensification of the degradation of the initial crystalline phase and accentuation of the tendency of the polymeric chains to form new small ordered domains. To explain this behavior we must take into account the fact that the crystallization process takes time to spread from nucleation centers towards the amorphous places. At fast cooling rate the polymeric

chains have not enough time to disengage completely from the ordered domains that result in the persistence of an important proportion of ordered phase. However a great fraction of the chains have enough time to escapes from the ordered phase and become free. The result is the growing of the amorphous phase. A small fraction of them have enough time to conglomerate into new small ordered domains, responsible for the new peaks at  $2\theta = 17.7^\circ$  and  $16.5^\circ$ . At slow cooling rate, the polymeric chains have enough time to disengage from the ordered domains, determining almost complete destruction of the initial ordered phase. The intensity of the peak  $2\theta = 22.6^\circ$  and  $26^\circ$  decreases considerable. On the other hand, the chains have more time to self assembling in the new ordered domains, that explains the refinement of the shape of the peaks at  $2\theta = 17.7^\circ$  and  $16.5^\circ$ .

## CONCLUSION

The thermal degradation of commercial PET was investigated by XRD method. The initial samples, before any heating process, have a semi-crystalline structure dominated by the crystalline phase. The XRD spectrum shows an intense peak at  $2\theta = 25.5^\circ$ . The structure of the samples changes in function of the thermal treatment. In the partially melted samples the fraction of the amorphous phase increases in the detriment of the ordered phase. Moreover the inter-planar distance of the crystalline phase decreases and new crystallization centers becomes to appear. At fast cooling rate the fraction of the initial crystalline phase decreases again and the tendency of crystallization in new domains is accentuated. At slow cooling rate, the initial ordered phase is almost completely destroyed, the amorphous phase is dominant, and the tendency of crystallization in new centers appear more clearly. As final conclusion we can affirm that changes of local structure of the PET depend strongly on the particularities of heating-cooling process.

## REFERENCES

1. D.C. Bassett, Principles of Polymer Morphology, Cambridge (UK), Cambridge University Press, 1981.
2. X.F. Lu, J.N. Hay, Isothermal crystallization kinetics and melting behavior of poly(ethylene terephthalate), *Polymer* 42(23):9423-9431, 2001.
3. Barbara Stuart, Polymer Analysis. Chichester (UK): John Wiley & Sons; 2002.
4. J.P. Cohen Addad, Physical properties of polymeric gels: Chichester (UK): John Wiley & Sons; 1996.
5. M. Todica, Proprietăți fizice ale polimerilor, Cluj-Napoca, Presa Universitara Clujeană, 2005, ISBN 973-610-376-5.
6. M. Todica, V. Simon, T. Stefan, D.L. Trandafir, I. Balasz, Spectroscopic investigation of gamma irradiated PAA-graphite membranes, *Indian Journal of Pure and Applied Physics*. 53. 2015. p. 359-366.
7. M. Todica, T. Stefan, S. Simion, I. Balasz, L. Daraban, UV-Vis and XRD investigation of graphite-doped poly(acrylic) acid membranes, *Turkish Journal of Physics*, 2014.
8. C. Lung, D. Marconi, M. Toma and A. Pop, Characterization of the Aluminum Concentration upon the Properties of Aluminum Zinc Oxide Thin Films, *Analytical Letters* 49, No. 8, 1278–1288, 2016.
9. C. Lung, M. Toma M. Pop, D. Marconi, A. Pop, Characterization of the structural and optical properties of ZnO thin films doped with Ga, Al and (Al plus Ga), *Journal of Alloys and Compounds*, 725, 25, 1238-1243, 2017.
10. B. Demirel, A.H. Yaras, B.F. Elcicek, Crystallization behavior of PET materials, *Bil Enst Dergisi Cilt*; 13:26–35, 2011.
11. S.A. Jabarin, Crystallization kinetics of Polyethylene Terephthalate. II. Dynamic Crystallization of PET. *Journal of Applied Polymer Science* vol. 34, 2003.





# PHOTOPHYSICAL PROPERTIES OF PERYLENE MOLECULE

LARISA MILENA ȚIMBOLMAȘ<sup>1</sup>, V. CHIȘ<sup>1\*</sup>

**ABSTRACT.** In this work we investigated computationally the photophysics of the perylene molecule using the time-dependent Density Functional Theory (TD-DFT). Particularly, we were interested in the vertical emission energy and radiative fluorescence lifetime of the investigated molecule. Using adequate models and proper computational methodologies we were able to satisfactorily predict the experimentally reported photophysical properties of the perylene core.

**Keywords:** *perylene; photophysics; excited state; TD-DFT; radiative lifetime*

## 1. INTRODUCTION

Perylene derivatives, consisting of a perylene core functionalized with different substituents, attached at their terminal and/or bay-positions [1], have been used for many years as technical pigments due to their high temperature, photo and chemical stabilities [2]. Besides, in the last years, such compounds

---

<sup>1</sup> Babeș-Bolyai University, Faculty of Physics, 1 Kogălniceanu, RO-400084 Cluj-Napoca, Romania

\* Corresponding author: [vasile.chis@phys.ubbcluj.ro](mailto:vasile.chis@phys.ubbcluj.ro)

gained a great popularity because of their use in optical devices [3-5]. These  $\pi$  conjugated dyes show high photosensitivity and high electron mobility (the charge-carrier mobilities are between  $1 \text{ cm}^2\text{v}^{-1}\text{s}^{-1}$  and  $10 \text{ cm}^2\text{v}^{-1}\text{s}^{-1}$ ) [3]. Also, their photophysical properties, particularly the sensitivity of their fluorescence lifetime to the pH, render them very useful as probes for live cell fluorescence lifetime imaging [6].

The photophysical properties of such derivatives are expected to be similar to those of the perylene core. However, in spite of numerous works reported on the absorption and emission properties of perylene derivatives, surprisingly few studies deal with its photophysical properties [3, 7-13].

Besides being a distinct parameter of the molecular excited states, independent of concentration, the fluorescence lifetimes are fundamental parameters for the fluorescence lifetime imaging microscopy (FLIM). They show unique properties which render them very useful for getting information related to the changes of the molecular environment, micro-viscosity, pH, identification of the components in a mixture, or for inter-molecular interactions [14]. Therefore, the accurate determinations of these parameters by experimental or computational techniques are highly needed [15].

While the fluorescence lifetime can be measured nowadays with great accuracy by using the Time-Correlated Single Photon Counting (TCSPC) technique [16], however, its estimation by quantum chemical calculations imposes challenges due to the fact that it requires the optimization of the excited state geometries and the calculation of the dipole moment strength corresponding to the energetic minimum of the excited state. This is why a reduced numbers of studies were reported till now, having as subject the quantum chemical calculation of this parameter [17, 18].

In this study we were interested to obtain computationally the excitation and emission energies and the radiative fluorescence lifetime of the perylene molecule. An interesting and useful characteristic of the molecule is represented by its upconverting properties in sensitized systems [11]. In addition, due to its relatively small size and high symmetry ( $D_{2h}$ ), the perylene

core is an excellent model for testing different calculation methodologies adapted to various molecular properties. Of particular importance are the absorption and emission energies, as well as the radiative lifetime.

Using the model of vertical transition, the radiative emission rate can be written as [19]:

$$k_r = \frac{1}{\tau_r} = \frac{4}{3} \frac{\Delta E^3}{c^3} \mu_{10}^2 \quad (1)$$

where  $c$  is the speed of light,  $\Delta E$  is the energy of transition  $S_1 \rightarrow S_0$  and  $\mu_{10}^2$  is the transition dipole strength.  $\Delta E$  and  $\mu_{10}$  must be evaluated for the energy minimum corresponding to the excited state of the molecule, including solvent effects [17]. The fluorescence lifetime is very sensitive to the conformation of the molecule and to the environment, so any change in the surroundings of the molecule leads to important changes of this parameter [40].

The fluorescence lifetime, defined as the time after which the fluorescence signal intensity (the number of molecules remaining in the excited state) decreases to  $1/e$  of its initial value, can be written using the radiative and non-radiative rates as:

$$\tau_f = 1 / (k_r + k_{nr}) \quad (2)$$

The rate of radiative de-excitation corresponds to the radiative lifetime  $k_r$ , and the non-radiative de-excitation rate corresponds to the non-radiative lifetime:

$$\tau_r = 1 / k_r \text{ and } \tau_{nr} = 1 / k_{nr} \quad (3)$$

The fluorescence total lifetime  $\tau_f$  can be written in terms of  $\tau_r$  și  $\tau_{nr}$  as:

$$\tau_f = \frac{\tau_r \tau_{nr}}{\tau_r + \tau_{nr}} \quad (4)$$

The fluorescence emission efficiency (quantum yield) of a fluorophore is defined as the ratio of the number of photons emitted and the number of photons absorbed by the sample or, in other words, the fraction of molecules

returning from the excited state S1 to the ground state S0 by radiative emission [20]. This parameter can be estimated based on the two radiative and non-radiative rate constants [21]:

$$\Phi_f = \frac{k_r}{k_r + k_{nr}} = \frac{\tau_f}{\tau_r} \quad (5)$$

Alternatively,  $\tau_f$  can be obtained from the recorded absorption and emission spectra of the fluorophore, based on the Strickler-Berg equation [7]:

$$\frac{1}{\tau_f} = 2.88 \cdot 10^9 n^2 \langle \tilde{\nu}_0^{-3} \rangle^{-1} \frac{g_f}{g_e} \int \epsilon(\nu) d \ln(\nu) \quad (6)$$

where integration is done over the entire fluorophore absorption band. Here,  $n$  is the refractive index of the solvent,  $\tilde{\nu}_0$  is the wave number corresponding to the absorption maximum,  $\epsilon$  is the molar extinction coefficient and  $g_f$  and  $g_e$  are the degenerations of the fundamental and excited state, respectively.

## 2. COMPUTATIONAL DETAILS

The DFT and TD-DFT calculations were performed using the Gaussian 09 Rev. E.01 [22]. For both, DFT and TD-DFT methodology we used the B3LYP [23-26], M06-2X [27] and APFD [28] exchange correlation functionals with Pople style basis sets [29, 30]. The geometries of fundamental and excited states were optimized, and the type of minima obtained was confirmed by the frequencies calculation on each optimized geometry, performed at the same level of theory as that used for geometry optimization. Absorption and emission spectra were calculated using the TD-DFT [31] methodology implemented in the Gaussian 09 program. Figures representing the structures of Perylene have been created using the Mercury 3.9 program [32]. Solvent effects have been accounted for by using the Polarizable Continuum Model (PCM) [33] and the Universal Solvation Model Based on Solute Electron Density (SMD) [34].

### 3. RESULTS AND DISCUSSIONS

Experimental absorption and emission spectra of perylene in cyclohexane were constructed based on data from ref. [35] and they are presented in Fig. 1. As observed, the absorption spectrum [35] is dominated by the vibronic structure of the first  $\pi$ - $\pi^*$   $S_0 \rightarrow S_1$  electronic transition with the 0-0 peak at 436 nm. The energy difference between the first two peaks in the absorption spectrum corresponds to a vibration with  $1574 \text{ cm}^{-1}$  wavenumber. A normal mode at  $1567 \text{ cm}^{-1}$  wavenumber was calculated for  $S_1$  state of perylene in cyclohexane at SMD-B3LYP/6-311++G(2d,p) level of theory, and it corresponds to the C=C stretching vibration along the longitudinal axis of the molecule. This is similar to the case of perylene bis-imide reported previously by our group [36].

As shown in Table 1, the available experimental photophysical data for perylene are quite dispersed, particularly in terms of its fluorescence lifetime. The molecule was studied experimentally in the gaseous phase [9] but also in dilute cyclohexane [10], toluene [3,11], acetone [12] or methanol [13] solutions. The reported 0-0 transition wavelengths are 437.5 nm in cyclohexane [10] and 438.6 nm in toluene. Dalavi et al. [12] reported  $\lambda_{\text{max}} = 434 \text{ nm}$  in acetone and Torres et al. [3] reported for perylene in toluene at room temperature  $\lambda_{\text{max}}$  for absorption at 440 nm and  $\lambda_{\text{max}}$  for emission at 444 nm. Thus, a minor influence of the solvent on the absorption and emission energies was observed. Contrary, large differences were noted for the measured lifetimes by different groups.

Thus, the reported experimental values of the fluorescence lifetime ( $\tau_f$ ) of perylene are: 6.40 ns in cyclohexane [10], 4.21 ns in toluene [3], 3.78 ns in toluene [11] and 3.63 ns in methanol [13].

Based on the Strickler-Berg equation [7] and using the absorption and emission spectra taken from ref. [38] we obtained a value of 4.66 ns in cyclohexane.

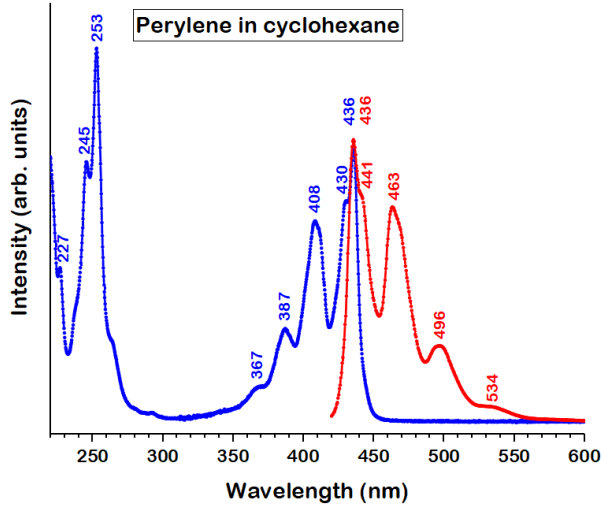


**Fig. 1.** Absorption and fluorescence spectra of perylene in cyclohexane (adapted from ref. [35]).

**Table 1.** Available experimental photophysical parameters of perylene

Reference	[9]	[7]	[37]	[10]	[35, 38]	[11]	[3]	[13]	[12]
Solvent	Gas-phase	Cyclo-hexane	Cyclo-hexane	Cyclo-hexane	Cyclo-hexane	Toluene	Toluene	Ethanol	Acetone
$\lambda_{max}^{abs}(nm)$	415.4	n.a.	436	437.5	436	438.6	440	n.a.	434
$\lambda_{max}^{ems}(nm)$	n.a.	n.a.	n.a.	n.a.	436	n.a.	444	n.a.	n.a.
$\tau_r(ns)$	3.88-4.16	4.79	4.70	6.40	4.66***	3.78	3.80	3.63	n.a.
$\Phi$	0.97	0.89	n.a.	0.93	0.94	0.89	0.95	n.a.	n.a.
$\tau_r(ns)^*$	4.00-4.29	5.38	n.a.	6.88	4.96	4.26	4.00	n.a.	n.a.
$\tau_{nr}(ns)^{**}$	129.33-137.28	43.68	n.a.	91.73	77.04	34.36	76.00	n.a.	n.a.

\* calculated based on eq. (5)

\*\* calculated based on eq. (4)

\*\*\* calculated based on eq. (6)

na – not available

We mention that the theoretical data presented in this study correspond to the perylene in cyclohexane and the position of the absorption and emission bands were obtained without considering the vibronic structure of the two spectra.

Computational data provided by using three functionals APFD, B3LYP and M06-2X are presented in Table 2. Excitation and emission energies (in nm) correspond to the vertical transitions. The calculated transitions dipole strength calculated on the minimum structure of the excited state of perylene were also included in Table 2.

To compute the vertical emission energy, which is the difference between the excited state energy calculated on the optimized geometry and the ground state energy calculated on the excited state geometry, it is necessary to optimize both the ground and excited state of the investigated molecule. The estimation of the 0-0 transitions also requires a frequency calculation for the excited state.

**Table 2.** Calculated photophysical parameters of perylene in cyclohexane

Functional	Basis set	Solvation model	$\lambda_{max}^{ex\ vert}$ (nm)	$\lambda_{max}^{ems\ vert}$ (nm)	Dipole strength (a.u.)	$\tau_r$ (ns)
APFD	6-311+G(2d,p)	SMD	453.8	523.0	8.0710	8.75
B3LYP	6-31+G(2d,2p)	PCM	462.3	528.3	7.7158	9.43
B3LYP	6-31+G(d,p)	CPCM	462.5	526.2	8.2569	8.71
M06-2X	6-31+G(d,p)	CPCM	402.4	480.0	8.7928	6.21
M06-2X	6-31+G(d,p)	PCM*	401.0	458.0	8.4905	5.59
M06-2X	6-311G(d,p)	CPCM	393.9	472.4	8.6656	6.01
M06-2X	6-31G(d)	CPCM	385.7	458.0	8.6445	5.48

ex – excitation; vert – vertical; ems – emission; \* - state specific solvation

As observed in Table 2, the B3LYP functional provides higher absorption  $\lambda_{max}$  than the experimental values, this behavior of the B3LYP functional being well-known in the literature [39]. However, for the emission energies, the discrepancy between experiment and theory is much worse, with an unacceptable



difference of cca. 90 nm. Obviously, this behavior affects drastically the calculated radiative fluorescence lifetime which is significantly higher than the experimental one.

APFD functional, even though coupled to a very flexible triple-zeta basis set, brings some improvement on the calculated excitation energy but still provides unsatisfactory results for the emission energy and the radiative lifetime.

Contrary to B3LYP and APFD, the M06 xc functional systematically provides higher excitation and emission energies compared to B3LYP and APFD. While  $\lambda^{\text{ex}}$  are more than 35 nm larger than the experimental value, the vertical emission wavelengths are in qualitative agreement with the experimental counterpart. As seen in Table 2, in case of M06-2X/6-31G(d) and state-specific solvation-M06-2X/6-31+G(d,p) levels of theory, the agreement with experiment is quantitative. This situation is reflected in the calculated radiative lifetimes, which are significantly lower, and closer to the experimental value.

One should remark also the effect of the diffuse functions mixed in the basis set; it seems that such functions decrease the vertical emission energy and decrease the radiative lifetime.

Fig.4 shows the calculated bond lengths for perylene in its ground and excited state. Because of the high symmetry of

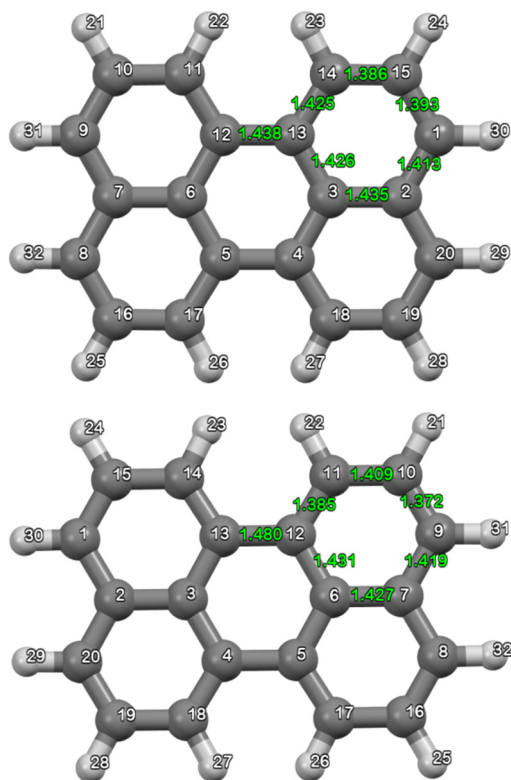


**Fig. 4.** Bond lengths for the ground state (bottom) and excited state (top) of the perylene molecule in cyclohexane, calculated at M06-2X/6-31+G(d,p) level of theory.

the molecule, only the non-redundant bond lengths are displayed. First of all, it is observed that the molecule retains its planarity when passing from the ground state to the excited state. It is also noticed that the molecule contracts the C12-C13, C4-C5 and C14-C15 bond lengths as a result of electronic excitation. A contrary variation is seen in the case of bonds that are not parallel to the long axis of the molecule. The lengths of CH bonds as well as the valence angles do not change appreciably as a result of transition between the two states.

Similar geometric distortions have been noted for the perylene bis-imide derivative [36].

#### 4. CONCLUSIONS

The purpose of this study was to describe the parameters of excited states for the perylene molecule.

It was shown that the APFD and B3LYP functionals provide vertical excitation energies in agreement with the experiment, but much too higher vertical emission energies. Conversely, the M06-2X functional performs bad for reproducing the excitation energies but it provides much better values for the vertical emission energies.

Inclusion of the diffuse functions into the basis set leads to a drastic decrease of the emission energy and consequently an increase of the calculated radiative fluorescence lifetime for perylene.

For obtaining reliable DFT calculated radiative lifetimes for perylene (and perylene derivatives) we recommend the use of M06-2X functional, coupled to the 6-31+G(d,p) basis set. It is also concluded that state-specific solvation of the excited state is mandatory for reaching quantitative agreement between the calculated and experimental photophysical parameters.

## ACKNOWLEDGMENTS

The research undertaken for this article was conducted using the Babeș-Bolyai University Research infrastructure financed by the Romanian Government through the project MADECIP (POSCEE COD SMIS CSNR 48801/1862).

## REFERENCES

1. J.Y. Kim, S.W. Woo, J.W. Namgoong, J.P. Kim, A study on the fluorescence property of the perylene derivatives with methoxy groups, *Dyes Pigm.*, 148 (2018), 196-205.
2. L.B.-A. Johansson, H. Langhals, Spectroscopic studies of fluorescent perylene dyes, *Spectrochim. Acta A*, 47 (1991), 857-861.
3. E. Torres, M.N. Berberan-Santos, M.J. Brites, Synthesis, photophysical and electrochemical properties of perylene dyes, *Dyes Pigm.*, 112 (2015), 298-304.
4. J. Makowiecki, E. Piosik, G. Neunert, R. Stolarski, W. Piecek, T. Martynski, Molecular organization of perylene derivatives in Langmuir-Blodgett multilayers, *Opt. Mater.*, 46 (2015), 555-560.
5. B. Pagoaga, O. Mongin, M. Caselli, D. Vanossi, F. Momicchioli, M. Blanchard-Desce, G. Lemercier, N. Hoffmann, Optical and photophysical properties of anisole- and cyanobenzene-substituted perylene diimides, *Phys. Chem. Chem. Phys.*, 18 (2016), 4924-4941.
6. D. Aigner, R.I. Dmitriev, S.M. Borisov, D.B. Papkovsky, I. Klimanta, pH-sensitive perylene bisimide probes for live cell fluorescence lifetime imaging, *J. Mater. Chem. B*, 2 (2014), 6792-6801.
7. S.J. Strickler, R.A. Berg, Relationship between Absorption Intensity and Fluorescence Lifetime of Molecules, *J. Chem. Phys.*, 37 (1962), 814-822.
8. W.R. Ware, P.T. Cunningham, Fluorescence lifetime and Fluorescence Enhancement of Perylene Vapor, *J. Chem. Phys.*, 44 (1966), 4364-4365.

9. M. Sonnenschein, A. Amirav, J. Jortner, Absolute fluorescence quantum yields of large molecules in supersonic expansions, *J. Phys. Chem.*, 88 (1984), 4214-4218.
10. N.I. Nijegorodov, W.S. Downey, The Influence of Planarity and Rigidity on the Absorption and Fluorescence Parameters and Intersystem Crossing Rate Constant in Aromatic Molecules, *J. Phys. Chem.*, 98 (1994), 5639-5643.
11. M.R. Ribas, R.P. Steer, R. R  ther, Photophysical properties of new bis-perylene dyads for potential upconversion use, *Chem. Phys. Lett.*, 605-606 (2014), 126-130.
12. D.K. Dalavi, D.P. Bhopate, A.S. Bagawan, A.H. Gore, N.K. Desai, A.A. Kamble, P.G. Mahajan, G.B. Kolekar, S.R. Patil, Fluorescence quenching studies of CTAB stabilized perylene nanoparticles for the determination of Cr(VI) from environmental samples: spectroscopic approach, *Anal. Methods*, 6 (2014), 6948-6955.
13. S. Acikgoz, Investigation of time-resolved fluorescence lifetime of perylene dye molecules embedded in silicon nanopillars, *Appl. Phys. A*, 118 (2015), 629-636.
14. B. Valeur, *Molecular Fluorescence Principles and Applications*, Wiley-VCH, Weinheim, 2002.
15. E. Fiserova, M. Kubala, Mean fluorescence lifetime and its error, *J. Lumin.*, 132 (2012), 2059-2064.
16. M. Wahl, Time-Correlated Single Photon Counting, Technical Note TCSPC v.2.1, PicoQuant GmbH, 2009.
17. M. Savarese, A. Aliberti, D. De Santo, E. Battista, F. Causa, P.A. Netti, N. Rega, Fluorescence Lifetimes and Quantum Yields of Rhodamine Derivatives: New Insights from Theory and Experiment, *J. Phys. Chem. A*, 116 (2012), 7491-7497.
18. Y. Zhang, L.L. Zhang, R.S. Wang, X.M. Pan, Theoretical study on the electronic structure and optical properties of carbazole- $\pi$ -dimesitylborane as bipolar fluorophores for nondoped blue OLEDs, *J. Mol. Graphics Modell.*, 34 (2012), 46-56.
19. B. Lounis, M. Onil, Single-photon sources, *Rep. Prog. Phys.*, 68 (2005), 1129-1179.
20. J.R. Lakowicz, *Principles of Fluorescence Spectroscopy*, Kluwer Academic/Plenum Publishers, New York, 1999.
21. M. Sauer, J. Hofkens, and J. Enderlein, Basic Principles of Fluorescence Spectroscopy, in *Handbook of Fluorescence Spectroscopy and Imaging*, Wiley-VCH, 2011.

22. Gaussian 09, Revision E.01, M.J. Frisch, G.W. Trucks, H.B. Schlegel, G.E. Scuseria, M.A. Robb, J.R. Cheeseman, G. Scalmani, V. Barone, B. Mennucci, G.A. Petersson, H. Nakatsuji, M. Caricato, X. Li, H.P. Hratchian, A.F. Izmaylov, J. Bloino, G. Zheng, J.L. Sonnenberg, M. Hada, M. Ehara, K. Toyota, R. Fukuda, J. Hasegawa, M. Ishida, T. Nakajima, Y. Honda, O. Kitao, H. Nakai, T. Vreven, J.A. Montgomery, Jr., J.E. Peralta, F. Ogliaro, M. Bearpark, J.J. Heyd, E. Brothers, K.N. Kudin, V.N. Staroverov, R. Kobayashi, J. Normand, K. Raghavachari, A. Rendell, J.C. Burant, S.S. Iyengar, J. Tomasi, M. Cossi, N. Rega, J.M. Millam, M. Klene, J.E. Knox, J.B. Cross, V. Bakken, C. Adamo, J. Jaramillo, R. Gomperts, R.E. Stratmann, O. Yazyev, A.J. Austin, R. Cammi, C. Pomelli, J.W. Ochterski, R.L. Martin, K. Morokuma, V.G. Zakrzewski, G.A. Voth, P. Salvador, J.J. Dannenberg, S. Dapprich, A.D. Daniels, Ö. Farkas, J.B. Foresman, J.V. Ortiz, J. Cioslowski, and D.J. Fox, Gaussian, Inc., Wallingford CT, 2009.
23. A.D. Becke, Density-functional thermochemistry. III. The role of exact exchange, *J. Chem. Phys.*, 98 (1993), 5648-5652.
24. C. Lee, W. Yang, R.G. Parr, Development of the Colle-Salvetti correlation-energy formula into a functional of the electron density, *Phys. Rev. B*, 37 (1988), 785.
25. S. H. Vosko, L. Wilk, M. Nusair, Accurate spin-dependent electron liquid correlation energies for local spin density calculations: a critical analysis, *Can. J. Phys.*, 1980, 58, 1200.
26. P.J. Stephens, F.J. Devlin, C.F. Chabalowski, M.J. Frisch, Ab Initio Calculation of Vibrational Absorption and Circular Dichroism Spectra Using Density Functional Force Fields: A Comparison of Local, Nonlocal, and Hybrid Density Functionals, *J. Phys. Chem.*, 98 (1994), 11623-11627.
27. Y. Zhao, D.G. Truhlar, The M06 suite of density functionals for main group thermochemistry, thermochemical kinetics, noncovalent interactions, excited states, and transition elements: two new functionals and systematic testing of four M06-class functionals and 12 other functionals, *Theor. Chem. Acc.*, 120 (2008), 215-241.
28. A. Austin, G. Petersson, M.J. Frisch, F.J. Dobek, G. Scalmani, and K. Throssell, A density functional with spherical atom dispersion terms, *J. Chem. Theory Comput.*, 8 (2012), 4989-5007.

29. W.J. Hehre, R. Ditchfield, J.A. Pople, Self Consistent Molecular Orbital Methods. XII. Further Extensions of Gaussian Type Basis Sets for Use in Molecular Orbital Studies of Organic Molecules, *J. Chem. Phys.*, 56 (1972), 2257-2261.
30. M.J. Frisch, J.A. Pople, J.S. Binkley, Self-consistent molecular orbital methods 25. Supplementary functions for Gaussian basis sets, *J. Chem. Phys.*, 80 (1984), 3265-3269.
31. M.R. Casida, C. Jamorski, K.C. Casida, D.R. Salahub, Molecular excitation energies to high-lying bound states from time-dependent density-functional response theory: Characterization and correction of the time-dependent local density approximation ionization threshold, *J. Chem Phys.*, 108 (1988), 4439-4449.
32. C.F. Macrae, P.R. Edgington, P. McCabe, E. Pidcock, G.P. Shields, R. Taylor, M. Rowler, J. Van de Streek, Mercury: visualization and analysis of crystal structures, *J. Appl. Crystallogr.*, 39 (2006), 453-457.
33. J. Tomasi, B. Mennucci, R. Cammi, "Quantum Mechanical Continuum Solvation Models," *Chem. Rev.*, 105 (2005), 2999–3094.
34. A.V. Marenich, C.J. Cramer, D.G. Truhlar, Universal Solvation Model Based on Solute Electron Density and on a Continuum Model of the Solvent Defined by the Bulk Dielectric Constant and Atomic Surface Tensions, *J. Phys. Chem. B*, 113 (2009), 6378–6396.
35. <http://www.fluorophores.tugraz.at/> (accessed: December 5-th, 2017).
36. M. Oltean, A. Calborean, G. Mile, M. Vidrighin, M. Iosin, L. Leopold, D. Maniu, N. Leopold, V. Chiş, Absorption spectra of PTCDI: A combined UV–Vis and TD-DFT study, *Spectrochim. Acta A*, 97 (2012), 703-710.
37. I.B. Berlman, Handbook of Fluorescence Spectra of Aromatic Molecules, Academic Press, 1965.
38. J.M. Dixon, M. Taniguchi, J.S. Lindsey, PhotochemCAD 2: a refined program with accompanying spectral databases for photochemical calculations, *Photochem. Photobiol.*, 81 (2005), 212-213.
39. J.B. Foresman, A. Frisch, Exploring Chemistry with Electronic Structure Methods, 3rd edition, Gaussian, Inc.: Wallingford, CT, 2015.
40. M.Y. Berezin, S. Achilefu, Fluorescence lifetime measurements and biological imaging, *Chem. Rev.*, 110 (2010), 2641-2684.



## MAGNETIC PROPERTIES OF THE PEROVSKITE OXIDE $\text{PbV}_{1-x}\text{Fe}_x\text{O}_3$ INVESTIGATED BY ELECTRON PARAMAGNETIC RESONANCE SPECTROSCOPY

A. OKOS<sup>1</sup>, OANA RAITA<sup>2</sup>, A. POP<sup>1\*</sup>

**ABSTRACT.** The perovskite oxide  $\text{Pb}(\text{V}_{1-x}\text{Fe}_x)\text{O}_3$  ( $0 \leq x \leq 0.75$ ) was synthesised by solid state reaction under high pressure (HP) – high temperature (HT) conditions. The effect of partial substitution of V with Fe on magnetic properties of  $\text{PbVO}_3$  compound were studied by Electron Paramagnetic Resonance (EPR) spectroscopy measurements.

**Keywords:** *PbVO<sub>3</sub>, high pressure - high temperature synthesis, EPR spectroscopy*

### INTRODUCTION

The properties of  $\text{ABO}_3$  perovskite oxides can often be improved by introducing magnetic dopants as long as their ferroelectric properties can be maintained.

Bulk  $\text{PbVO}_3$  is known to be a  $\text{PbTiO}_3$ -type structure with a large tetragonal distortion ( $c/a = 1.22$ ), with the V atoms displaced from symmetric O–V–O bonding along the c-axis, [1, 2].

---

<sup>1</sup> Faculty of Physics, Babes-Bolyai University, Str. M Kogălniceanu, Nr. 1, RO-400084 Cluj-Napoca, Romania.

<sup>2</sup> INCDTIM, Str. Donath Nr. 65-103, RO-400293 Cluj-Napoca, Romania.

\* Corresponding author: aurel.pop@phys.ubbcluj.ro



Both theoretical and experimental studies have shown that V ions in bulk  $\text{PbVO}_3$  are arranged in two-dimensional antiferromagnetic (AFM) ordering [3-5]. However, a long magnetic order is difficult to realize in  $\text{PbVO}_3$  samples as it is often coupled to a spin glass phase.[1,6].

The single d electron per  $\text{V}^{IV}$  is localized and ordered into the xy orbital in the basal plane; the in-plane interatomic V–O–V interactions between the localized- electron spins give a broad maximum in the paramagnetic susceptibility near 200 K ,typical of 2D antiferromagnetic interactions [2,7].

If the weak magnetism is caused by the 2D arrangement of the V cations, the substitution could reduce the tendency of the system to form a 2D network and could lead to the onset of a 3D magnetic ordering.

The Fe ion with a large magnetic moment could provide some remnant magnetic moments at the oxygen ions and degrade the magnetic moment of the V ions by Fe–O –V super-exchange interaction [8].

The  $\text{PbV}_{1/2}\text{Fe}_{1/2}\text{O}_3$  sample was previously synthesized at the pressure  $p = 7$  GPa and temperature  $T = 800\text{-}1000^\circ\text{C}$ , [9].The tetragonal distortion, which is still large in  $\text{PbV}_{1/2}\text{Fe}_{1/2}\text{O}_3$  (the  $c/a = 1.18$ , placed between the values of 1.23 for  $\text{PbVO}_3$  and 1.06 for  $\text{PbTiO}_3$ ) is considered to be a second order Jahn-Teller effect caused by the electronic configuration of the  $\text{V}^{5+}$  ion and the lone electron pair of the  $\text{Pb}^{2+}$  ion.

In the present work, we will attempt to shed some light on the problem of the effect of partial substitution of V with Fe in of  $\text{PbVO}_3$  compound on magnetic properties by Electron Paramagnetic Resonance (EPR) spectroscopy measurements.

## EXPERIMENTAL

$\text{PbV}_{1-x}\text{Fe}_x\text{O}_3$  ( $0 \leq x \leq 0.75$ ) polycrystalline samples were prepared by solid state reaction under high pressure, high temperature conditions (HP-HT) in a CONAC type apparatus.

For our samples almost single phase samples were obtained at pressures of 6 GPa and temperatures of 950° C, [10,11]. EDX measurements evidenced that the chemical composition of the samples with  $x < 0.5$  were little different from those expected from starting elements.

For samples with  $x < 0.5$  Fe the main phase correspond to the tetragonal structure in the space group P4mm. The  $a = b$  lattice constants do not depend on the composition and the unit cell height  $c$  decreased linearly with increasing iron content. [10]

X-Ray Absorption Spectroscopy (XAS) data for the vanadium K edge reveals in our samples the presence of  $\text{V}^{4+}$  and  $\text{V}^{5+}$ , and below  $x=0.5$  Fe the composition of the samples can be written as  $\text{Pb}(\text{V}^{4+}_{1-2x}\text{V}^{5+}_x\text{Fe}^{3+}_x)\text{O}_3$  [11]. For  $x = 0.5$  all the  $\text{V}^{4+}$  cations are exhausted and consequently the sample contains only  $\text{V}^{5+}$  and  $\text{Fe}^{3+}$  cations (result consistent with the need / choice of starting oxides). This can also explain why the solid solution stops at  $x = 0.5$ .

Electron Paramagnetic Resonance (EPR) measurements were carried out on a Bruker Elexsys E500 spectrometer in X band (at 9.4 GHz) and in function of temperature.

## RESULTS AND DISCUSSION

EPR was used as an effective tool to study the local magnetic interactions of Vanadium ions. EPR spectra of our  $\text{PbVO}_3$  powder sample show a well-resolved hyperfine structure typical for  $\text{V}^{4+}$  ions, as in fig.11 and reference [11]. The EPR spectra of V(IV) ions in an isotropic environment exhibit eight lines of equal peak-to-peak width due to the hyperfine coupling of one unpaired electron ( $S = 1/2$ ) with the nuclear spin ( $I = 7/2$ ) of  $^{51}\text{V}$ . The spectrum shows that both parallel and perpendicular features can be seen.

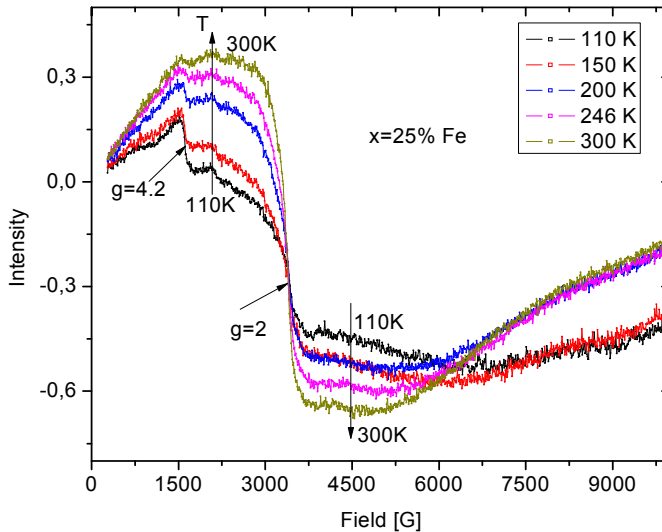
The EPR parameters for  $\text{V}^{4+}$  ions obtained from experimental spectra are consistent with a square–pyramidal  $\text{C}_{4v}$  coordination specific for vanadyl ions [11-16]. The hyperfine coupling constants  $A_{||}$  and  $A_{\perp}$  are sensitive to the local bonding environment for  $\text{V}^{4+}$  coordinated with oxygen ligands.

The small decrease of the hyperfine coupling  $A_{||}$  and  $A_{\perp}$  suggest the slight increase of ligand field with increasing temperature from 110K to 300K [11].

Three signals are invariably reported for  $\text{Fe}^{3+}$  [17-19]: a sharp line around  $g=4.3$ , interpreted as  $\text{Fe}^{3+}$  in a tetrahedral environment with strong rhombic distortion, a broad line around  $g=2.3$  due to oxidic Fe species and a line around  $g=2$ , interpreted as  $\text{Fe}^{3+}$  in (distorted) octahedral environment

The widths of the line are larger in low magnetic fields when compared to high magnetic fields. If the lowest doublet,  $|S_{\pm 1/2}\rangle$  is populated, it gives a  $g$  value of 2 to 6 whereas if the middle Kramer's doublet  $|S_{\pm 3/2}\rangle$  is populated, a  $g$  value 4.30 is expected.

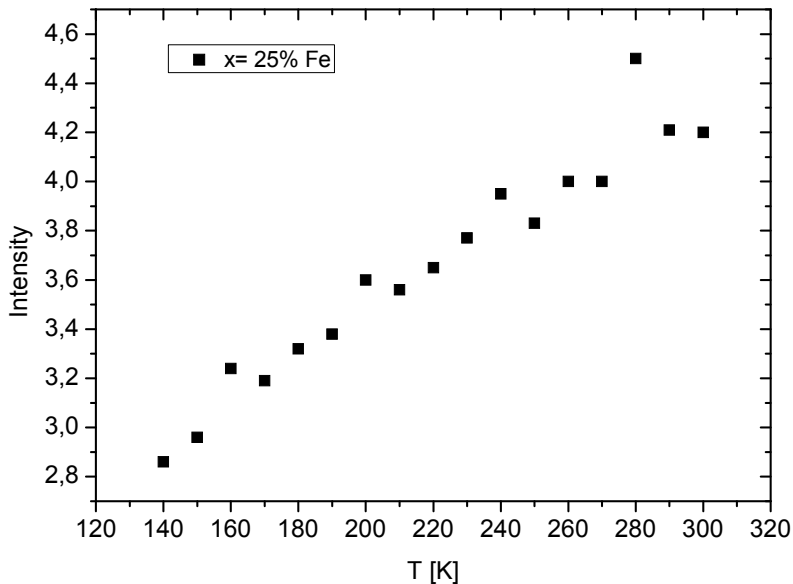
The Fe substitution samples investigated by EPR spectroscopy are  $x=25\% \text{Fe}$  and  $x=40\% \text{Fe}$ . Figure 1 shows the spectra for  $x=0.25$  sample at 5 temperatures (from 300K to 110K). It can be observed that all the resonance spectra exhibit a broad line, centred on  $g = 2$  due to the spin of the  $\text{Fe}^{3+}$  ions. An additional resonant mode is situated around  $g = 4.2$ . By decreasing the temperature the signal around  $g = 4.2$  is well resolved and the signal intensity decreases.



**Fig. 1.** EPR spectra for  $x=25\%$  Fe sample.

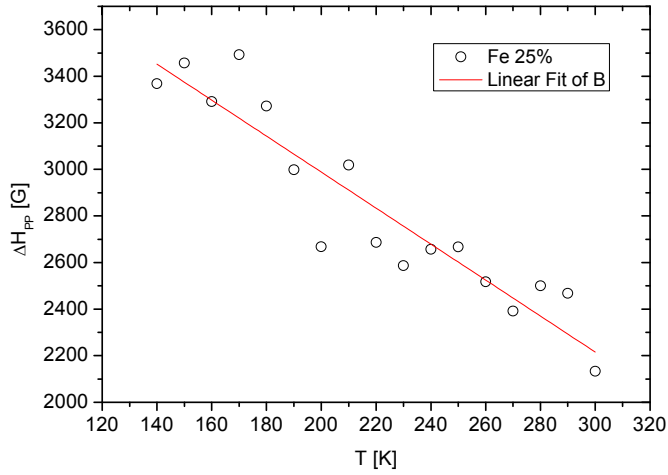
The presence of the additional resonant mode is interpreted as an indication of the presence of  $\text{Fe}^{3+}$  cations in a tetrahedral environment with a strong rhombic distortion.

The complete evolution of the EPR line intensity/concentration of the paramagnetic  $\text{Fe}^{3+}$  centres with the temperature, as determined in the present investigation, is presented in figure 2. One finds that the EPR line intensity of the  $\text{Fe}^{3+}$  paramagnetic centre decreases with decreasing temperature. This suggest the increase of the number of antiferromagnetic  $\text{Fe}^{3+}$ - $\text{Fe}^{3+}$  pairs by decreasing temperature.



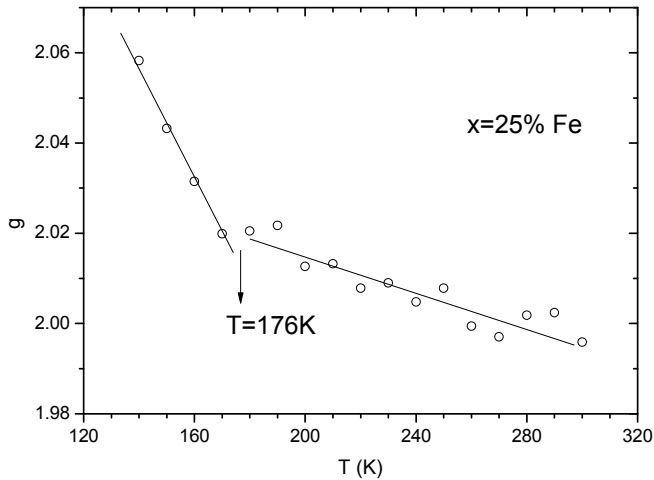
**Fig. 2.** Temperature dependence of the EPR integrated intensity of the  $x=25\%$  Fe sample.

Figure 3 shows that the linewidth  $\Delta H_{pp}$  increases by decreasing temperature. The large value of  $\Delta H_{pp}$  is the result of a strong magnetic dipolar interaction between the  $\text{Fe}^{3+}$  ions [20].



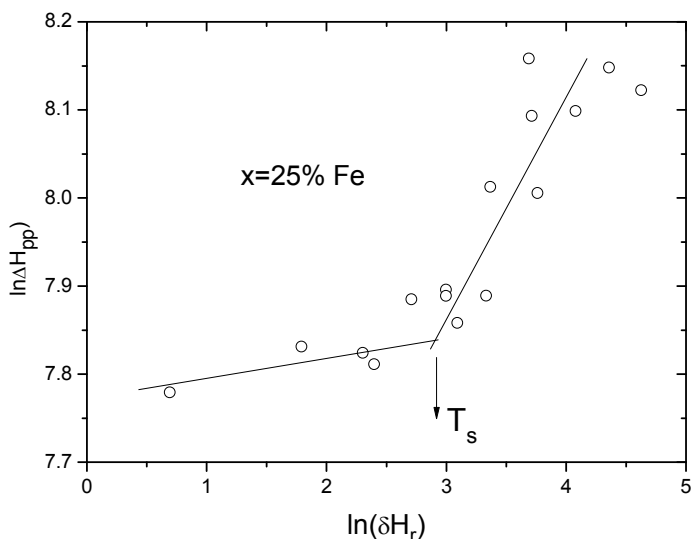
**Fig. 3.** Temperature dependence of the line width in function of temperature for  $x=25\%Fe$  sample.

Figure 4 shows that the  $g$ -factor increases linearly with decreasing temperature, presenting a change of the slope around  $\sim 176$  K. The approximate temperature rate of change for the  $g$ -factor is  $\Delta g/\Delta T \sim 0.17 \cdot 10^{-3} \text{ K}^{-1}$  in the temperature range of 300 to 180 K and  $\Delta g/\Delta T \sim 1.26 \cdot 10^{-3} \text{ K}^{-1}$  (170 –138 K).



**Fig. 4.** Temperature dependence of the  $g$ -factor for  $x=0.25$  sample.

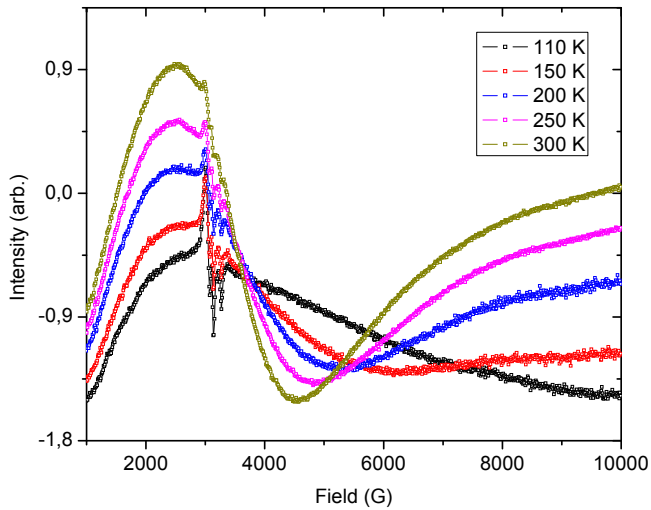
The double logarithmic plot of linewidth  $\Delta H_{pp}$  versus a shift of resonance field  $\Delta H_r$  (see Fig. 5) reveals the existence of two relaxation types with negative slope in the high temperature ranges (300 - 180 K), (175 - 130 K), with a crossover temperature  $T_s$  around 175 K.



**Fig. 5.** Plot of  $\ln(\Delta H_{pp})$  vs.  $\ln(\delta H_r)$  for the  $x=25\%$  Fe sample. The crossover temperature is indicated by the arrow.

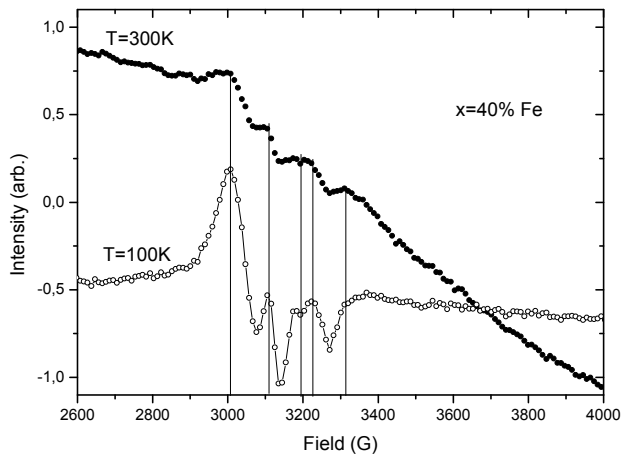
Figure 6 shows the spectra for the  $x=40\%$  Fe sample at the same 5 temperatures as for  $x=25\%$  Fe sample. The signal seems to contain two components: a large transition attributed to  $\text{Fe}^{3+}$  ions (assigned to the central fine structure  $\Delta M_S = -1/2 \rightarrow 1/2$  transition) and a hyperfine structure, respectively.

The EPR line intensity of a paramagnetic centre is proportional with its concentration. For the  $x=40\%$  Fe sample the decrease of the EPR signal with the decreasing temperature shows that the concentration of free  $\text{Fe}^{3+}$  ions decreases. This behaviour is related with the antiferromagnetic order evidenced from magnetic susceptibility measurements.



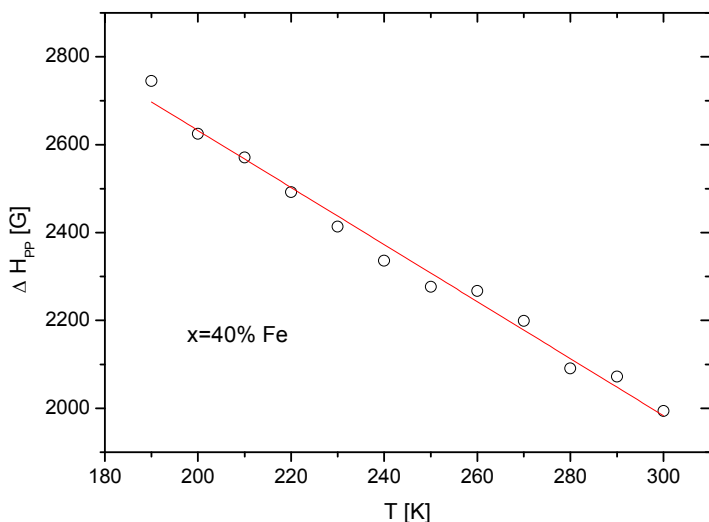
**Fig. 6.** EPR spectra for the  $x=40\%$  Fe sample at different temperatures.

Figure 7 shows that by decreasing the temperature, the hyperfine structure becomes well resolved.



**Fig. 7.** The hyperfine structure of  $x=40\%$  Fe sample at temperatures  $T=300\text{K}$  and  $T=100\text{K}$ , respectively.

Figure 8 shows that the linewidth  $\Delta H_{pp}$  increases by decreasing temperature with a slope of  $\Delta H_{pp}/\Delta T = -6.5 \text{ G/K}$ , a value lower comparatively with the one obtained for the  $x=25\%$  Fe sample ( $\Delta H_{pp}/\Delta T = -7.7 \text{ G/K}$ ). The large value of  $\Delta H_{pp}$  confirms the presence of a strong magnetic dipolar interaction between the  $\text{Fe}^{3+}$  ions.



**Fig. 8.** Temperature dependence of the line width function of temperature for  $x=40\%$ Fe sample.

Figure 9 shows that the  $g$ -factor decreases with decreasing temperature, with a noticeable change observed about  $\sim 260 \text{ K}$  and  $200 \text{ K}$ . The temperature change for the  $g$ -factor is  $\Delta g/\Delta T = 1.95 \cdot 10^{-3}$ . The shift of  $g$ -factor and the decrease of  $\Delta H_{pp}$  suggest the increase of the exchange interaction in the sample with  $x=40\%$  Fe comparatively with the  $x=25\%$  Fe sample.

The double logarithmic plot of linewidth  $\Delta H_{pp}$  versus a shift of resonance field  $\Delta H_r$  (see Fig. 10) shows the existence of a single relaxation type with positive slope in the high temperature range (300-200 K).



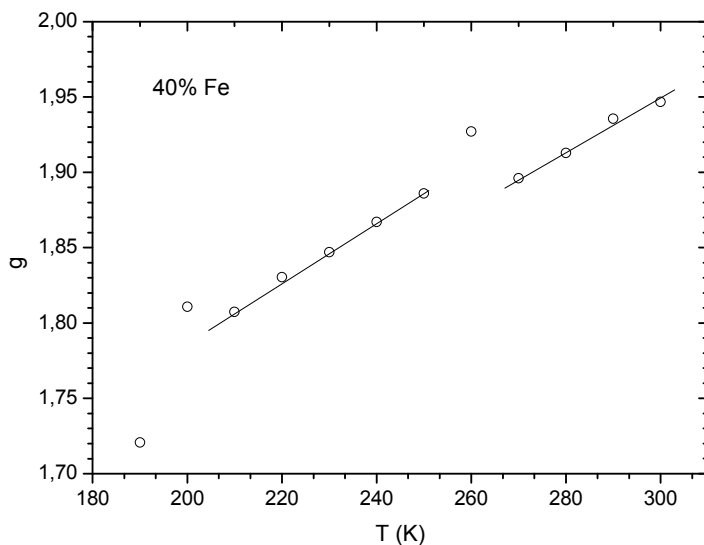


**Fig. 9.** Temperature dependence of the g – factor for sample x=40% Fe.

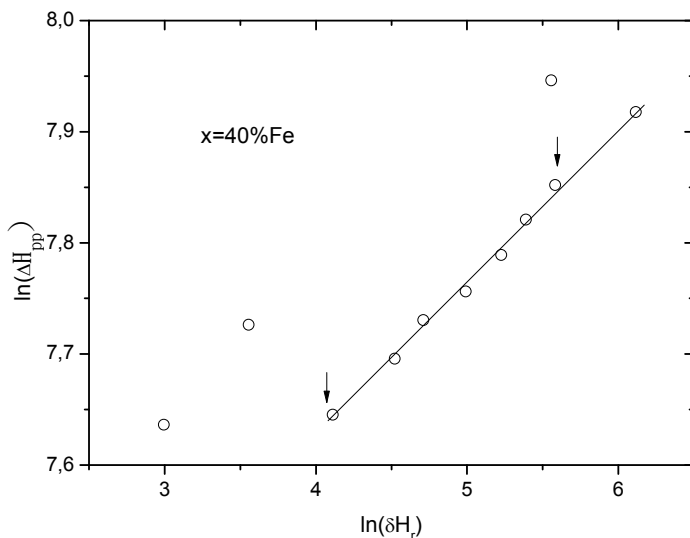


**Fig. 10.** Plot of  $\ln(\Delta H_{pp})$  vs.  $\ln(\delta H_r)$  for sample x=40% Fe.

Figure 11 shows comparatively the fine structure of the  $\text{PbVO}_3$  ( $x=0.00$  Fe) and of  $x=40\%$  Fe samples. The shift to lower fields of fine structure for  $x=40\%$  Fe sample (PVF\_40) suggest the existence of a different internal field because of the Fe ions. Most likely, the fine structure can be attributed to the vanadium ions.

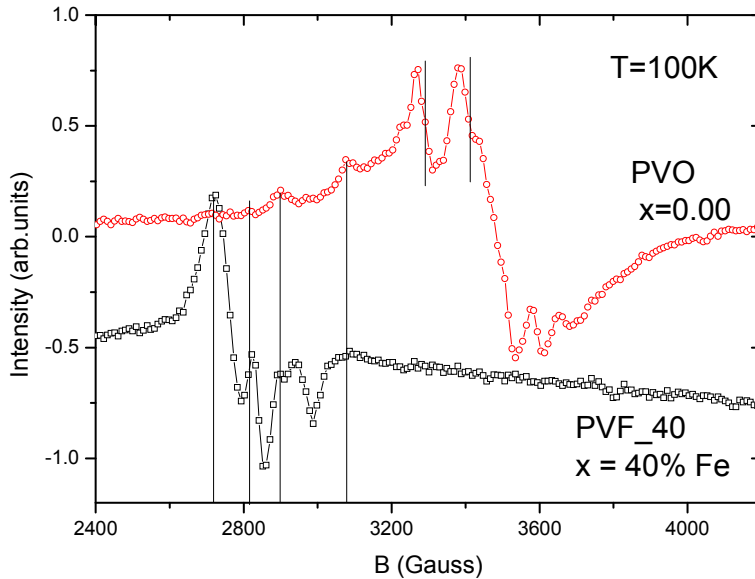


**Fig. 11.** Hyperfine structure of sample  $\text{PbVO}_3$  ( $x=0.0$  Fe) and of the  $x=40\%$ Fe sample.

## CONCLUSIONS

EPR results function of temperature for  $\text{PbVO}_3$  are consistent with the presence of  $\text{V}^{4+}$  paramagnetic ions in a square-pyramidal  $C_{4v}$  coordination (with hyperfine coupling constants  $A_{||}$  and  $A_{\perp}$ ), [11]. The evolution of the hyperfine coupling constants function of temperature is in agreement with the small increase of unit cell height  $c$  with increase of the temperature [10].

All resonance spectra function of temperature, for samples  $x=25\%$  and  $40\%$  exhibit a broad line, centred on  $g=2$  due to the spin of the  $Fe^{3+}$  ions.

For the  $x = 25\%$ Fe sample, an additional resonant new absorption mode situated around  $g=4.2$  was evidenced. It is attributed of the presence of  $Fe^{3+}$  ions on a tetrahedral environment with a strong rhombic distortion.

For sample with  $x=40\%$  Fe, the superimposed hyperfine structure around  $g=2$  can be attributed to the vanadium ions.

The large value of  $\Delta H_{pp}$  is the result of strong magnetic dipolar interaction between the  $Fe^{3+}$  ions in both the  $x=25\%$  and  $40\%$  Fe samples.

The shift of  $g$ -factor and the decrease of  $\Delta H_{pp}$  suggest the increase of the exchange interaction in sample by increasing  $x$ .

The decrease of EPR line intensity attributed to  $Fe^{3+}$  paramagnetic centre with decreasing temperature, suggest the increase of the number of antiferromagnetic pairs  $Fe^{3+}$ - $Fe^{3+}$ .

For the sample  $x=25\%$  Fe two relaxation mechanisms were evidenced with a crossover temperature  $T_s$  around  $175K$ , while for the  $x=40\%$  Fe sample only a single relaxation type is present.

## REFERENCES

1. Shpanchenko R.V., Chernaya V.V., Tsirlin A.A., Chizhov P.S., Sklovsky D.E. and Antipov E.V., 2004, *Chem. Mater.*, 16, 3267-3273.
2. Oka K., Yamada I., Azuma M., Takeshita S., Satoh K.H., Koda A., Kadono R., Takano M. and Shimakawa Y., 2008, *Inorg. Chem.*, 47, 7355.
3. Singh D.J., 2006, *Phys. Rev. B*, 73, 094102.
4. Tsirlin A.A., Belik A.A., Shpanchenko R.V., Antipov E.V., Takayama- Muromachi E. and Rosner H., 2008, *Phys. Rev. B*, 77, 092402.
5. Uratani Y., Shishidou T. and Oguchi T., 2009, *J. Phys. Soc. Jpn.*, 78, 084709.

6. Kumar A., Martin L.W., Denev S., Kortright J.B., Suzuki Y., Ramesh R. and Gopalan V., 2007, *Phys. Rev. B*, 75, 060101.
7. Bonner J.C. and Fisher M.E., 1964, *Phys. Rev.*, 135, A640.
8. Tsuchiya T., Katsumata T., Ohba T. and Inaguma Y., 2009, *J. Ceram. Soc. Jpn.*, 117, 102.
9. Takeshi Tsuchiya, Tetsuhiro Katsumata, Tomonori Ohba, Yoshiyuki Inaguma, *J. of the Ceramic Society of Japan*, 2009, 117, 102-105.
10. Al. Okos, C. Colin, C. Darie, O. Raita, P. Bordet, A. Pop, 2014, *J. Alloys and Compounds*, 602, 265-268.
11. Al. Okos, A. Pop, Céline Darie, P. Bordet, 2013, *Studia UBB Physica*.
12. O.R. Nascimento, C.J. Magon, L.V.S. Lopes, José Pedro Donoso, E. Benavente, J. Páez, Vladimir Lavayen, María Angélica Santa Ana, G. González, 2006, *Molecular Crystals and Liquid Crystals*, Volume 447, Issue 1.
13. O. Cozar, I. Ardelean, I. Bratu, S. Simon, C. Craciun, L. David. C. Cefan, 2001, *Journal of Molecular Structure*, 563-564.
14. A. Agarwall, A. Sheoran, S. Sanghi, V. Bhatnagar, S.K. Gupta, M. Arora, 2010, *Spectrochimica Acta, Part A*, 75.
15. R.P. Sreekanth Chakradhar, A. Murali, J. Lakshmana Rao, 2000, *Physica B*, 293.
16. N. Vedeanu, O. Cozar, I. Ardelean, V. Ioncu, 2007, *J. Opt. Adv. Mat.*, Vol 9, 844-847.
17. Grommen R., Manikandan P., Geometry and Framework Interactions of Zeolite-Encapsulated Copper(II)-Histidine Complexes, 2000, *J. Am. Chem. Soc.*, 122, 11488-11496.
18. Lin D.H., Coudurier G., Vedrine J., Zeolites: Facts, Figures and Future, Proc 8<sup>th</sup> Int. Zeolite Conf., Amsterdam, The Netherlands, July 10–14 1989, Elsevier, Amsterdam, *Stud. Surf. Sci. Catal.*, 49, 1431, 1989.
19. Bert M. Weckhuysen, Ralf Heidler, 2004, Electron Spin Resonance Spectroscopy, *Mol. Sieves*, 4, 295–335.
20. John A. Weil, James R. Bolton, and John E. Wertz, 1994, Electron Spin Resonance: Elementary Theory and Practical Applications - John Wiley & Sons, New York.



## VERSATILE MEASURING DEVICE FOR THE STUDY OF MAGNETIC PROPERTIES OF SOLIDS

IOAN COSMA<sup>1</sup>

**ABSTRACT.** As a zero apparatus, our measurement device is based on the Faraday method. We have made two compensation systems; mechanical and electromagnetic. It is adapted to the translational movements for insertion of the sample between the poles of the electromagnet that creates a field with an appropriate gradient of operation. To the balance can attach either a non-inductive furnace that provides sample heating up to 1900 K, or a cryostat that provides a controlled cooling temperature and a return temperature between ambient and to liquid nitrogen temperature. Susceptibility and magnetization are assessed in a relative mode; calibration using standard samples of high trust. Magnetic properties studies, versus temperature and intensity the magnetic field, on hundreds materials of thousand different metallic, vitreous and crystalline and oxidic superconductor samples, have been confirmed with similar research, demonstrating the versatility and utility of our measuring system for many years.

**Keywords:** *Susceptibility, magnetization, Faraday balance, magnetic field*

---

<sup>1</sup> *Department of Physics, Technical University of Cluj-Napoca, Romania.*

## 1. INTRODUCTION

Experimental methods for studying the static magnetic properties of materials are based either on the Faraday interaction of a non-homogeneous magnetic field on the sample or on the induction of an electrical current in a circuit by changing the magnetic flux to remove the sample from a homogeneous field [1.2].

The analytical method and device, which ensures high sensitivity, is based on the action of a non-homogeneous magnetic field on the material samples. When the  $dH / dz$  gradient is known, it is easy to assess the magnetic moment of a sample of observed force. Resistance is usually measured by offsetting an analytical balance. That's why this type of equipment is called Faraday Balance. The Faraday magnetic interaction is evaluated from the difference between the apparent and real weight of the sample recorded with the on-off and off-on electromagnet.

More known analytical method and device that provide a high sensitivity is based on the action of a vertical non-homogeneous magnetic field upon material samples. As soon as the gradient  $dH/dz$  is known, it is easy to evaluate the magnetic moment of a sample from the observed force. The force is usually measured with an analytical balance. That's why this kind of equipment is called Faraday Balance. The magnetic part of the vertical force is evaluated from the difference in apparent sample mass with, respectively, the magnet switched on and off.

Development and use of these scales of type Foerrer-Weiss by adapting to the arm of an analytical balance scales fixed on an electromagnet has sample port vertical rods whereby the sample is placed in non-uniform field. The measurements weighing operation and the electro-mechanical design of the balance give rise to various effects which influence the data obtained. Among this influence are the repeatability, nonlinearity, sensitivity tolerance and the temperature coefficient of the sensitivity. Eccentric load can be another effect.

The magnetic balances with horizontal gradient field [3, 4, 5] have many advantages on sensitivity, adaptability and control based on measurements of magnetic field and temperature parameters test sample, thereby eliminating the short comings but also introducing other vertical ones.

To the both types of balance the interaction of scratchy field is applied to the sample in the direction of the magnetic field gradient. This has the value:

$$F_x = m\chi H \frac{dH}{dx} = m\sigma \frac{dH}{dx} \quad (1)$$

where  $\sigma$ ,  $\chi$  and  $m$  are magnetization, susceptibility and mass of the sample;  $dH/dx$  is the gradient of magnetic field.

Magnetic properties study involves to obtaining more accurate values of the studied susceptibilities according to the required temperature and magnetic field for correlating and describing the sample-specific behaviour through different theoretical models. These studies constitute one of the fundamental problems of knowledge at the macroscopic and microscopic physical properties of materials.

## 2. INSTALLATION AND EXPERIMENTAL TECHNIQUE

The device operated by us has a number of facilities and features for study materials paramagnetic, fero, diamagnetic, Shun, antiferromagnetic in a broad spectrum of susceptibility and conditions which provide ground sample up to temperatures of 1900K and controlled cooling of the sample until the liquid nitrogen temperature.

In order to prevent chemical reactions in the sample space at high temperatures, this space is filled with inert gas. The disadvantage of the use of an inert atmosphere is that the whole system has to be placed in a vacuum vessel, in open connection with the sample space in the furnace.

In Figure 1 it can see the constructive and operation scheme of device and of the measuring systems. Swinging system with one degree of freedom  $D_1D_2$  made of thin glass tube suspended by flexible and inextensible silk thread of  $AD_1A'$  and  $BD_2B'$  [6]. To left end of horizontal rod



is attached a quartz port sample cup – *E*. At right end longitudinal with the rod is glued a bar magnet *M* having mass below one gram, with a length of more than 8 times as large as in diameter.

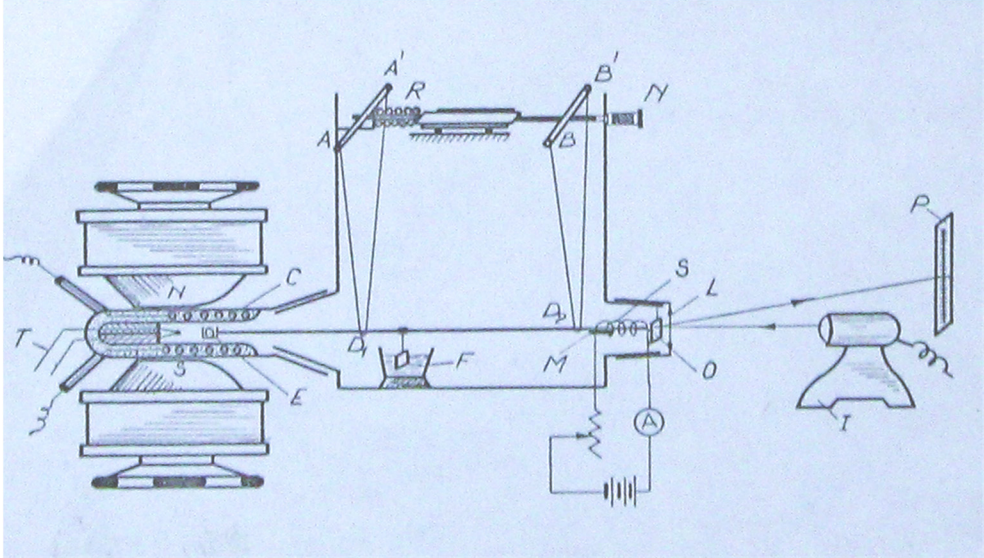


**Figure 1.** Principle sketch of the constructive with measuring systems of magnetic balance for study of static magnetic properties of materials.

The sample is subjected to the force  $F_x$  along the glass rod, carried on by non-homogenous field generated between of *N* - *S* poles of an Weiss type electromagnet. To enable axial centring in furnace and cryostat *C*, the suspension points of oscillation system are adjustable vertically. They can be moved by their horizontal support on a distance measurable using a micrometer *N* and a resort *R*. On the opposite rod of sample-cup is suspended a mirror, which reflect a beam of light passing through the lens it twice focusing a reticular image on the *P*.

The oscillation system behaves normally like a nearly critically damped oscillator. The damping is a viscous damping *F* in transformer oil.

After a suitable d. c. is coupling through the excitation electromagnet coils, force  $F_x$  of the magnetic field over sample is compensated by means of micrometer by moving the suspension system swinging up the spot returns

to zero. Thus the suspension treats form an angle  $\theta$  with the vertical. I mean we have:

$$m\chi H \frac{dH}{dx} = (m_p + m)g \tan \theta \quad (2)$$

Because the mass of the system swinging,  $m_p$ , on the order of a few grams is much greater than the sample mass  $m$  smaller of the meters submitted to measurement the latter can be neglected. After clearing the travel  $d$  measured with the micrometer being very small comparatively with the physical pendulum length  $l$ . Vertical angular tilting of the silk yarn will be also very small; i.e.:  $\theta \cong \tan \theta = l/d$ . With good above the clearing balance of forces is writing:

$$m\chi H \frac{dH}{dx} = mg \tan \theta = mg \frac{l}{d} \quad (3)$$

Working with the same current through the electromagnet excitation for a standard sample with known susceptibility  $\chi_0$  corresponding sizes will be  $m_0$  and  $d_0$  and relationship to relative measurements will be:

$$\chi = \frac{m_0}{m} \frac{d}{d_0} \chi_0 \quad (4)$$

Although the using of mechanical method is relatively simple and has a very high sensitivity, this does not ensure sufficient stability balance. Sample rising in the camp, it has other drawbacks. Such compensation forces range is too small and the precision decreases as a result of instability of zero point, the rising there retains its place in the field.

Shortfalls mentioned and versatility growth a lot and balance was done by adapting an electromagnetic compensation system [5] different from the one used by Sucksmith [6].

Our compensation system consists of a fixed coil and a horizontally mobile bar-magnet glued axially in front of coil. Compensation current  $I$  through the coil, is adjustable and measurable, being supplied by a galvanic or stabilized source. The fixed coil is centreline along the rod in front of which a barium ferrite magnet  $N - S$  moves (Figure 2).

Theoretically, we can consider [6] as a magnet-coil is assessed through an axial force of interaction between the magnetic field and the elementary element of the current  $ds$  spire:

$$df_c = H_c I ds \sin \alpha.$$

For an entire field this force/spire becomes

$$f_c = \int_0^{2\pi r} H_c I ds \sin \alpha = 2\pi r H_c I \sin \alpha \quad [5]$$

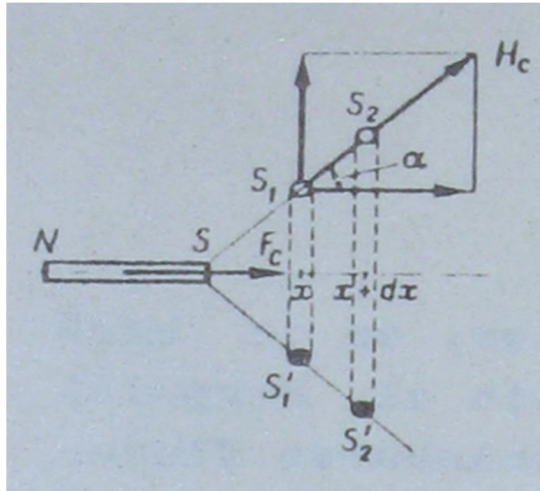


**Figure 2.** Axial force of interaction between a cylindrical magnet and the current through a coil

where  $H$ ,  $N$  and  $\alpha$  are constants for a date. Why magnetic field flow crosses two different layers in turn at a distance  $dx$  infinitesimal considered one another is:

$$\pi r^2 H = \pi (r + dx \tan \alpha) (H + \frac{\partial H}{\partial x} dx).$$

Neglecting the terms which contain small-order infinity, for small angles and the coil has a comparable section of cylindrical magnet we have:

$$\tan \alpha \cong \sin \alpha = \frac{r}{2H} \frac{\partial H}{\partial x}.$$

Value inserted in the expression [1] give the formula of interaction between spire from layer  $j$  and the field magnet bar:

$$f_{ij} = \pi r_{ij}^2 I \frac{\partial H}{\partial x_i}$$

Claims for coil spirals all obtain expression of the force

$$F = \sum_{i,j} \pi r_{ij}^2 I \frac{\partial H}{\partial x_i}$$

for a position because all date coefficients of  $I$  is constant we can write:

$$F = I \sum_{i,j} \pi r_{ij}^2 \frac{\partial H}{\partial x_i} = const I \quad [6]$$

i.e. the force of interaction between the voice coil and magnet bar with the cylindrical section is proportional to the current through the coil.

For the same current through the electromagnet excitation coils in case of standard samples with known susceptibility  $\chi_0$  and a test of the unknown susceptibility  $\chi$  mass  $m_0$  respectively  $m$ , obtaining compensation currents  $I_0$  and  $I$  the relationship for relative measurements will be:

$$\chi = \frac{m_0}{m} \frac{I}{I_0} \chi_0 \quad (7)$$

Practically, based on formula (7), the susceptibility of the materials under study and thus of the magnetic behaviour depending on the temperature, the magnetizing field, the structure, the composition can be analyzed. For this is necessary to weight the etalon and the bulk samples and to determining their intensity of the compensating currents. We use salt Mohr etalon sample with susceptibility at room temperature  $\chi_0 = 32 \cdot 10^{-6}$  emu/g.

### 3. MEASUREMENT METHODS AND USES

The utility of the two mechanical and electromagnetic compensation systems described in the above paragraph, and their adaptation to calibration procedures and appropriate measurement methods at very diverse thermal and magnetic conditions, highlights the versatility, reproducibility and credibility of data obtained with high- precision.

By feeding the electromagnet coils N-S from a DC source, we can obtain magnetic fields of up to 1 Tesla at a distance of 20 mm between the poles during each measurement, which takes about 10-20 seconds. The compensation coil circuit is powered from an adjustable source with currents measured by analogue or digital multimeters. The two DC, excitation and compensation circuits close or open simultaneously with a manual switch

The quartz sample holder cup can move longitudinally into space of furnace / cryostat, type test-tube, outer diameter 12 mm, inner 8 mm. The temperature is measured with thermocouples. A type Pt / Pt(10%Rh) thermocouple is installed inside the furnace space close to the sample. It is directly connected to the input of the micro voltmeter via dedicated extension wire. This thermocouple is isolated with thin alumina tubes

The heating power of 120W of this furnace set-up showed to meet our objectives well and, moreover, to be very fast. With currents up to 3 A at 20 V a temperature of 900 °C is attained within 10 minutes. After switching off the power the temperature is below 50 °C within, again, 10 minutes. The maximum temperature amounts to above 1600 °C (close to 1900 K). From time to time we do checks of the temperature readings with the Curie points of nickel and iron. In all cases, we found results that differed not more than  $\pm 1^\circ\text{C}$ . Literature values scatter between 354 and 358 °C.

Attaching the balance through a two-wire standard ground mouth of small noninductive furnace wound with wire kantal ensure heating samples at temperatures that can achieve the values of 1900K. The same kind it can be attached to a standard ground mouth circulation cryostat, in which sample will be cooled up to temperatures of approximately 93K of evaporation of liquid nitrogen. Knowing the temperature of the sample is assessed through a thermocouple T, Pt – PtRh, in small furnace, respectively Cu - Constantan -in nitrogen cryostat. Thanks of higher facility and accuracy for measurement of electromagnetic compensation scheme, the mechanic system was dropped from. The sensitivity of a balance sheet is based on the value of  $HdH/dx$  product which can be adjusted by changing the distance between both poles of electromagnet but also through the variation of current

excitation and the belt alignment distance between poles. Sensitivity maximum insured through the optical system of compensation is  $\Delta\chi \cong 5 \cdot 10^{-9}$  e.m.u/g. This is sufficient for sample under 100 mg to put in evidence diamagnetic, paramagnetic and one-dimensional antiferromagnetic substances. The interfere field from which assured a given constant force is 2/2 mm and 9 mm in a horizontal plane. This surveying was achieved by casing the magnetic poles cap so that the magnetic field decrease in parabolic axis Ox. These characteristic of non-uniform magnetic field implies relationships:

$$F_x = m\chi H \frac{dH}{dx} \leftrightarrow F_x = \frac{1}{2} m\chi H \frac{d}{dx} (H^2) = m\chi H \frac{dH}{dx} = m\sigma \frac{dH}{dx}$$

In the case of 2 sufficiently small ferromagnetic (~10mg) samples operating under the same conditions of the magnetizing field, the unknown magnetic saturation  $\sigma$  will be evaluated by the relation:

$$\sigma = \frac{F}{F_0} \frac{m_0}{m} \sigma_0 = \frac{I}{I_0} \frac{m_0}{m} \sigma_0 \quad (8)$$

By this relationship, using reliable standard samples, magnetic saturation of ferromagnetic and ferrimagnetic samples can be obtained.

The calibration of the balance was carried out in two steps. In the first step,  $m_0$  and  $I_0$  were measured for a nickel sample which at 20 °C have the saturation  $\sigma_0=54,4\text{emu/g}$ , and in the second step the accuracy of the measured values was checked by studying the thermal saturation of an iron sample in a magnetic field of 14000 Oe. In figure 3, the results of our measurements are given by points and by the continuous curve dependence  $\sigma$  (T) for iron after Bozorth [6].

Paramagnetic susceptibility calibration was done on nickel at temperatures above the Curie point until temperatures above 1400K relative measuring with samples of about 100 mg of Mohr salt having standard susceptibility  $\chi_0=32 \cdot 10^{-6}\text{emu/g}$ . In the same figure 3 is presented  $1/\chi$  (T) dependency graph of the magnetic harnessed (inverse of the susceptibility).

For diamagnetic samples, which are rejected by magnetic field, the susceptibility measurements compensation current requiring being repellents proportional with magnetic field. In the case of our device of quartz port

sample cup implicate a correction to each sample measuring. Otherwise the systematic errors in the susceptibility of the sample studied, which generally represents the percentage values more or less significant.

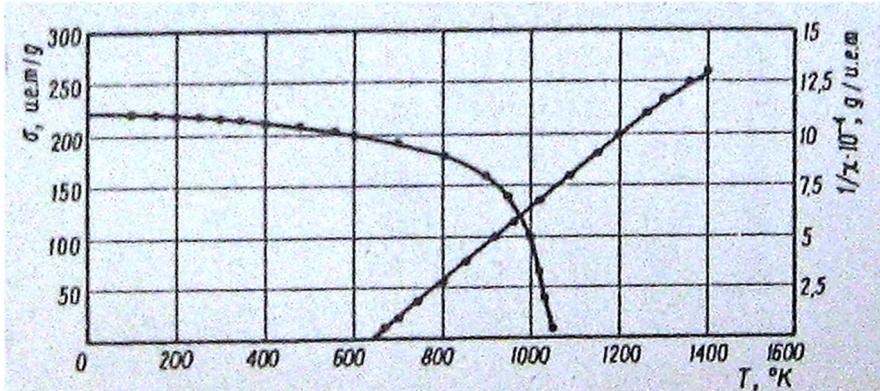


**Figure 3.** The balance calibration in temperature for Fe magnetization and for Ni susceptibility

The degree of confidence in measurement accuracy check if our method through repeatability compensate current through some optical feedback to spot over the landmark ruler graduated in 0 mm. Predictability of appreciation under a 1mA/mm lead we provide values that do not exceed 2%. Calculating these errors in the case of measurements of the masses and current or with the compensator class and scales can be done with the relationship:

$$\frac{\Delta\chi}{\chi} = \frac{\Delta\sigma}{\sigma} = \Delta m \left( \frac{1}{m} + \frac{1}{m_0} \right) + \Delta I \left( \frac{1}{I} + \frac{1}{m_0} \right) \quad (9)$$

In our case, errors are less than 1%. Of course, the stability of the magnetic field and the measurement of the sample temperature are particularly important to ensure the credibility of the determined values.

The type of magnetic balance also allows the magnetic field to be measured instead of the sample. This is particularly important because the use of the Hall (GaussMeter) probe is hard to locate where the sample is

positioned. Thus, will determine for a paramagnetic sample and the susceptibility  $\chi$  and mass  $m_p$  and for a ferromagnetic sample magnetic saturation  $\sigma$  and mass  $m_f$  with and compensation currents  $I_p$  respectively  $I_f$ , the intensity of the magnetic field will be:

$$H = \frac{I_p m_f \sigma}{I_f m_p \chi} \quad (10)$$

The results in determining field after relation (10) are in agreement with those obtained by soak up gaussmeter with the probe.

Magnetization measurements depending on the temperature range 90-1300K are facilitated by the fact that we can attach through the same standard ground mouth a small cryostat respectively furnace for study magnetic behaviour with temperature. By maintaining the temperature at a constant value can we assign magnetization isotherms according to camp through excitation current intensity variation through the electromagnet. Determination of temperature of transition (points) Curie can be done also described within the installation. For this the temperature at which the sample of the material by heating ferromagnetic becomes paramagnetic. For the exact determination of the sample are measured in arbitrary unit's magnetization to the excitation currents as small. The values obtained are draw graph thermal variation of Curie temperature magnetization is considered the place where the tangent point of inflection of the curve cut temperature axis. The data found for Ni 631K and Fe 1043K represent reliable values for thermal studies of magnetic properties of concordant with those presented by Bates [9]. So I could continue and expand studies [10] on the Curie points of alloys of nickel with non-magnetic elements initiate by my teacher Victor Marian.

#### 4. CONCLUSIONS

The study of magnetic properties is one of the fundamental problems of the knowledge, at the macroscopic and microscopic level, of the physical properties of the materials. Their research involves knowing as



accurately as possible the values of susceptibility of the studied sample, depending on temperature and field, necessary to correlate and describe the specific behaviour of the sample through different theoretical models. Besides the theoretical impetus, the magnetic behaviour of new and new materials is of great applicative importance in new technologies.

Our installation, which has been verified by hundreds and hundreds of studies on the magnetic behaviour of thousands of conductive, semiconductor, insulating and superconducting, metallic, oxide, crystal and glass samples, has proven its usefulness and credibility. Its versatility in the determination of static magnetic parameters as well as their dependence on variable external factors, allow decisive correlations with the dynamic studies of magnetic structures at microscopic and atomic level.

## ACKNOWLEDGMENTS

My esteem and gratitude goes to Professor Iuliu Pop for his assistance in data acquisition during the first part of this experiment. Sincere thanks to Professor Emil Burzo, for the many valuable conversations and useful collaborations.

## BIBLIOGRAPHY

1. Weiss P., Foerer R., *Ann. de Physique*, 5, 153 (1926).
2. Foex G., Forrer R., *J. Phys. Rad.*, 7, 180(1936).
3. Maxim I., Pop I., Nicula A., *Studia UBB*, ser I/1, 260(1960)
4. Pop I., Cecernicov V. I., *Pribori i tehnica experimenta*, 5, 180 (1964)
5. Cosma I., *Comunicari Bul. Inst. Politehnic Cluj*, p. 432 (1971).
6. Pop V., Cosma I., Ardeleanu I., *Comunicare Anal*, Univ Oradea.
7. Sucksmith W., Clarck C. A., Oliver C. J., Thompson J. R., *Rev. Mod. Phys.* 25, 1, 34(1953).
8. Bozorth R. M. I. I. L. *Moskva* (1956).
9. Bates L. F., *Modern Magnetism*, Cambridge University Press (1965).
10. Marian V., *Ann. de Physique*, 11, 7, 459.